Novel Experimental and Analysis Paradigms for Neuroimaging

by

Wenjing Yan

A dissertation submitted to the Graduate Faculty of
Auburn University
in partial fulfillment of the
requirements for the Degree of
Doctor of Philosophy

Auburn, Alabama
August 5, 2017

Keywords: HRF, fMRI, Autism, Bipolar Disorder, Schizophrenia, Functional Connectivity

Approved by

Gopikrishna Deshpande, Chair, Associate Professor of Electrical and Computer Engineering
Thomas Denney, Professor of Electrical & Computer Engineering
Jeffrey Katz, Alumni Professor of Psychology
Jennifer Robinson, Assistant Professor of Psychology

Abstract

Functional magnetic resonance imaging (fMRI) technique uses the blood-oxygen-level-dependent (BOLD) contrast to detect associated changes in blood flow. The BOLD signal is temporal correlated with cerebral electrophysiological activities. Therefore, the recording and decoding of the BOLD signal provides insight into human brain function and benefits enormous amount of brain cognitive studies in scientific and medical interest. Although fMRI has become the primary application in the field of brain cognitive science, elusive and enigmatic questions remain. The scope of this dissertation lies in the construction of novel signal processing methods and experimental paradigms with fMRI applications, which devotes to the strategies of decoding brain signals and states.

In the first and second studies, we addressed the issue that the fMRI is an indirect measure of neural activity. Since the BOLD signal can be modeled as a convolution of the hemodynamic response function (HRF) and latent neural activity and HRF varies across both between individuals and different brain regions within an individual. Therefore, the correlation acquired from the BOLD-level data could lead to false inferences of functional connectivity. The aberrant neurochemical mechanism which control the shape of the HRF have been reported in autism spectrum disorders (ASD), schizophrenia (SZ) and bipolar disorder (BP). Therefore, we hypothesized that these aberrations would lead to differences in the shape of the HRF between these pathological populations and healthy controls, and the alterations would contribute to the differences in estimating functional connectivity in the BOLD space as compared to the latent

neural space. We reported that raw fMRI data failed to detect group differences in connectivity analysis when compared that with deconvolved data. Our results are relevant for the understanding of hemodynamic and neurochemical aberrations in pathological groups.

In the third study, we applied a novel real-time fMRI (rt-fMRI) neurofeedback technology to investigate the insight problem solving. Inspired by a transcranial direct current stimulation (tDCS) study, we hypothesized that rt-fMRI neurofeedback could enable subjects to up-regulate activity in their right Anterior Temporal Lobe (rATL) using neurofeedback, and it could mimic the effects of tDCS in facilitating subjects to solve the nine-dot puzzle. Our results show that approximately 40% of subjects were able to solve the problem using rt-fMRI neurofeedback, which is similar to the percentage of subjects who were able to solve the puzzle using tDCS. Our results indicated that the group that successfully solved the problem were able to up-regulate the activity over rATL through rt-fMRI neurofeedback while the group that didn't solve the problem were not able to. Further, we contrasted the brain activation and network obtained from two groups to investigate the neural bias generated by up-regulation of activity in rATL. Our results provideda putative neural mechanisms underlying nine-dot problem solving, and a possible explanation for the top-down inputs into the rATL in enhancing or suppressing creative insight. Furthermore, our study demonstrates that neurofeedback could potentially be used to mimic effects similar to brain stimulation techniques such as tDCS.

Acknowledgements

First and foremost, I wish to express my sincere gratitude to my supervisor, Dr. Gopikrishna Deshpande, for the continuous support throughout my Ph.D. study and related research. His guidance has been of invaluable help in the research and writing of this thesis.

Apart from my advisor, I would like to thank the rest of my thesis committee members: Dr. Thomas Denney, Dr. Jefferey Katz, Dr. Jennifer Robinson, and my university reader Dr. Sridhar Krishnamurti, for their insightful comments and encouragement.

My sincere gratitude also goes to my fellow labmates, Sinan Zhao, Yun Wang, Xinyu Zhao, and Ranga Deshpande for the stimulating discussions, for the encouragement, and for the time they spent working with me. I would also like to thank my friends Chong Li, Xinning Wang, Zerui Dong, Qiong Hu and Fang Yu.

I would also like to express my special gratitude to Prof. G. Székely and the other lab staff members from the Computer Vision Laboratory of the ETH Zürich. He shared the digital model of the 3D anatomy of the thalamus according to the atlas of Morel by a written consent.

Last but not the least, I would like to thank my family. My father, Shilong Yan, who was an accomplished professor in the field of chemical engineering. He is my role model and he inspired me to choose my academic life path and taught me how to become a person of integrity. He passed away in the fourth year of my Ph. D study, but his spirit has given me the power to bear all the sorrows and finish my Ph.D. study. My mother, Xuehua He, a journal editor, who is a tender, smart, and strong-willed woman. She always supports me in any situation, encourages me when I fall,

and guides me with her wisdom. Under any circumstance, I can always get love and courage from them. My husband, Haipeng Li, who is a Ph. D in computer network systems engineering. We have supported each other during our doctoral study.

Pursuing a doctoral degree is a difficult and challenging task. Because of the loss of my father, the last year of my Ph. D life has been tough for me. Without the support of my family and friends, I would not have been able to get over all the sad days and finish my Ph. D studies. Throughout this long journey, I have gained not only academic progress but also experience of life. I will always appreciate everything that I own and keep holding onto faith in my life.

Finally, I dedicate this dissertation is dedicated to the memory of my beloved father --Shilong Yan (1958-2016). He was an accomplished professor in the field of chemical engineering, who committed his whole life to research and made remarkable achievements. He was a respectable professor who provided inspiration, motivation and inherent guidance to all his students. He was an honorable man who lived with dignity. At his funeral, thousands of people gathered and grieved over his death. His life deserves to be honored.

Table of Contents

List of Tables

List of Figures

List of Abbreviations

MRI	Magnetic Resonance Imaging
fMRI	Functional Magnetic Resonance Imaging
BOLD	Blood-Oxygen-Level Dependent
EEG	Electroencephalograph
CBF	Cerebral Blood Flow
CBV	Venous Blood Volume
CMRO2	Oxygen Metabolism
nNOS	Nitric Oxide Synthase
NO	Nitric Oxide
NMDAR	N-methyl-D-aspartate Receptors
mGluR	Metabotropic Glutamate Receptors
GABA	The γ--aminobutyric Acid
HRF	Hemodynamic Response Function
RH	Response Height
TTP	Time to Peak
FWHM	Full Width at Half Maximum
rs-fMRI	Resting-State Functional Magnetic Resonance Imaging
rt-fMRI	Real-Time Feedback of Functional Magnetic Resonance Imaging
rATL	Right Anterior Temporal Lobe

tDCS	Transcranial Direct Current Stimulation
ASD	Autism Spectrum Disorder
BP	Bipolar Disorder
SZ	Schizophrenic
TR	Repetition Time
GLM	General Linear Model
FWER	Family-wise Error Rate
FDP	False Discovery Proportion
FDR	False Discovery Rate
CKF	Cubature Kalman filter
ABIDE	Autism Brain Imaging Data Exchange
MPRAGE	Magnetization-Prepared Rapid Acquisition with Gradient Echo
IRBs	Local Institutional Review Boards
HIPAA	Health Insurance Portability and Accountability
DPARSF	Data Processing Assistant for Resting-State fMRI
SPM8	Statistical Parametric Mapping
MNI	Montreal Neurological Institute
AAL	Automated Anatomical Labeling
DC	Deconvolved
NDC	Non-deconvolved
BA	Brodmann Area

CSF	Cerebro-Spinal Fluid
GC	Granger Causality
ROI	Region of Interests
DSM-5	Diagnostic and Statistical Manual of Mental Disorders Fifth Edition
GE-EPI	Gradient-Echo Echo-Planar Images
MD	Mediodorsal
Hb	Habenular
CL	Central Lateral
lATL	Left Anterior Temporal Lobe
GC	Granger Causality
DGC	Dynamic Granger Causality
lAG	Left Angular Gyrus
rIFG	Right Inferior Frontal Gyrus
rSFG	Right Superior Frontal Gyrus
lSFG	Left Superior Frontal Gyrus
CauH	Caudate Head
rSOG	Right Superior Occipital Gyrus
rSPG	Right Superior Parietal Gyrus

Chapter 1

Introduction

1.1 Background Review

1.1.1 BOLD Signal

The blood-oxygen-level dependent (BOLD) contrast imaging is based on the principle that the oxyhemoglobin shows less magnetic susceptibility than deoxyhemoglobin. More specifically, since the brain can't reserve energy in the form of sugar and oxygen, the neuronal firing calls for a rapid energy supplying favored by cerebral blood flow. When a certain brain region functions, the regional blood releases a greater rate of oxygen to active neurons than to inactive neurons. And then, the unbalanced magnetic changes of oxyhemoglobin and deoxyhemoglobin would be captured by the MRI scanner. In 1990, Seiji Ogawa et al [1] first demonstrated that the variations of blood oxygenation in vivo could be detected with the MRI and provided the concept of BOLD. Figure 1.1 represents the example of BOLD signal.

The BOLD signal is sensitive to cerebral blood flow (CBF), venous blood volume (CBV) or oxygen metabolism (CMRO2), where the CBF change is most consistent with fluctuation of BOLD signal and it can be used to estimate changes in CMRO2 [2]. Therefore, CBF is a valuable tool in exploring the physiological processes underlying neural stimulus-induced BOLD activation.

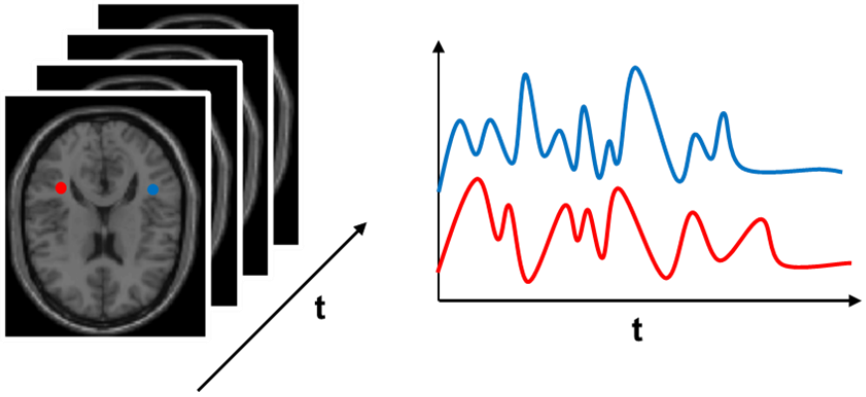

Figure 1.1 *Example of BOLD signal.*

Although changes in CBF correlate with energy supplying during brain functional activation [3], it's not simply regulated by the oxygen or energy usage but a set of complex biochemical and electrophysiological processes. Evidence has confirmed that several neurotransmitter-related signaling mediations in neurovascular coupling mechanism regulate the CBF and imply the generation of BOLD single [4] (Figure 1.2).

Glutamate which is released by synapse in response to neural activity primarily regulates the CBF. In neurons, glutamate acts on N-methyl-D-aspartate receptors (NMDAR), causing neuronal nitric oxide synthase (nNOS) to release nitric oxide (NO). This released NO dilates vessels directly and indirectly in different brain regions [6][7]. Also, glutamate activates astrocyte by acting on metabotropic glutamate receptors (mGluR) and then, astrocyte converted glutamate to glutamine to supply the usage of energy [5]. During this procedure, astrocyte releases serval neurotransmitters (e.g. Ca(2+), K(+), 20-hydroxyeicosatetraenoic acid and etc.) which are important in mediating CBF [6].

The γ--aminobutyric acid (GABA) also has effects on regulating the CBF. Interneurons release GABA in response to stimulation of the basal forebrain, which inhibits neural activity through the GABA receptors [7]. Then, the altered neural activity could lead to altered mediation to blood vessels. It is still unclear that the mediation is direct or via agents: neurons or astrocytes.

The serotonin (5-hydroxytryptamine) is demonstrated as major vasoconstrictor, providing blood-brain barrier permeability. It modulates neurovascular coupling mechanism either directly or indirectly via the neuronal-astrocytic-vascular tripartite functional unit [8].

In addition, therapeutic modulation and metabolic aberrance may as well affect the signaling pathways and alter the neurovascular coupling mechanism [9].

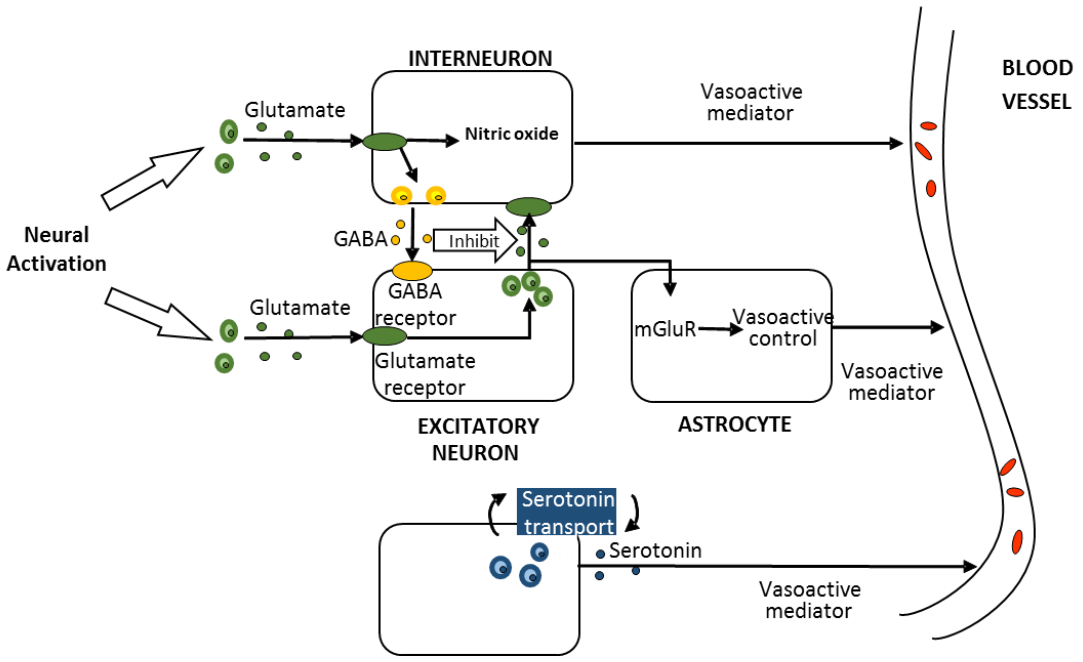

Figure 1.2 *Signaling pathways of neurovascular coupling mechanism. The interneurons, neurons, and astrocytes release vasoactive mediators, leading to both dilation and constriction of the vessels nearby.*

1.1.2 Functional Magnetic Resonance Imaging based on BOLD Technology

Since Charles Roy and Charles Sherrington demonstrated that blood flow and blood oxygenation are closely linked brain function in 1980 [10], Kenneth Kwong et al [11] first applied the BOLD technique to study activation in the visual cortex in human subjects and termed it as functional magnetic resonance imaging (fMRI) in 1992. Through manipulation of stimulus, the rise of BOLD signal was found that lags the neuronal events for few seconds. If the stimulus continuous, which means neurons keep firing, the peak spreads to a flat plateau. After stimulus stops, the BOLD signal falls [12]. The relationship between changes in brain activity and BOLD signal is indirect and has been speculated, however, the neural basis of the BOLD signal has been gradually demonstrated by experiments which combined other neuroimaging technologies (e.g. Electroencephalograph (EEG)) and intracortical recordings. Researchers have checked the BOLD signal corresponding to both signals from implanted electrodes (mostly in monkeys) and signals of field potentials (measured outside the skull) from EEG and MEG, and demonstrated that the local field potential, which includes both post-neuron-synaptic activity and internal neuron processing, better predicts the BOLD signal [13]. After that, the fMRI technology based on analysis of BOLD signal has gradually became the leading research tool in investigating human brain function.

The fMRI technology is applied diversely and multitudinously both in the research world and clinical world. Since it is a noninvasive and it has high spatial resolution (works at a resolution of

tens of micrometers) and low temporal resolution (works at hundreds of milliseconds or seconds), the fMRI has the advantage in precise functional specialization. The brain mapping is the best established application of fMRI, which applied the fMRI to determine the precise neuroanatomical locations in responsible for specific brain functions [14]. The functional integration is another well-established application of fMRI, which is describing how different brain areas interact. The high spatial resolution allows the investigation between highly constrained spatial regions in the brain. A wide range of statistical techniques are being used to measure inter-regional connectivity (e.g., Independent Component Analysis), and "causal" connectivity (e.g., Dynamic Granger Causality). To date, these two applications have been applied in investigating the brain functional systems and boosted many achievements, including visual, auditory, sensorimotor, emotional, memory, language, attention or control and etc [15].

Typically, the measured BOLD signal contains many noise signals, such as the artefactual signals due to hardware of the scanner, signal changes due to head motion, multitude of physiological fluctuations of cardiac and respiratory noise, random brain activity, changes in blood pressure and cerebral autoregulation mechanisms and etc [16]. The non-neuronal noise can introduce spurious common variance across time series and considerably affects the results of task-based and resting state fMRI experiments. In task-based fMRI, it is generally thought that task-based fMRI is sufficiently robust to non-neuronal noise because most fMRI studies repeat a stimulus presentation multiple times and average the response to eliminate the effect [12]. However, the noise components might confound the timing of the response and introduce variance

in the signals from different regions of the brain, thus affecting the estimation of functional or effective connectivity. In resting state fMRI (rs-fMRI), the analysis cannot benefit from an averaging process which removes these non-neuronal noise as it is done in task-based fMRI [17]. Different methods have been developed to cope with multiple types of noise components and interaction between noise sources, such as developments in acquisition sequences to diminish the system-related artefacts, motion-related correction, physiological-related noise, and etc. However, cleaning the non-neuronal in BOLD measurement and estimating the true neuronal activity are still challenging tasks in fMRI and it could boost the novel applications research world and clinical world.

1.1.3 Hemodynamic System Modelling

The physiological mechanisms mediating the relationship between neuronal activation and BOLD signal have been studied extensively, and the realistic physiological model is extremely complex and hard to be constructed [9][18]. However, studies demonstrated that although the hemodynamic model is nonlinear in nature [19], it exhibits relatively linear and time-invariant relationship with regard to specific manipulation of experiment [20][21]. The relationship between neuronal activation and BOLD signal can be approximated by mathematical modeling, which assumes the measured BOLD signal as the neuron activities convolved with the hemodynamic response function (HRF) (Figure 1.3). In the paradigm, $s(t)$ represents the time series of the stimuli specified as supposed neuronal activity. The $f(t)$ represents the measured fMRI signal for a particular voxel, which is calculated as $f(t)=s(t)\otimes h(t)+\varepsilon(t)$, where $\varepsilon(t)$ represents the noise. The

system function *h(t)*, termed as HRF, is determined from the response to an impulse function or Dirac delta function.

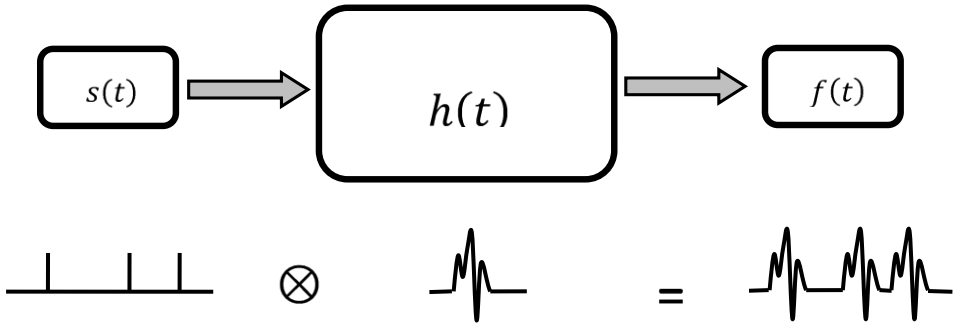

Figure 1.3 *Hemodynamic model.*

In fMRI experiments, this model is sufficient to characterize up to 90% of the BOLD responses in some cortical regions [22]. Based on this model, hidden neural states and parameters of the nonlinear/linear dynamic system can be inferred by inversed convolution, and different algorithms of inversion are developed with regard to distinct experiments.

The canonical HRF [23][2] is modeled by two Gamma functions with six unknown parameters (four of them to model the shape and the remaining to scale and baseline respectively). Most HRFs share the similar shape across different regions and subjects. Normally, the HRF is estimated by three parameters (Figure 1.4): response height (RH), time-to-peak (TTP), and full-width at half-maximum (FWHM), respectively. L. D. Lewis et al used simultaneous EEG–fMRI and compared evoked potential measured by EEG with the shape of HRF acquired by fMRI [24]. They reported that the waveform of HRF depends on the underlying dynamic activity pattern and faster HRFs may provide a better representation of the true hemodynamic response [24][25]. Lindquist and

Wager [26] have proposed a scheme to illustrate the relationship between neural activity, observed BOLD response, and estimated HRF parameters (Figure 1.5). The induced change in RH, TTP and FWHM, could be interpreted regarding the latency of neural firing, onset latency, and duration of neural activity.

The three parameters are unlikely uniquely interpreted regarding the changes in neuronal activity. The potential cross-talk exists among all the estimated parameters. Moreover, the clear interpretability is constrained by incomplete comprehension in physiology mechanism of BOLD.

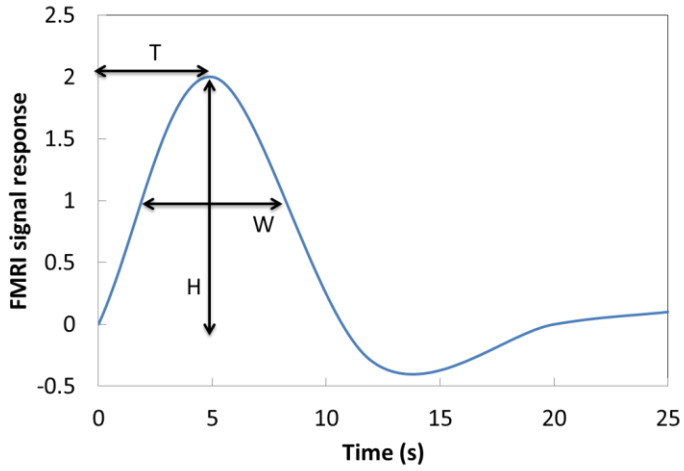

Figure 1.4 *Estimates of response height (RH), time-to-peak (TTP), and full-width at half-max (FMHW) from a simulated HRF.*

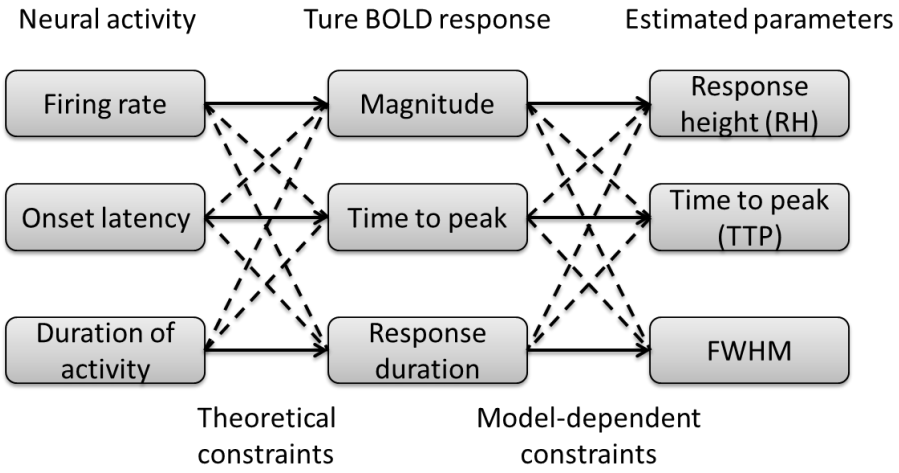

Figure 1.5 *The relationship between neural activities, BOLD observation, and estimated HRF parameters [26]. Solid lines indicate expected relationships; dashed lines indicate potential relationships that could obstruct the interpretation of estimated parameters.*

1.1.4 Resting State Functional Connectivity

The rs-fMRI experimental paradigm measures the BOLD signal when a subject is not performing an explicit task. Even in the absence of cognitive or sensory stimulation, the rs-fMRI BOLD signal displays spontaneous low-frequency fluctuations [27][28] and the significant ongoing spontaneous brain activity has been demonstrated in many literatures [29][30].

The rs-fMRI connectivity is the analysis based on rs-fMRI BOLD signal and it explores the co-activation and co-deactivation between brain regions, even if they are distinct [31]. It is simply a statement in terms of statistical dependencies among neurophysiological measurements (e.g. fMRI signal), which indicates the "temporal correlations between spatially remote neurophysiological events" [31]. Recently, the rs-fMRI functional connectivity analysis has become a useful approach to explore the functional network structure of the human brain [32][33].

1.1.5 Real-time fMRI Neurofeedback

The real-time of fMRI data (rt-fMRI) neurofeedback technology permits simultaneous measurement and observation of brain activity during an ongoing task. It allows participants to selectively regulate their own brain activity by gaining volitional control over the BOLD signal from specific regions of their own brains provided as a feedback [34][35]. The efficacy of rt-fMRI neurofeedback could be demonstrated by the observed enhanced levels of raw BOLD signals or the enhanced neuronal activation within the regions of interest (ROIs) before and after rt-fMRI trials. In previous studies, the self-regulation of brain activity has been achieved in various regions, e.g., the anterior cingulate cortex for pain control [36], the amygdala for the emotional regulation of fear [37], etc. Moreover, the learned control over the local brain activity via rt-fMRI neurofeedback training enables the correspondingly changes in behavior [34][35]. Therefore, the rt-fMRI neurofeedback technology could complement traditional neuroimaging techniques by providing more causal insights into the functional role of brain regions in behavior, which allows it to become a promising new approach for the cognitive neuroscience.

A rt-fMRI neurofeedback system is usually constructed by a fMRI scanner responsible for data acquisition (Figure 1.6 A), a scanner host responsible for data transferring (Figure 1.6 B), a computer responsible for data pre-processing in real-time (Figure 1.6 C), and a device to show the feedback signal to the participants (Figure 1.6 D). The procedure transfers the acquired raw BOLD single to the pre-processed BOLD signal, and presents the feedback signal could be finished within seconds. Therefore, the self-regulation of participants based on the feedback signal could be

ensured to be conducted in nearly real time. The participants are usually trained by following the instructions (e.g. by increasing the signal or decreasing the signal.) according to different experimental aims.

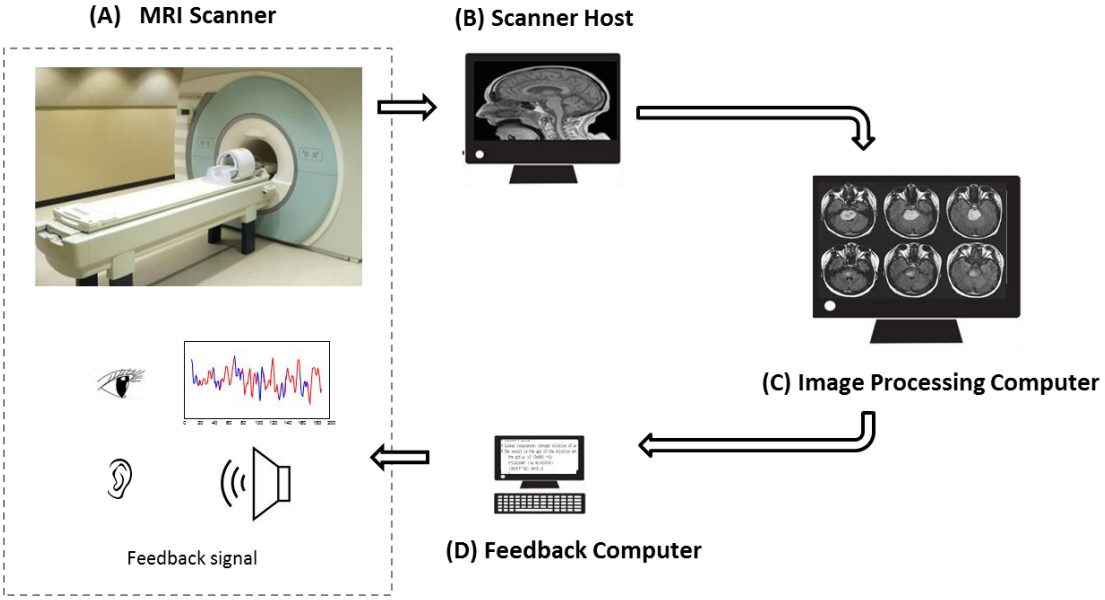

Figure 1.6 *An architecture of rt-fMRI system is consisted of (A)MRI scanner, (B)Scanner host (C) Image processing computer, and (D) Feedback computer.*

1.1.6 Insight Problem

Schooler, Ohlsson, and Brooks [38] defined the insight problem by saying that "an insight problem is well within the competence of the average subject has a high probability of leading to an impasse and has a high probability of 'rewarding' sustained effort with an aha-experience." Unlike non-insight problems, the solutions for insight problems cannot be guaranteed by analytical thinking and prior knowledge, while conceptual restructuring is an important key [39]. More specifically, while solving, one would try to minimize the difference between the current state of the problem solving and the goal state. Insight only occurs when one realizes that the following analysis steps could not achieve the goal and that a new analysis must be sought.

The nine-dot problem is one of the most classic insight problems, which requires both analytical thinking and conceptual restructuring. The problem requires that nine dots be arranged in a square connected by four straight lines drawn without lifting the pen from the paper and without retracing any lines (Figure 1.7). This problem is ridiculously simple in the formal sense that there are only a few possible solutions to try, but ridiculously difficult in the psychological sense that the probability of success approximates 0% [40]. The explanation for this phenomenon is because our brains, especially left hemisphere, are wired to interpret the world though the filter of our past experiences, and we are inclined to see the nine-dots as a square, with imposed rigid boundaries. This mechanism is mostly unconscious and cannot be easily overridden.

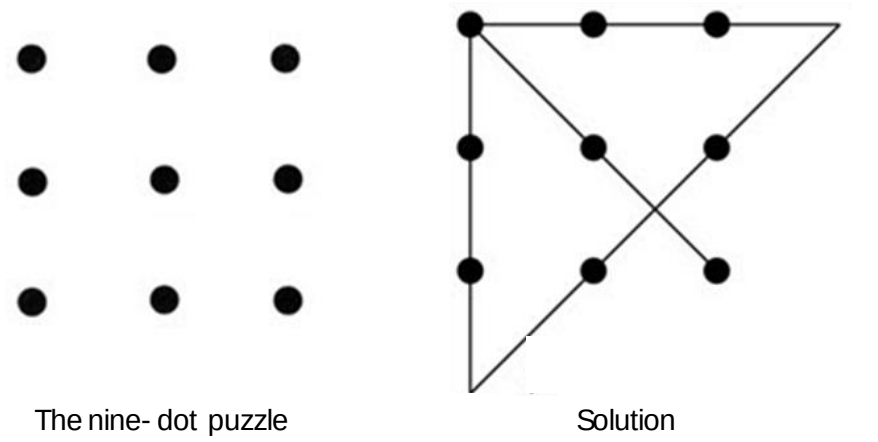

Figure 1.7 *The nine-dot problem and its solution.*

1.2 Motivation

The high-resolution fMRI is a powerful tool for the noninvasive imaging of human brain. Normally, fMRI is used popularly in mapping brain activity related to specific behaviors [41][42]. In recent years, fMRI has been applied to new decoding-based strategies in human cognitive research which requires new data processing methods and experimental paradigms.

Resting-state functional magnetic resonance imaging (rs-fMRI) connectivity is a novel method that estimates the temporal correlation of BOLD signals between spatially remote brain regions in resting state [29][30][31]. The relationship between brain regions is referred as resting-state functional connectivity. This allows the characterization of large-scale brain networks both in healthy and clinical populations. To date, a number of studies have employed rs-fMRI functional connectivity in order to understand both shared and distinct neural alterations in pathological populations with healthy controls [43][44][45]. However, criticisms were also raised. One important issue in interpreting rs-fMRI functional connectivity lies in that the fMRI BOLD contrast is an indirect measure of neural activity [46][13]. The measured BOLD signal could be considered as a convolution of the latent neural activity with a transfer function – the HRF [20] and the shape of HRF varies not only across subjects but also across different brain regions in the same subject [47][48]. Besides the underlying neural activity, different non-neural factors could contribute to this variability [4][49][50][51][52]. The usefulness of HRF deconvolution is under debate. David et. al [53] first performed a combined EEG-fMRI study that proved the theoretical possibility of HRF deconvolution in improving interregional coupling estimation from hidden

neural states of fMRI. Previous discussions on evaluating effective connectivity from fMRI data also reached the conclusion that it is better to use state-space model for inferring causality on hidden neural states [54][55][56]. In the light of these works, we continue the discussions into rs-fMRI connectivity analysis.

As mentioned above, the examined synchronicity between observed BOLD data in any two given regions would be blurred by the varying HRF due to non-neural factors. And the false inferences of functional connectivity could be observed in two situations: (i) the BOLD data are highly correlated while the underlying latent neural signals are not (Figure 1.8 A); (ii) the underlying latent neural signals are highly correlated while the BOLD data are not (Figure 1.8 B).

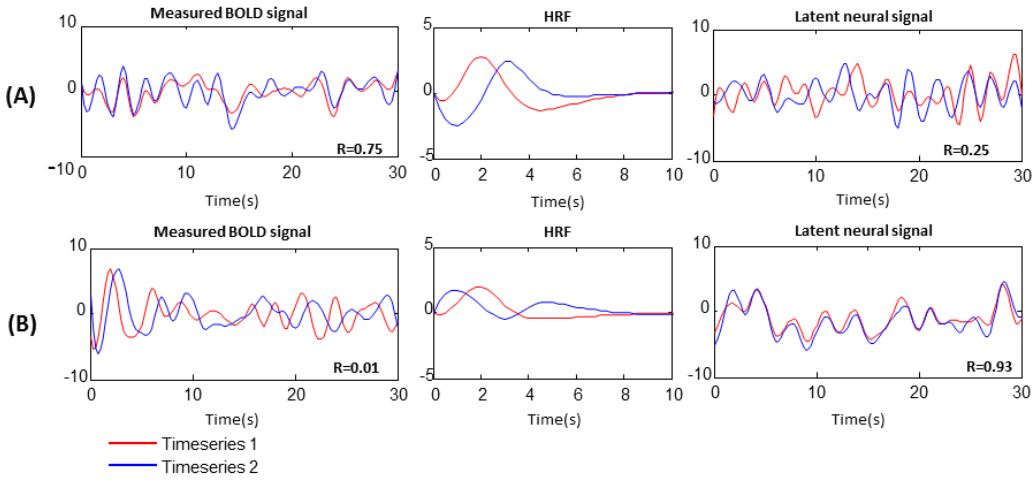

Figure 1.8 *Illustration of the impact of HRF variability on functional connectivity analysis. The measured BOLD signal, retrieved latent neural signal and the voxel-level HRF are shown. (A) Two BOLD time series are low correlated while the correlation between underlying neural signals is high. (B) Two BOLD time series are highly correlated while the correlation between underlying neural signals is low.*

Since, factors other than neural activity could contribute to this variability was confirmed in ASD [57], SZ [58][59][60][61][62] and BP [63][64][65], we hypothesized that this could potentially cause systematic differences in the shape of the HRF between pathological populations

and healthy controls, and the altered HRF will lead to differences in estimated functional connectivity in the fMRI space as compared to the latent neural space. We aimed to demonstrate that the possible confounds introduced by the variable HRF in identified functional networks of pathological populations.

The rt-fMRI neurofeedback technology is another novel neuroimaging technology applied in human cognitive research. It allows on-line analysis and feedback of BOLD signal from a targeted ROI. Compared with other neuroimaging techniques, the rt-fMRI neurofeedback technology provides the only non-invasive method that could acquire the feedback signal of the deep subcortical brain regions. In previous studies, the self-regulation of brain activity has been observed in various regions, e.g., the anterior cingulate cortex for pain control [36], the amygdala for the emotional regulation of fear [37], etc. Studies also demonstrated that the learned control over the local brain activity via rt-fMRI neurofeedback training was able to cause the specific changes in behavior [34][35]. Although much progress has been achieved, the applications of rt-fMRI technology are still being explored. The capability of tracking brain activations could lead to new research modalities and practical applications in both clinical and daily life. Therefore, we propose a novel application of rt-fMRI in brain stimulation. Based on the research that applied the transcranial direct current stimulation (tDCS) targeted on right anterior temporal lobe (rATL), a surprisingly large number of people (40%) were able to solve the nine-dot puzzle [66]. We aimed to mimic this tDCS by applying rt-fMRI technology, which could provide a new paradigm for

cognitive neuroscience to study brain plasticity. We also aimed to estimate the functional relevance of regulated brain areas by modification of insight problem solving.

1.3 Organization of the Dissertation

This dissertation is organized into 6 chapters. Chapter 1 reviews relevant background about BOLD signal, fMRI, rt-fMRI, and the basis of experiment design. It also represents the motivation for this dissertation and elaborates the structure of the dissertation. Chapter 2 describes the general methods that were applied in this dissertation, including BOLD signal preprocessing, deconvolution, rs-fMRI connectivity analysis, effective connectivity analysis, visualization of connectome and relevant statistical methods. Chapter 3 represents the procedures of examining seed-based rs-fMRI functional connectivity studies in ASD and control subjects. It also represents the result of aberrant hemodynamic responses in ASD and its implications for seed-based rs-fMRI functional connectivity studies. Chapter 4 represents the procedures of examining seed-based rs-fMRI functional connectivity studies in SZ, BP, and control subjects. It also represents the result of aberrant hemodynamic responses in these populations and its implications for seed-based rs-fMRI functional connectivity studies. Chapter 5 represents the experiment that mimics the effects of tDCS in facilitating individuals to solve the nine-dot puzzle by applying rt-fMRI neurofeedback technology. The contracted brain activation and networks of the subjects who solved the puzzle and those who did not are also represented. Chapter 6 provides the conclusion to summarize this dissertation.

Chapter 2

General Methods

2.1 Review of Statistical Methods

2.3.1 Statistical Parametric Mapping

Statistical Parametric Mapping (SPM) is a statistical approach to infer the topological features function continuously. Specific to neuroimaging, it is usually used to identify regional brain activations by assuming parametric statistical models at each voxel. Mathematically, it mapps values with probabilistic behavior by a known probability density function, usually the Student's t or F-distributions.

For each voxel, the observed response variable Y is formulated based on a General Linear Model (GLM),

$$Y = X\beta + \varepsilon \tag{2.1}$$

X is a design matrix, which is a linear combination of explanatory variables and ε is a well-behaved error term [67]. β is a matrix of parameters that represents the relative contribution of each of these columns in design matrix X. This formulation allows the assessment of the F-statistic

about these contributions by testing the null hypothesis according to a given contrast, the linear combination of the contrasts, or all of them together.

2.3.2 False Discovery Rate Controlling

When a large number of statistical tests are performed simultaneously, the probability of making at least one false positive (type I error) among the family of hypothesis tests is defined as the family-wise error rate (FWER). The FWER would cause the classic confidence intervals, and p-values fail to reject the null hypothesis. False discovery rate (FDR) controlling is a technique that quantifies the statistical significance of multiple statistical tests [68][69]. Mathematically, it adjusts the false discovery proportion (FDP), which is defined as the proportion of false discoveries among total rejections.

Suppose N (null) hypotheses, $H_1, H_2, \dots, H_N$, are tested simultaneously at a level α. Their corresponding p-values are sorted in an ascending order, $P_1, P_2, \dots, P_N$. Find the largest k that satisfies $P_k \leq \frac{k}{N}\alpha$, then Reject the null hypothesis $H_i, i = 1,2, \dots, k,$ where $H_i = 0$, when the ith null hypothesis is true, and $H_i = 1$ when the ith alternative is true.

Let $p_i \leq t$, for $i = 1,2, \dots, m$ and $t \in [0,1]$. Therefore the FDP is calculated as:

$$FDP(t) = \frac{False\ \ Discoveries}{Discoveries} = \frac{\sum_i \{ture\ \ null\ \ P_i\colon\ P_i \leq t\}}{\sum\{P_i \leq t\}} \tag{2.2}$$

The FDR controlling for a multiple testing threshold α is defined as the expected FDP using that procedure:

$$FDR = E(FDP(t)) \tag{2.3}$$

The FDR controlling has been intrudouced in many applications across different fields and was introduced by Genovese et al into the filed of neuroimaging at 2002 [70].

2.2 Image processing

2.2.1 Pre-processing

Pre-processing is necessary for fMRI analysis, which prepares the acquired raw data before being applied to statistical analysis. It applies various image and signal processing techniques to reduce noise and artifacts (e.g. head motion, field non-uniformity, acquisition synchrony, etc. [12]) in BLOD signal. The pre-processing steps are crucial in making the statistical analysis valid in the subsequent analyses.

The usual method of pre-processing is to apply sequential individual processing steps in a particular order. However, the interactions between these steps may cause the loss of statistical power and the different post fMRI data analyses require distinct sets of preprocessing [12]. Consequently, each preprocessing step needs to be understood and considered carefully. There is a move towards developing more integrated approaches to pre-processing. At present, though, it is still common to have separate, independent pre-processing steps described in the following.

(1) Slice timing correction

At every time point, one functional volume was acquired. The functional volume was combined by slices. All the slices can be acquired within one repetition time (TR) and this procedure evenly spread over the TR. Since TR was short, the volume should be assumed that all the slices were captured at the same time. Otherwise, it would invalidate following statistical

analysis. Slice timing correction aims at adjusting slices that were acquired in different times during the same TR to a common reference time. In detail, for each slice in one TR, the temporal adjustment is usually achieved by resampling the time series of slice by applying sinc interpolation backward or forward, and taking the value at the same reference time for all the slices. Then, the value of every voxel in the volume can be considered as acquired at the same time.

(2) Realignment

The object of realignment is to determine the rigid body transformation and to best map the series of functional volumes in the common space. It estimates the six parameters of the rigid body transformation (three translations and three rotations respectively) and minimizes the mean squared difference between each successive volume and reference volume.

(3) Coregistration and normalization

Coregistration is the process of registering functional and structural images from the same subject to map functional information into anatomical space by taking the constant overall shape. Spatial normalization aims to map the human brain of different sizes into a standard template, which makes them comparable to each other and could boost the statistical power in fMRI analysis.

2.2.2 Deconvolution

The fMRI BOLD signal is the indirect measurement of neural activity and this may raise many issues when it is used as a tool in brain investigations[71] (e.g. effective connectivity [53]). Based on the model that considers fMRI signal as a filtered version of neural activity (Figure 1.3), the inversion of the modeled hemodynamic system is termed as ‘deconvolution’. This procedure

allows the extraction of HRF and estimation of hidden neuronal activation from the observed fMRI signal theoretically. The deconvolution method is an ill-posed problem since both the HRF, and the latent neural input are unknown and only the output of the convolution (fMRI signal) is measured. Therefore, the precision of the observation (such as temporal resolution, signal to noise ratio and etc.), as well as the algorithms that optimize the problem could affect the accuracy of estimation of neural activation.

(1) Deconvolution using Kalman filtering

This deconvolution method estimates the coupled dynamical systems based on nonlinear Kalman filtering [72]. The algorithm formulates a model with the continuous process equation and a discrete measurement, and applies a forward pass using the cubature Kalman filter (CKF) [73].

In detail, the method considers a discrete-time nonlinear dynamic system, where the system's hidden states cannot be observed. The state-space model for joint estimation of state and parameter is formulated as:

$$\tilde{x}_t = \begin{bmatrix} x_t \\ u_t \\ \theta_t \end{bmatrix} = \begin{bmatrix} \boldsymbol{F}(x_{t-1}, \theta_{t-1}, u_{t-1}) \\ u_{t-1} \\ \theta_{t-1} \end{bmatrix} + \begin{bmatrix} q_{t-1} \\ v_{t-1} \\ w_{t-1} \end{bmatrix} \tag{2.4}$$

$$y_t = g(\tilde{x}_t) + r_{t-1} \tag{2.5}$$

Where x_t is the state vector, θ_t is the parameter vector and u_t is the input vector; w_t is the "artificial" process noise vector, v_t input noise vector, q_t is the zero-mean Gaussian state

noise vector; y_t is the simultaneously observed noisy signal, and r_t is random Gaussian measurement noise vector.

Then the method introduces a forward pass using the of the square-root version of CKF, which is finessed by a backward pass and aims to obtain smoothed estimates of states, input and parameters. In this continuous dynamic system, the discretization of process equations of both forward pass and backward pass are discretized by a local linearization [74] scheme for all cubature points. The log-likelihood were evaluated at each iteration and the iteration would terminate when increment of the (negative) log-likelihood is less than a tolerance value. This procedure furnishes posterior estimates of both the hidden states and the parameters of a system, including any unknown exogenous input.

(2) Blind deconvolution using Wiener filter

The blind deconvolution proposed by Wu et al models the resting fMRI data as 'pseudo-events' time series with randomly occurring events [75]. The 'pseudo-events' time series is constructed by searching the local peak beyond a threshold (Figure 2.1) and is adjusted by considering the time delay in hemodynamic response following the neural activity. Then, the time series convolved by the canonical HRF is fitted into measured BOLD signal by applying the general linear model, and the noise error covariance is calculated. By searching through all integer values in the interval of time delay $[0 \ \ k_{max}]$, the time series achieves the smallest noise error covariance is chosen as the input neural activity time series $s(t)$. The $s(t)$ is formulated as following:

$s(t)=\sum_{\tau=0}^{\infty}\delta(t-\tau)$

(2.6)

Following Glover's classic deconvolution method [20], the measured BOLD signal can be described as:

$$b(t) = s(t) \otimes h(t) + \varepsilon(t) \quad (2.7)$$

where $b(t)$is the measured BOLD signal, $h(t)$ is HRF, and $\varepsilon(t)$ is the noise.

The $\tilde{h}(t)$ could be obtained by applying Wiener filter d(t):

$$\tilde{h}(t)=d(t) \otimes b(t) \quad (2.8)$$

Combine the above formulate and the Fourier transform of Wiener filter can be obtained by turning to

$$\mathrm{D}(\omega) = \frac{\mathrm{H}'(\omega)}{|\mathrm{H}(\omega)|^2+|\mathrm{N}(\omega)|^2} \quad (2.9)$$

For white noise, the spectrum is a constant and is calculated as $|N(\omega)|^2 = N_0^2$

The HRF can be estimated as

$$\tilde{h}(t)=\mathcal{F}^{-1}\{D(\omega)B(\omega)\} = \mathcal{F}^{-1}\left\{\frac{S'(\omega)B(\omega)}{|S(\omega)|^2+|N(\omega)|^2}\right\} \quad (2.10)$$

Finally, the deconvolution is performed by applying voxel specified HRF and Wiener filter back into the linear model:

The estimated neural activity could be acquired by:

$$\tilde{s}(t) = \mathcal{F}^{-1}\left\{D(\omega)\tilde{H}(\omega)\right\} = \mathcal{F}^{-1}\left\{\frac{\tilde{H}'(\omega)B(\omega)}{|\tilde{H}(\omega)|^2+|N(\omega)|^2}\right\} \quad (2.11)$$

This deconvolution method has the advantage of requiring no prior information of the neural event. Furthermore, it returns three parameters characterizing the HRF of each voxel for further HRF examination.

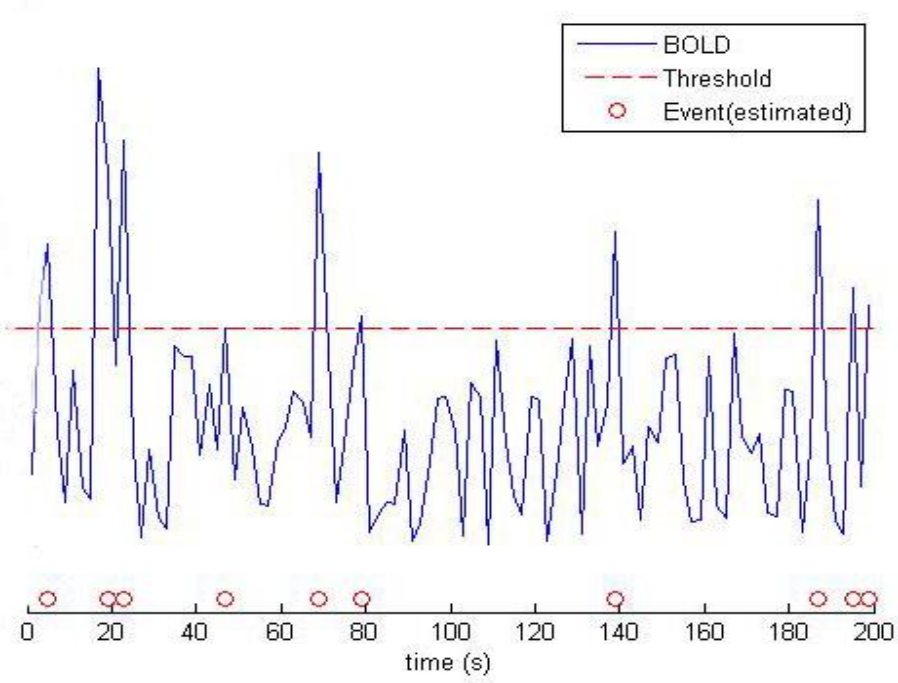

Figure 2.1 *Constructing 'pseudo-events' time series.*

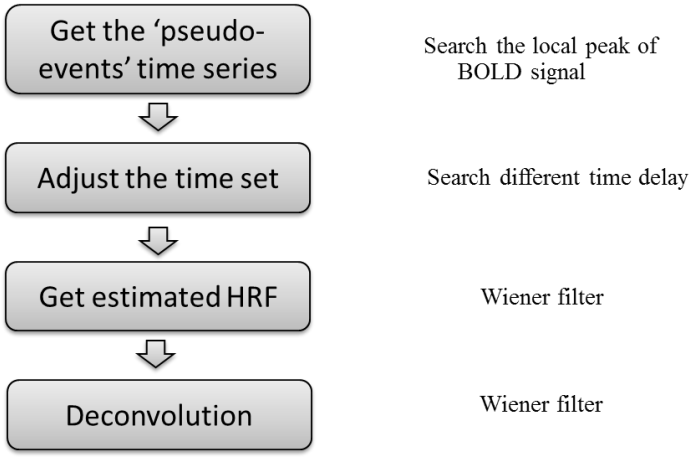

Figure 2.2 *Blind-deconvolution pipeline.*

2.3 Connectivity Analysis based on fMRI

2.3.1 The rs-fMRI Functional Connectivity Analysis

The most widely applied estimation of rs-fMRI functional connectivity is Pearson correlation coefficient [76]. It assumes these fMRI measurements conform to Gaussian assumptions and then characterizes the correlations or covariance (correlations are normalized covariance) of each voxel or the averaged time series in voxels or region of interests (ROIs）.

For two fMRI time series x, y with n observations (e.g., time points of fMRI signal), the correlation coefficient $\rho_{x,y}$ is calculated as:

$$\rho_{x,y} = \frac{cov(X,Y)}{\sigma_x \sigma_y} \tag{2.12}$$

where cov stands for the covariance, which is expressed in terms of mean and expectation:

$$cov(X,Y) = E[(X - \mu_x)(Y - \mu_y)] \tag{2.13}$$

σ_x,$\sigma_y$are the standard deviations of X, Y.

μ_x, $\mu_y$are the means of X, Y.

E is the expectation.

2.3.2 Fisher Z-transformation

Fisher's z-transformation is a statistical transformation that converts Pearson's correlation coefficient r to the normally distributed variable z [77]. Because, when the population correlation coefficient is not equal to zero, the distribution of r is somewhat skewed.

For a given population of correlation, the Fisher's z values for a sample of size n are virtually normally distributed with a variance of $1/(\mathrm{n}-3)$. Thus, the standard error of a Fisher's z transformed correlation is $1/\sqrt{n-3}$.

Fisher's z values are calculated as

$$\frac{1}{2}[\ln(1+r)-\ln(1-r)] \tag{2.14}$$

2.3.3 Dynamic Granger Causality

The Granger causality (GC) [78] is a statistical concept which infers whether the information in past variable $X=[x(1),x(2),\dots x(t)]$ could benefit the prediction of present variable $Y=[y(1),y(2),\dots y(t)]$.

The identification of causality relationship is based on statistical hypothesis. If "X" happens prior to "Y", "X" could be referred as the cause, while "Y" could be referred as the effect. When the present value of Y could be evaluated based on its own past values and the past values of another varied variable X, the X could be considered as granger-causes Y [79][80]. Therefore, the null hypothesis is stated as the X does not granger-cause Y, while the alternate hypothesis is stated as the X granger-causes Y.

To test the null hypothesis, a univariate autoregression of Y could be formulated as following

$$y(t)=a_0+a_1y(t-1)+a_2y(t-2)+\cdots a_my(t-m)+\varepsilon_1(t) \tag{2.15}$$

where m is the number of lags for Y.

For the alternate hypothesis, a multivariate autoregression of Y is augmented by including lagged values of X:

$$y_{augmented}(t) = a_0 + a_1 y(t-1) + a_2 y(t-2) + \cdots a_m y(t-m)$$

$$+b_0 + b_1 x(t-n1) + \quad b_2 x(t-1) + \cdots b_n x(t-n) + \varepsilon_2(t) \qquad (2.16)$$

where n is the number of lags for X.

The F-statistic of $6^2(y) - 6^2(y_{augmented})$ is calculated to examine whether all lagged values of x add explanatory power to the regression.

In practice, there could be more than two variables which granger-causes each other. Therefore, the multivariate granger causality analysis is usually performed by fitting GC into multivariate vector autoregressive model (MVAR) [39].

For be a k-dimensional multivariate time series. The variable vector is formulated as:

$$S(t) = [s_1(t), s_2(t), \cdots, s_k(t)] \qquad (2.17)$$

The multivariate GC model [81] is given by:

$$S(t) = A'^{(0,t)} S(t) + A'^{(1,t)} S(t-1) + \cdots + A'^{(p,t)} S(t-p) + E(t) \qquad (2.18)$$

where the model coefficients A' were estimated by using variable parameter regression [82], and *p* is an arbitrary time delay [83] which calculates the optimal set of coefficients that minimizes the model error *E(t)*. The coefficient $A'^{(p,t)}$ indicates the degree to the involvement of the past

$X(t-p)$ in predicting the present $X(t)$. The sum of all coefficients corresponding to all delays at time t is considered as Dynamic Granger Causality (DGC), and calculated as:

$$DGC_{ij}(t) = \sum_{n=1}^{p} a'_{ij}(n,t) \quad (2.19)$$

In this framework, DGC_{ij} is the strength of causal relationship from component i to component j at time instant t, where all values of component i at past p timepoint at component i together were involved in the prediction of the present value in component j. The a'_{ij} are the elements of coefficient matrix A'.

2.3.4 Visualization of Connectivity

Since the brain itself functions as a complex network, graph theoretic approaches are a natural and attractive choice for fMRI connectivity analysis. In brain functional network analysis, functional brain regions are projected as nodes and the connectivity between each pair of regions as edge. Therefore, the visualization of brain network should be considered both based on graph theory and brain structure.

(1) Directly diagram

In directly diagram, the functional units are represented as nodes and the edges are represented as straight lines, polylines, or curves on the Euclidean plane. By using arrowheads, weighted node or edges, directly connectivity diagram could carry additional information, such as orientation or classified subnetwork. The adjustability of position allows flexible network display. However, the

designed space for the visualization of weighted graphs is limited due to the use of color, and the actual structural position cannot be displayed. In addition, if diagrams represent dense graphs, it is not sufficient to encode weight and orientation of the edge.

(2) Connectivity matrix

The connectivity matrix is defined as a correlation matrix between brain functional units (voxel or ROIs). It is a square matrix, and the value of each element of the matrix indicates the weighted edges in pair-wise nodes, identified by its index of row and line. Connectivity matrix visualization is advantageous for avoiding any wasted space. Especially for a large sparse graph, it requires less storage space and the captivity of storage facilitates the encoding of additional information in cells more effectively. However, this visualized method is limited in localizing the structural position and identifying the structure of network.

(3) 3D Graph

In the 3D node-link diagrams, ROIs are shown as nodes and weighted edges denote the straight line of pair-wise nodes. Additional information can be encoded by the size or color of the nodes, and the thickness and color of the edges. The biggest advantage of the 3D graph is that all the nodes are localized in its structural position. In addition, it could facilitate the comparison by overlaying two connectivity datasets. However, images of large datasets are still cluttered and suffer from the known side effects of the 3D rendering such as occlusion. All this renders it difficult to perform accurate visualization.

Chapter 3

Aberrant Hemodynamic Responses in Autism: Implications for Resting State fMRI Functional Connectivity Studies

Abstract

Functional magnetic resonance imaging (fMRI) is modeled as a convolution of the hemodynamic response function (HRF) and an unmeasured latent neural signal. However, the HRF itself is variable across brain regions and subjects. This variability is induced by both neural and non-neural factors. Aberrations in underlying neurochemical mechanisms which control the shape of the HRF have been reported in Autism Spectrum Disorders (ASD). Therefore, we hypothesized that this will lead to voxel-specific, yet systematic differences in the shape of the HRF between individuals with Autism and healthy controls. As a corollary, we also hypothesized that such alterations will lead differences in estimated functional connectivity in the fMRI space as compared to the latent neural space. In order to test these hypotheses, we performed blind deconvolution of resting state fMRI time series acquired from large number of ASD and control subjects obtained from the Autism Brain Imaging Data Exchange (ABIDE) database. Many brain regions previously implicated in Autism showed systematic differences in HRF shape in the ASD population. Specifically, we found that the precuneus had aberrations in all HRF parameters.

Consequently, we obtained precuneus-seed-based functional connectivity differences between ASD and controls in fMRI as well as latent neural space. We report that raw fMRI data failed to detect group differences in connectivity between precuneus and certain brain regions that were however observed in deconvolved data. Our results are relevant for the understanding of hemodynamic and neurochemical aberrations in ASD, as well as have methodological implications for resting state functional connectivity studies in Autism and more generally in disorders that are accompanied by neurochemical alterations that may impact HRF shape.

Keywords: Resting-state fMRI, Deconvolution, Autism, Hemodynamic response function (HRF), Seed-based functional connectivity

3.1 Introduction

Resting-state functional magnetic resonance imaging (fMRI) is widely used to examine brain networks by investigating temporal correlations of the blood oxygen level dependent (BOLD) signals in different brain regions [84][85]. Specifically in the case of Autism Spectrum Disorder (ASD), resting state fMRI based functional connectivity studies could be used to identify potential biomarkers [86][87][88]. For example, the underconnectivity of the superior temporal sulcus that predicts emotion recognition deficits ASD have been reported [89]. Also deficits in the somatosensory, default mode, and visual regions have been highlighted in characterizing ASD [90].

Notwithstanding the strides made in understanding the neurobiology underlying ASD using resting state fMRI functional connectivity, one drawback of the method is that the BOLD signal only provides an indirect measurement of neural activity [46], i.e. the observed BOLD signal is a

convolution of latent neural activity with the hemodynamic response function (HRF). The HRF is the transfer function that broadly represents neurovascular coupling. This could raise many issues while using the BOLD signal as a tool for examining and inferring neural activity. Specifically problematic is the large variability of the HRF across subjects, as well as across brain regions in the same subject [47][48][91]. Further, the HRF seems to vary across pathological populations [57] [92] and can be influenced by the composition of the Genome [49]. With specific reference to ASD, prior studies have shown alterations in neurotransmitters which control neurovascular coupling [57], and this could potentially cause changes in the HRF. Therefore, if the HRF varies due to any factors other than underlying neural activity, it could lead to false inferences of functional connectivity because synchronicity between observed BOLD data in any two given brain regions may or may not exist in latent neural data depending on the differences in HRF shape between the two given regions (Figure 3.1) [93]. Therefore, our objective in this work is to investigate the effects of HRF variability on resting state fMRI functional connectivity estimates in the ASD population. In order to do so, we utilize blind deconvolution of resting state fMRI data [75] from ASD and control populations and characterize functional connectivity differences before and after deconvolution.

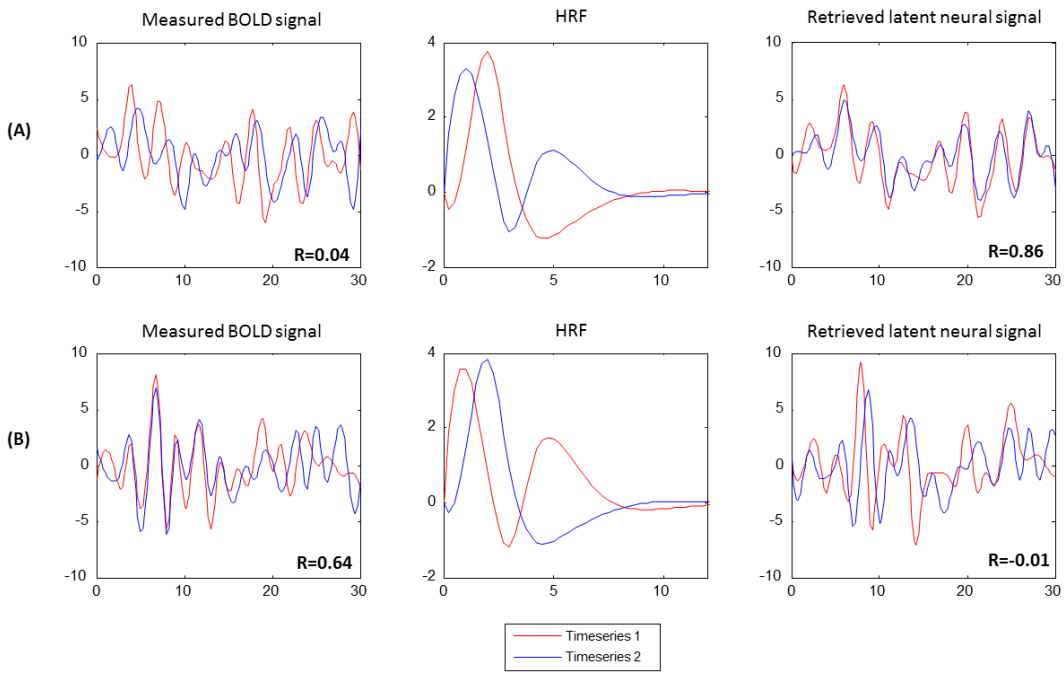

Figure 3.1 *Illustration of the impact of HRF variability on functional connectivity analysis. Both measured BOLD signal, retrieved latent neural signal and the voxel-level HRF are shown. (A) Two real fMRI data timeseries that have low correlation while the correlation between underlying neural signals is high. (B) Two real fMRI data timeseries that are highly correlated while the correlation between underlying neural signals is low. This apparent dissociation between BOLD and latent neural space is induced by the spatial variability of the HRF shape (especially, its latency), as illustrated.*

In fMRI task paradigms, the neural activity as well as the BOLD response is entrained to the external sensory input or the motor output. Hence, it is relatively straightforward to deconvolve the HRF and recover latent neural activity, as the timing of neural events is known [17][18][19]. However, this is not true in case of resting state wherein the neural events must be estimated from the data [16][96] or inferred from independent measurements of electrical activity [53] before deconvolution is performed. In this study, we employ the resting state fMRI deconvolution method proposed by Wu et al [16], which is based on assuming resting state data to be generated by neural events at random times and then performing Weiner deconvolution.

In ASD, the abnormalities of the neurotransmitters which control neurovascular coupling are well established [57][97]. Thus, we hypothesized that the HRF, which depends on cerebrovascular reactivity and neurovascular coupling, may be altered between ASD and the healthy control groups, thereby altering inferred group differences in resting state functional connectivity. We examined voxel-specified HRFs obtained by deconvolving each voxel time series and characterized group differences of HRF shape in terms of three parameters: time-to-peak (TTP), response height (RH), and full-width at half-max (FMHW) (see Figure 3.2). We determined brain regions with the significantly altered HRF between the ASD and the control groups. Further, we examined possible impacts of the altered HRF on the resting state fMRI functional connectivity differences between the groups.

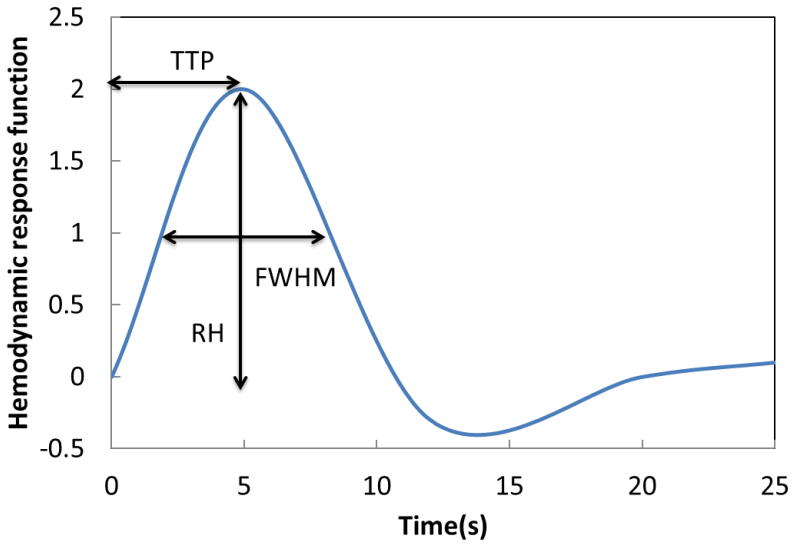

Figure 3.2 *Estimates of response height (RH), time-to-peak (TTP), and full-width at half-max (FMHW) from a simulated HRF.*

3.2 Materials and methods

3.2.1 Resting-states fMRI Data

The Autism Brain Imaging Data Exchange (ABIDE) [98] consists of resting state fMRI data from 1102 subjects contributed by 17 different institutions, including 531 individuals with ASD and 571 age- and sex-matched typical controls. Of these subjects, 739 were males, and 363 were females (Table 3.1). The data from each subject consisted of resting functional MRI acquisitions and a volumetric magnetization-prepared rapid acquisition with gradient echo (MPRAGE) image. Local Institutional Review Boards (IRBs) approved the study protocol at each institution, the subjects provided informed consent and the data was fully anonymized in accordance with Health Insurance Portability and Accountability Act (HIPAA) guidelines. Details of acquisition, informed consent, and site-specific protocols are available at http://fcon_1000.projects.nitrc.org/indi/abide/.

Table 3.1. *Gender distribution of ASD data in ABIDE acquired at 17 different institutions*.

No.	Institutions	Male	Female	Total
1	California Institute of Technology	30	8	38
2	Kennedy Krieger Institute	42	13	55
3	University of Leuven	56	8	64
4	Ludwig Maximilians University Munich	50	7	57
5	Oregon Health and Science University	28	0	28
6	University of Pittsburgh School of Medicine	49	8	57
7	Social Brain Lab UMC Groningen NIN	30	0	30
8	San Diego State University	14	24	36
9	Stanford University	20	20	40
10	Trinity College Dublin	49	0	49

11	University of California, Los Angeles	55	44	99
12	University of Michigan	117	28	145
13	NYU Langone Medical Center	79	105	184
14	Olin, Institute of Living at Hartford Hospital	20	16	36
15	University of Utah School of Medicine	58	43	101
16	Yale Child Study Center	28	28	56
17	Carnegie Mellon University	14	13	27

3.2.2 Pre-processing

The pre-processing of resting state fMRI data was performed by using Data Processing Assistant for Resting-State fMRI (DPARSF) [99] based on Statistical Parametric Mapping (SPM8) [100] and Resting-State fMRI Data Analysis Toolkit [101]. For each individual participant's data set, the first 4 image volumes were discarded. The remaining volumes underwent the following pre-processing steps. Slice time correction was performed by shifting the signal measured in each slice relative to the acquisition of the slice at the mid-point of each TR. Realignment of all the images by using the six rigid body motion parameters was followed by spatial normalization of the data to the Montreal Neurological Institute (MNI) template. Then we regressed out head motion effects from the fMRI signal with a 24-parameter (6 head motion parameters, 6 head motion parameters one time point before, and the 12 corresponding squared items) model [102]. The signals from the white matter and cerebrospinal fluid were regressed out to reduce respiratory and cardiac effects. At this point, the processing pipeline was split into two. In the first pipeline, the data was deconvolved using the method proposed by Wu et al [16], and the resulting latent neural

variables were temporally bandpass filtered in the (0.01 - 0.1 Hz) range. We will refer to this as the deconvolved (DC) dataset. In the second pipeline, the data was not deconvolved (hitherto referred to as non-deconvolved or NDC dataset), but was subjected to temporal bandpass filtering in the (0.01 - 0.1 Hz) range.

3.2.3 Blind Deconvolution and HRF Estimation

In order to characterize HRF variability in the data [48], we employed a blind deconvolution technique developed for resting state fMRI by Wu et al [75]. It is based on the idea that the resting state BOLD signal could be considered as the convolution of a voxel-specific HRF and spontaneous neural events occurring at random times [103] Spontaneous neural events were detected by picking up BOLD fluctuations of relatively large amplitude as pseudo neural events [103]. This was done after potential sources of noise were reduced or eliminated to the extent possible so that spikes contributed by noise sources were not mistaken for neural events. These pseudo-event onsets were then shifted with different delays in order to determine the delay at which the model fit was greatest. Once the pseudo-events and their onsets were determined, voxel-specific HRFs and the latent neural variables were reconstructed from the raw BOLD signal using Weiner deconvolution [20]. The estimated HRFs were characterized by three parameters: response height (RH), time-to-peak (TTP), and full-width at half-wax (FWHM).

The parameters were Z-scored. Also, a one-way ANONVA analysis was performed, and the result indicated there are no differences between parameters which acquired by the fMRI data

provided by different sites. A two-way ANONVA analysis was performed to check the interaction between group and sites, and the result indicated no interaction between group and sites.

3.2.4 Seed Region Selection

Our motive was to find brain regions that had alterations in all the three HRF parameters (TTP, FWHM and RH) in ASD compared to control subjects and use these regions as seeds to perform functional connectivity mapping with DC and NDC data. Two sample two-tailed t-tests were conducted using ASD and control samples separately for the three parameters to obtain maps indicating voxels with statistically significant difference (FDR corrected p-value<0.05, cluster size>50 voxels) between the groups. This resulted in two maps per parameter (ASD>control and control>ASD) and six maps overall. These maps were overlapped to obtain brain regions that had alterations in all the three HRF parameters. We found that this corresponded to the precuneus where in all the three HRF parameters were greater in controls compared to ASD. Therefore, precuneus was selected as the seed region of interest (seed ROI) for calculating resting functional connectivity maps with the remaining brain regions (Figure 3.4). Table 3.2 lists the details of the chosen seed region, including the Montreal Neurological Institute (MNI) coordinates of the cluster as well as cluster size.

3.2.5 Seed-based Functional Connectivity

For each participant, seed-based connectivity maps were obtained by evaluating Pearson's correlation coefficient between the mean time series from the precuneus seed ROI and the rest of

the pre-processed voxel time series in the brain. A Fisher's *z*-transform was applied to improve the normality of these correlation coefficients [104][105]. The converted *z*-score maps hereafter are referred to as "the correlation maps". This pipeline was implemented separately for the two datasets: (i) NDC: data pre-processed without deconvolution, and (ii) DC: data pre-processed with deconvolution.

3.2.6 Group-level Analyses

The z –score maps from individual subjects were entered into a random effect one-sample t-test to determine the brain regions showing significant connectivity to the precuneus within each group. They were also entered into a random effect two-sample t-test to identify the regions showing significant differences in connectivity to the precuneus between control and ASD groups [106]. These procedures were also implemented separately for both DC and NDC datasets.

3.2.7 The Effect of Deconvolution

To investigate the effect of deconvolution on between-group differences in functional connectivity, a two-way repeated-measures ANOVA was performed within each voxel connected with the precuneus seed. We considered the groups (Control and ASD) as one factor and with/without applying deconvolution as the other factor. The voxels showing a significant interaction between the two factors (FDR corrected, $p<0.05$) were identified. Statistical tests were performed using SPSS (version 20, IBM Inc., USA).

3.3 Result

3.3.1 Inter-group HRF Differences

We found that the bilateral inferior occipital gyrus and precuneus had significantly higher RH (Figure 3.3A) in the control group while the middle frontal gyrus and bilateral rectus had significantly ($p<0.05$ FDR corrected) higher RH (Figure 3.3B) in the ASD group. The bilateral parietal lobule, bilateral rectus, supramarginal gyrus, superior temporal gyrus, and precuneus exhibited significantly higher FWHM (Figure 3.3C) in the control group while the middle temporal gyrus exhibited significantly higher FWHM (Figure 3.3D) in the ASD group. The left lingual gyrus and precuneus showed significantly higher TTP (Figure 3.3E) in the control group. Detailed information such as cluster sizes, cluster centroids etc. are represented in Table 2. We found that only one cluster within the precuneus showed alterations in all three HRF parameters (Figure 3.4) (note: RH, TTP and FWHM were higher in Control group in this region compared to ASD).

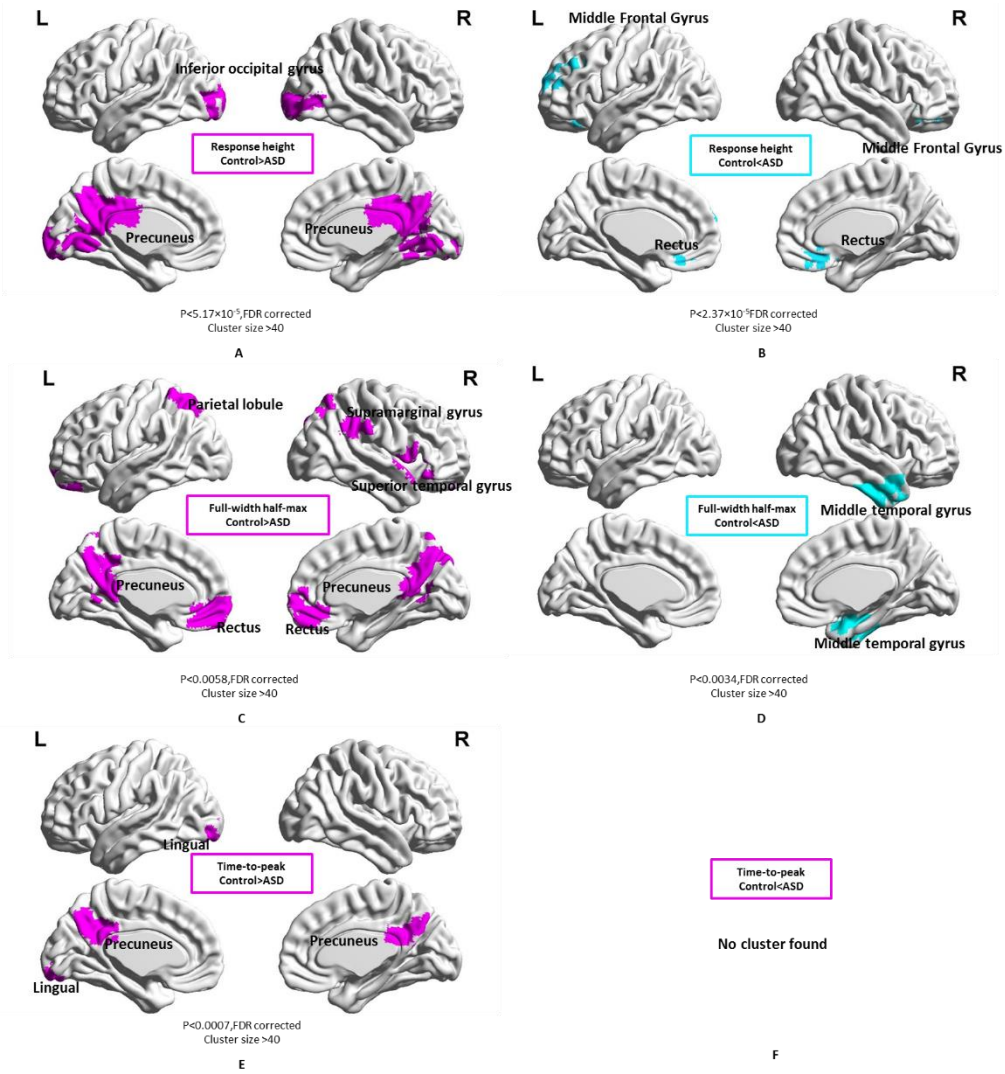

Figure 3.3 *Spatial maps showing regions with significantly different HRF parameters in ASD as compared to the control group. (A) Response height, Control>ASD (B) Response height, ASD>Control, (C) FWHM, Control>ASD, (D) FWHM, ASD>Control, (E) Time-to-peak, Control>ASD (F) Time-to-peak, Control<ASD*

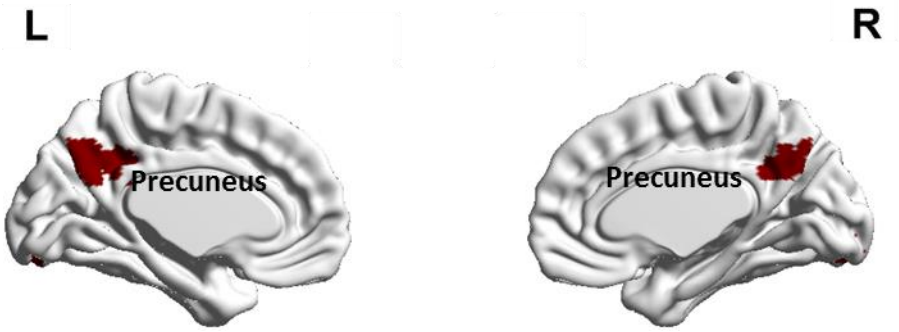

Figure 3.4 *The cluster within the precuneus which showed alterations in all three HRF parameters with RH, TTP and FWHM being higher in Controls compared to ASD*

Table 3.2. *Voxel clusters which had significantly (p<0.05 FDR corrected) different HRF parameters in control versus ASD subjects. The anatomical labels, MNI co-ordinates of cluster centroid, cluster size and corresponding Brodmann areas are listed*.

Comparison	Coordinates			Cluster size	Cluster anatomical location	Hemisphere	Brodmann area
	x	y	z				
Full-width at half max Control>ASD	-27	9	51	109	Superior Parietal Gyrus	Left	7
	-3	-51	16	153	Precuneus	Bilateral	29 30 3130
	24	-68	51	85	Superior Parietal Gyrus	Right	7
	1	51	-15	178	Rectus	Bilateral	10 11
	64	-36	53	42	SupraMarginal Gyrus	right	40
	57	6	-3	54	Superior Temporal Pole	right	22 38
Full-width at half max Control<ASD	39	9	-39	85	Middle Temporal Pole	right	21
Response height Control>ASD	-30	-90	-12	180	Inferior Occipital Gyrus	Left	17 18 19
	3	-57	20	1020	Precuneus	Bilateral	31 23 30 7 18 19
	27	-90	-12	140	Inferior Occipital Gyrus	Right	17 18 19
Time-to-peak Control>ASD	-15	-90	-16	109	Lingual	Right	18
	9	-57	18	122	Precuneus	Bilateral	31 7
Response height Control<ASD	12	34	-20	236	Rectus	Right	11 25 47
	-8	30	-22	182	Rectus	Left	11 25 47
	38	32	-18	158	Inferior Frontal Gyrus	Right	11
	-20	62	24	308	Superior Frontal Gyrus	Left	9 10
Region of overlap	-3	-60	27	50	Precuneus	Bilateral	31

* Coordinates referring to the center of the cluster, in the MNI Space.

* Anatomical labels based on Automated Anatomical Labeling (AAL).

3.3.2 Precuneus-based Functional Connectivity within Groups

In the NDC dataset, positive functional connectivity between the precuneus seed and bilateral angular gyrus were observed in both control and ASD groups (Figures 3.5B and 3.5D). For the control group, the positive functional connectivity between precuneus and the medial frontal lobe as well as negative functional connectivity between precuneus and right superior temporal gyrus (also containing a bit of the Insula) were detected, while these were not detected in the ASD group.

In the DC dataset, more clusters significantly connected with the precuneus were detected in both groups (Figures 3.5A and 3.5C). In the ASD group, in addition to precuneus – bilateral angular gyrus connectivity that was observed with NDC data, additional significant positive functional connectivity between precuneus and the medial frontal gyrus was detected. Likewise, in the control group, functional connectivities identified with NDC data were also identified using DC data. Additionally, positive functional connectivity between the precuneus and right middle temporal gyrus as well as negative functional connectivity with right supramarginal gyrus and bilateral insula were also detected. It is noteworthy that for regions identified to be functionally connected to precuneus in both DC and NDC datasets, those obtained from the DC dataset had a larger spatial extent (Table 3.3).

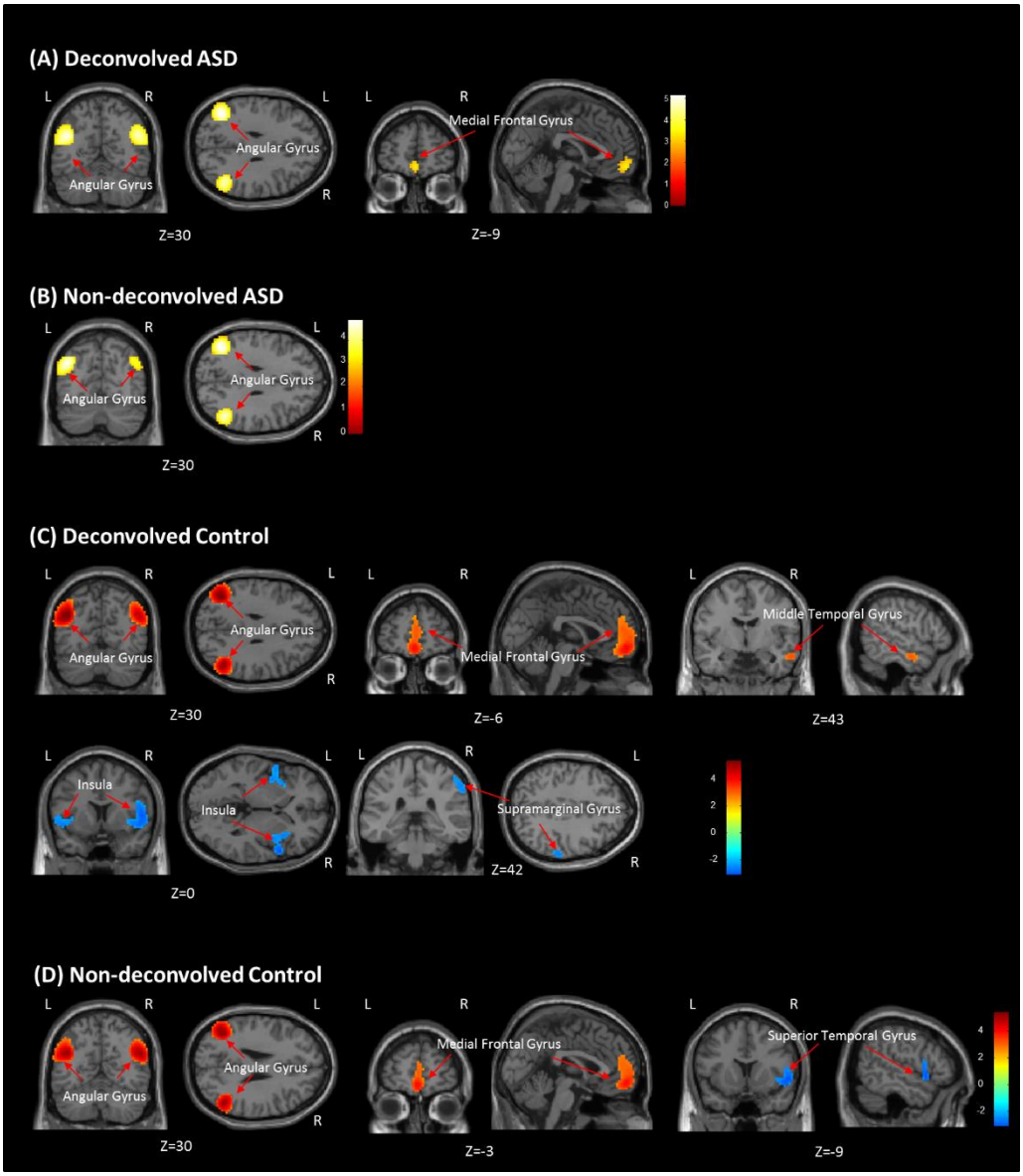

Figure 3.5 *Within group functional connectivity maps with precuneus seed. (A) Deconvovled ASD group. (B) Non-deconvovled ASD group. (C) Deconvovled Control group. (D) Non-deconvolved Control group. Red indicates area of the significant positive functional connectivity while blue indicates significant negative functional connectivity.*

Table 3.3 *Anatomical labels, cluster size and z-score of local maxima in brain areas showing significant (p-value < 0.05 FDR corrected) functional connectivity with precuneus in the control and ASD groups, for both deconvolved and non-deconvolved datasets.*

Cluster anatomical location	Peak coordinates			Cluster size	Peak intensity (z)	Hemisphere	Brodmann area
	x	y	z				
Deconvolved ASD							
Angular Gyrus	48	-60	30	365	4.59	Right	39 40
Angular Gyrus	-42	-63	30	464	5.16	Left	19 39 40
Medial Frontal Gyrus	0	57	-9	61	3.28	Bilateral	11
Non-deconvolved ASD							
Angular Gyrus	48	-60	30	315	4.47	Right	39 40
Angular Gyrus	-42	-63	30	418	4.88	Left	19 39 40
Deconvolved Control							
Angular Gyrus	-42	-66	33	460	5.12	Right	39 40
Angular Gyrus	51	-60	27	611	5.50	Lleft	7 19 39 40
Medial Frontal Gyrus	0	57	-12	409	4.05	Left	9 10 11 32
.Middle Temporal Gyrus	60	-6	-21	56	3.28	Right	21
Insula	54	12	-3	220	-3.34	Right	13 22 44
Insula	-33	15	3	116	-2.94	Left	13 22
Supramarginal Gyrus	60	-30	42	54	-2.95	Right	2 40
Non-deconvolved Control							
Angular Gyrus	51	-63	30	383	4.86	Right	39 40
Angular Gyrus	-42	-66	33	554	5.35	Left	7 19 39 40
Medial Frontal Gyrus	0	57	-12	243	3.82	Bilateral	10 11
Superior Temporal Gyrus	54	12	-3	99	-3.06	right	22

* Coordinates referring to the peak of the cluster in MNI Space.

* Anatomical labels are based on Automated Anatomical Labeling (AAL)

* Z-value is the mean across the group.

3.3.3 Precuneus-based Connectivity Differences between Groups

We quantified the differences in functional connectivity of the precuneus between ASD and control groups, using both DC and NDC datasets. In the NDC dataset, the superior temporal gyrus

showed higher negative connectivity with precuneus in the control group, while bilateral angular gyrus and medial frontal gyrus showed higher positive connectivity in the control group compared to ASD (Figure 3.6, Table 3.4). In the DC dataset, the superior temporal gyrus, insula and right supramarginal gyrus showed higher negative connectivity with precuneus in the control group while bilateral angular gyrus, medial frontal gyrus and right middle temporal gyrus showed higher positive connectivity in the control group compared to ASD (Figure 3.6, Table 3.4).

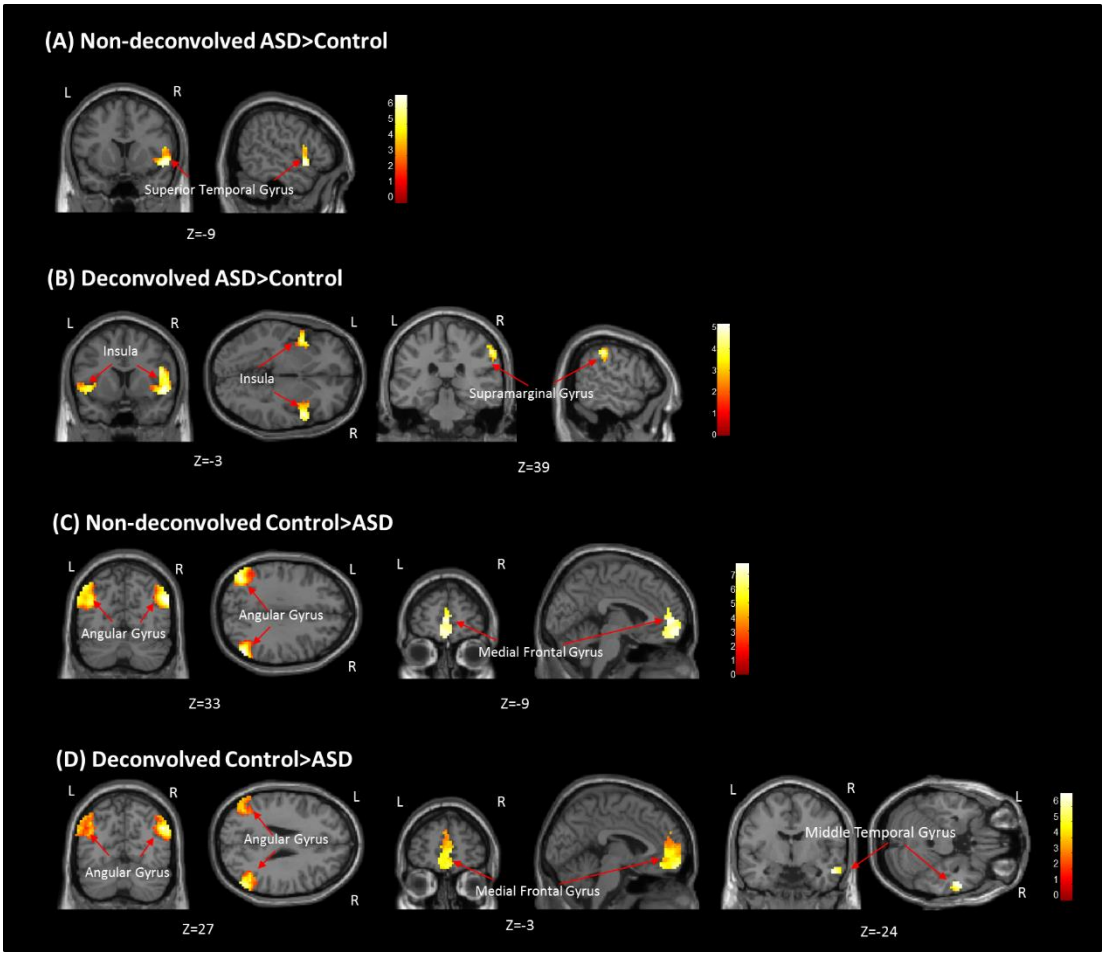

Figure 3.6 *Between-group (ASD vs. control) differences in functional connectivity maps estimated from a seed in precuneus. Results are shown from both DC and NDC datasets. (A) Non-deconvovled ASD>Control (B) Deconvovled ASD>Control (C) Non-deconvovled Control >ASD (C) Deconvovled Control>ASD*

Table 3.4. *Anatomical labels, cluster size and t-score of local maxima in brain areas showing significant between group (ASD vs. control) differences (p-value<0.05 FDR corrected) in functional connectivity with precuneus, for both deconvolved and non-deconvolved datasets.*

Cluster anatomical location	Peak coordinates			Cluster size	Peak intensity (t)	Hemisphere	Brodmann area	Z-score in ASD	Z-score in Control
	x	y	z						
Non-deconvolved Control>ASD									
Superior Temporal Gyrus	54	9	-4	99	6.32	Right	22	-2.45	-2.59
Deconvolved ASD>Control									
Insula	-44	7	-3	214	5.31	Right	13 22 44	-2.77	-3.34
Insula	-45	6	-3	103	4.90	Left	13 22	-2.61	-2.94
Supramarginal Gyrus	57	-33	44	54	4.89	Right	40 2	-2.43	-2.95
Non-deconvolved Control>ASD									
Angular Gyrus	57	-63	27	212	5.39	Right	39 40	4.47	4.86
Angular Gyrus	-42	-75	42	337	4.99	Left	7 19 39 40	4.88	5.35
Superior Frontal Gyrus	-3	54	3	243	6.77	Bilateral	10 11	2.93	3.82
Deconvolved Control>ASD									
Angular Gyrus	54	-66	30	282	5.70	Right	39 40	4.59	5.12
Angular Gyrus	-42	-75	42	348	4.59	Left	7 19 39 40	5.16	5.50
Superior Frontal Gyrus	3	60	-13	409	6.76	Bilateral	9 10 11 32	3.28	4.05
Middle Temporal Gyrus	54	-3	-24	56	6.81	Right	21	2.51	3.28

* Coordinates referring to the peak of the cluster in MNI Space.

* Anatomical labels based on Automated Anatomical Labeling (AAL)

* Z-value is the mean across the group.

3.3.4 The Effect of Deconvolution

Voxels in left medial frontal gyrus, left cuneus, right angular gyrus and bilateral postcentral gyrus showed a significant ($p<0.05$ FDR corrected) interaction effect between groups and deconvolution (Figure 3.7, Table 5). This means that group differences between ASD and Controls in these regions would be inferred differently in DC and NDC data.

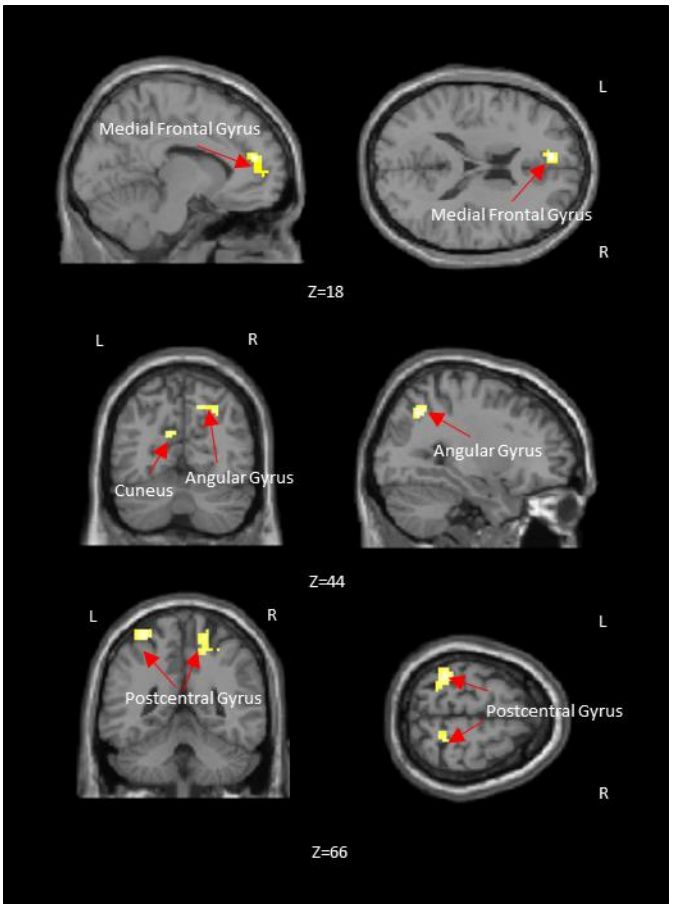

Figure 3.7 *The brain regions showing significant (p-value<0.05, FDR corrected) interaction between groups (ASD and control) and with/without applying deconvolution.*

Table 3.5. *Anatomical labels, cluster size and p-value of local maxima in brain areas showing significant interaction (p-value<0.05, FDR corrected) between groups (ASD and control) and with/without applying deconvolution method.*

Cluster anatomical location	Peak coordinates			Cluster size	Hemisphere	Brodmann area
	x	y	z			
Medial Frontal Gyrus	-6	48	18	68	Left	10
Cuneus	-9	-69	24	31	Left	31
Angular gyrus	30	-63	42	34	Right	
Postcentral Gyrus	33	-39	51	78	Right	
Postcentral Gyrus	-27	-44	66	53	Left	5

* Coordinates referring to the peak of the cluster in MNI Space.

* Anatomical labels based on Automated Anatomical Labeling (AAL).

3.4 Discussion

In this study, we test the hypothesis that the HRF is altered in individuals with ASD as compared to controls and this could lead to differences in resting state functional connectivity estimated in the latent neural space as compared with that obtained from raw BOLD data. In order to do so, we estimated the HRF at each voxel using a blind deconvolution technique and characterized significant differences in HRF characteristics such as RH, FWHM and TTP. Further, resting state functional connectivity maps obtained from DC and NDC data had significant differences and this impacted inferences about group differences derived from resting state connectivity analysis. These results seem to confirm scenarios such as the ones shown in Figure 3.1 do occur in experimental data. Therefore, we feel that it is desirable to perform resting state

functional connectivity analysis in the latent neural space than with BOLD data so that the uncertainty introduced by the variability of the HRF is taken care of.

The shape of the HRF is controlled by both non-neural and neural factors. The non-neural factors which impact the shape of the HRF include vasculature differences, baseline cerebral blood flow, hematocrit, alcohol/caffeine/lipid ingestion, partial volume imaging of veins, global magnetic susceptibilities, slice timing differences and pulse or respiration differences[50][51][52][47]. These factors induce HRF differences across both brain regions and subjects. Such differences seem to be random and will likely cancel out when we look at systematic differences between groups of subjects [47]. Therefore, the systematic differences in the shape of the HRF observed between ASD and controls are at least partly due to underlying neural factors that control the HRF shape.

A comprehensive account of neural factors that control the shape of the HRF is beyond the scope of this report. However, we will discuss neurochemicals that have been shown to affect the shape of the HRF and then link them with independent reports of altered neurochemistry in Autism. Figure 3.8 shows various neurochemicals which control the coupling between neural activity and blood flow [4]. The demand for energy due to neural activity is coupled to blood flow changes by signaling pathways controlled by various neurochemicals that directly or indirectly mediate vasodilation or vasoconstriction. HRF is a mathematical transfer function which represents this coupling and hence could be altered as a consequence of changes in any of these neurochemicals. Specifically, glutamatergic and GABAergic interneurons impact the HRF [107] by releasing

neuromodulators which control local cerebral blood flow [108][109]. In brain regions with low concentrations of GABA [110], taller, quicker and narrower HRFs have been observed previously. Also, local activation of brain regions cause blood vessel dilation, which is mediated by glutamatergic actions on N-methyl-D-aspartate (NMDA) receptors [111]. Therefore, we concentrate on abnormalities in GABA, serotonin, nitric oxide (NO) and glutamate in ASD (as indicated in Figure 3.8).

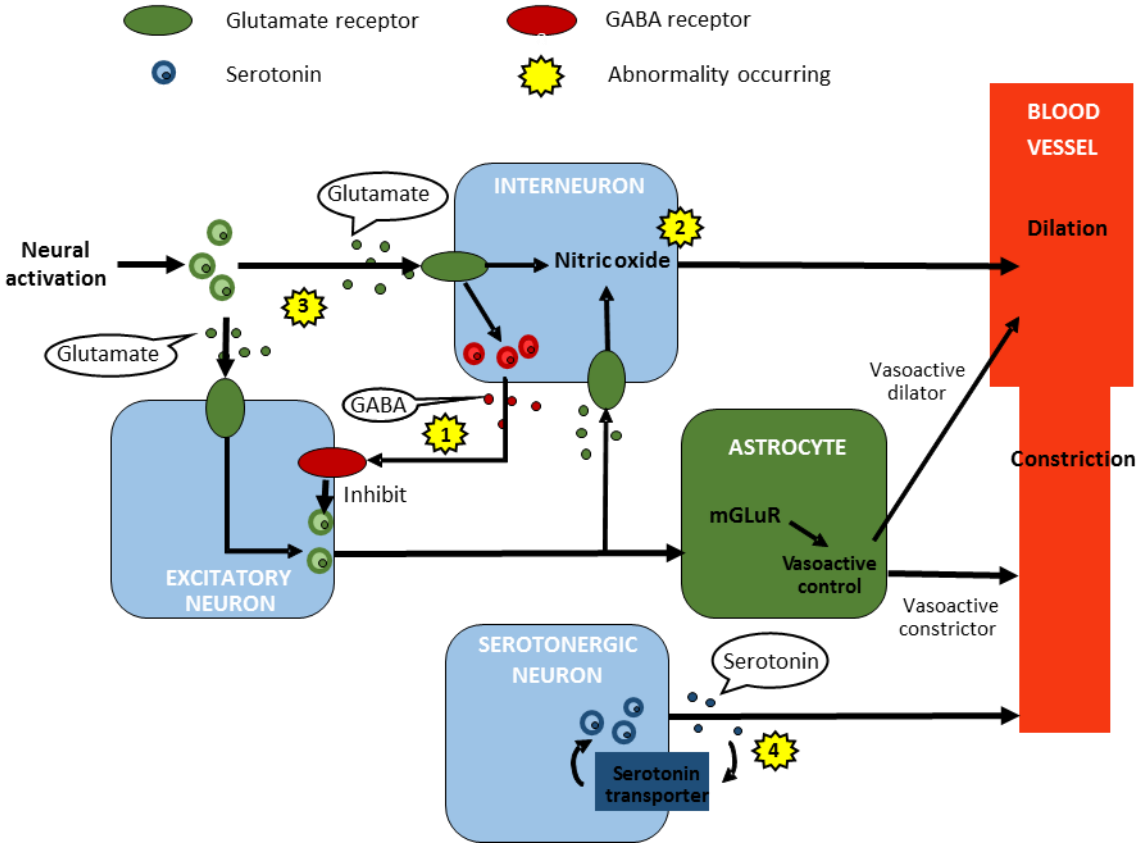

Figure 3.8 *A schematic illustrating how various neurochemicals control the coupling between neural activity and blood flow. Abnormalities in GABA (shown as 1), nitric oxide (shown as 2), glutamate (shown as 3) or serotonin (shown as 4) in the ASD population may impact the shape of the HRF.*

The resting GABA concentration has been shown to be correlated with the amplitude of the hemodynamic response [112][113]. We found that the bilateral inferior occipital gyrus and the

precuneus exhibited higher RH in the control group (Fig 3.3A, Table 3.2) while the bilateral rectus, right inferior frontal gyrus and left superior frontal gyrus (Figure 3.3B, Table 3.2) exhibited higher RH in the ASD group. Reduced GABA concentration in the frontal lobe has been reported in individuals with ASD [114]. Also, down regulation of GABA receptors in the superior frontal cortex has also been previously found in autistic subjects [115]. This could potentially explain why disinhibition from reduced GABA might have led to higher RH in ASD in the frontal cortex. Another study showed that when a bumetanide treatment was applied to reinforce GABAergic inhibition in ASD patients, it resulted in the enhanced activation of brain regions involved in the social and emotional perception, including the inferior occipital cortex and the precuneus [116]. This supports the fact that we found increased RH in these regions, which might have been due to inadequate amount of GABA in the inferior occipital cortex and the precuneus.

Muthukumaraswamy et al showed that the GABA concentrations were positively related with the width of HRFs [117]. In our study, the FWHM of the HRF in the frontal lobe was lower in the ASD group (Figure 3.3C), in addition to reduced RH as discussed above, alluding to the possibility of lower GABA in the frontal lobe in ASD impacting FWHM of the HRF as well. The supramarginal gyrus (BA 40) [118], and parietal lobule [115] was reported to exhibit significant down-regulation of GABA receptors. Although the relationship between GABA receptors and GABA concentration is complex, they have been shown to be correlated [119].

Serotonin is a vasoconstrictor that provides blood-brain barrier permeability [8] and plays a critical role in neurovascular coupling. The role of serotonin in controlling the shape of the HRF is complex given our lack of complete understanding of its production [120], uptake [121] and reuptake [121][122]. Altered serotonin levels have been confirmed in ASD [123]. The aberrant serotonin signaling pathways [124], including aberrations in serotonin transporters [125][126], cortical serotonin synthesis [127], and serotonin receptors [128], have been reported in individuals with ASD, and could potentially lead to changes in HRF shape. The brain regions where these serotonergic aberrations were reported are also consistent with our results. For example, the precuneus (BA31) (Figures 3.3A, C, and E) was reported to exhibit reduced serotonin transporters in ASD subjects [129]; altered serotonin system was reported in the frontal cortex (Figures 3.3B and C) of animal models of ASD [130]; the serotonin transporter binding in children with ASD was reduced in the frontal and temporal lobes (Figures 3.3C and D) [131]; and the right lingual gyrus (Figure 3.3E) was indicated to be associated with the serotonin abnormalities in the ASD patients in an acute tryptophan depletion study [129]. It is noteworthy that the superior temporal gyrus [132], and middle temporal gyrus [133][134] are implicated in processing anxiety, which is an important symptom in ASD [135]. Concomitantly serotonergic alterations have been implicated in anxiety of humans as well as in animal models [64][137]. Our result in fact reinforces this relationship.

Nitric oxide is a vasodilator [138], and its role in neurovascular coupling has been demonstrated before [139]. Aamand et al reported that the intake of dietary nitrate, which induced

a reduction of cerebral NO, was found to be related to alterations in the shape of the HRF [140]. A global increase in the level of NO has been implicated in the pathology of ASD [141][142][143]. Studies have confirmed that altered levels of NO are related to sensory-motor dysfunction [144][145][146][147], which is also an important symptom observed in ASD [148][149]. We found larger FWHM of HRFs in the posterior parietal cortex and supramarginal gyrus of ASD patients (Figure 3.3C). First, it is noteworthy that these regions are involved in sensorimotor [150] and somatosensory association functions [151][152][153], respectively. Second, the above literature indicates that HRF alterations in sensorimotor regions, aberrations of NO and sensorimotor deficits in ASD may be related.

Glutamate acts on astrocytes through glutamate receptors that are located on them. It triggers astrocytes to release several vasoactive messengers, which can either increase or decrease blood flow [9]. Therefore, aberrations in glutamate level and/or glutamate receptors on astrocytes could potentially alter neurovascular coupling and the shape of the HRF. Increased glutamate concentration [114] and abnormal glutamate receptor levels [154] have been demonstrated in subjects with ASD in the frontal cortex, and this could potentially contribute to alterations of HRF shape in the frontal cortex as observed by us (Figure 3.3C). Aberrant astrocytic mechanisms [155] were also detected in the frontal lobe of autistic subjects. Since the precise relationship between glutamate concentration, glutamate receptor level and astrocytic expression remains unclear, it is difficult to provide a more mechanistic explanation of the effect of these neurochemicals and associated signaling pathways on HRF parameters.

Since the precuneus showed alterations in all three HRF parameters, we chose that region as the seed for functional connectivity analysis. It is noteworthy that precuneus is a core regions of the Default-Mode Network [156][157][158][159]. Therefore, by using precuneus as the seed, in effect, we obtained the DMN in ASD and controls using both DC and NDC datasets. The between-group differences obtained from both datasets were largely consistent with those obtained from previous studies [98][160][161][162][163][164][165]. Since these functional network alterations in Autism have been well established and discussed in detail in these previous reports, we will not elaborate on them further here. However, it is noteworthy that deconvolved data showed additional regions in both within group and between-group comparisons (Figures 3.5 and 3.6). For example, the connectivity of the frontal lobe with the precuneus in the ASD group was detected in the DC but not the NDC dataset (Figure 3.5). Even when regions were identified using both DC and NDC datasets, the clusters obtained from the DC dataset tended to be larger in spatial extent (Table 3.3). Sometimes, this shifted the peak co-ordinates of the clusters. For example, right superior temporal was detected to be significantly and negatively correlated with the precuneus in the Control group in the NDC dataset (Figure 3.5C), while in the DC dataset, the peak was found in the right insula (Figure 3.5D).

S. Zhang and C. shan R. Li [158] has examined the resting-state connectivity pattern of precuneus. Their result included the negative connectivity with bilateral insula and right supramarginal gyrus and positive connectivity with right middle temporal gyrus. Due to the confounds brought by HRF, these paths in control group were not detected in UDC dataset, then

it causes the confounds in detecting the altered path between groups. The right supramarginal gyrus has been found related to emotion processing [166]. In resting-state, it represents a hub in ventral attention network and less impaired in ASD in contrast to the default mode network[45][167][168]. The insula was emphasized in interoception and its abnormalities would cause affective symptom (e.g. somatic complaints) [169]. Together with precuneus, insula actives in self-attributional processes[170]. Since the negative correlation could be related to neural inhibition [171][172], we assumed the precuneus suppresses these regions during resting-state in control group, while in ASD group, we can't observed these suppressions. A study reported that bilateral insula exhibit negative bias in interpreting interpersonal feedback [169], this may be related to the loss of the negative bilateral insula-precuneus paths in ASD. Although no further explanation for negative right supramarginal gyrus-precuneus were found. These negative correlations are likely related to specific resting-state brain functions and reflecting the underlying pathology of ASD. The temporal cortex belongs to the subsystem of DMN, and could be related to retrieval of social semantic and conceptual knowledge[159], which is also related to the symptoms of ASD. Therefore, the positive right middle temporal-precuneus is likely a byproduct of DMN and reflects unconscious brain function which impaired in ASD.

Using repeated-measures ANOVA, we investigated whether brain regions show an interaction between group and deconvolution factors, i.e. whether significant differences between ASD and control groups are themselves significantly different between DC and NDC datasets. We found that the connectivity between the precuneus seed and the following regions – left medial frontal

gyrus, left cuneus, right angular gyrus and bilateral postcentral gyrus (Figure 3.7, Table 3.4) – showed this interaction effect. This shows that functional connectivity group differences in these regions would be inferred differently in DC and NDC datasets. This finding reinforces the point that we would be better off performing functional connectivity analysis in the latent neural space using NDC data than in BOLD space using raw data so that our inferences are not confounded by HRF variability.

Finally, we present some limitations of this study and point towards future directions which could address those limitations. First, we estimated the effect of HRF variability using seed-based functional connectivity using a precuneus seed. We did this since the precuneus showed alterations in all three HRF parameters. However, one could investigate the effect of voxel-wise HRF variability on voxel-wise functional connectivity differences between controls and ASD at the whole brain level. Second, we have discussed various neurochemical alterations in ASD and how they could have influenced the shape of the HRF. These inferences are indirect at best, since we did not directly measure the concentration of those neurochemicals. Such an endeavor, using noninvasive *in vivo* methods such as magnetic resonance spectroscopy in humans as well as invasive methods in animal models, could provide evidence that is more direct and further validate our observations.

Chapter 4

Characterization of Hemodynamic Alterations in Schizophrenia and Bipolar Disorder and their Effect on Resting-state Functional Connectivity

Abstract

Schizophrenia (SZ) and bipolar disorder (BP) have both common and distinct clinical symptomatology. Their neural bases have been explored using functional connectivity between brain regions using resting-state functional magnetic resonance imaging (rs-fMRI). However, fMRI is an indirect measure of neural activity and is modeled as a convolution of the hemodynamic response function (HRF) and latent neural activity. The HRF varies across both individuals and different brain regions within an individual. Consequently, it is plausible for two brain regions to appear synchronized in the BOLD space while being desynchronized in latent neural space and vice versa. In order to address this issue, we estimated voxel-specific HRFs by deconvolving rs-fMRI time series obtained from SZ (N=19), BP (N=35) and matched healthy individuals (N=34). The shape of the HRF was significantly different between the three groups in many regions previously implicated in SZ and BP. Specifically, we found voxels within the mediodorsal, habenular and central lateral nuclei of the thalamus to have HRFs with aberrations in all three of

its shape parameters: time to peak, response height and full width half max. Therefore, we defined this region as the seed, estimated seed-based functional connectivity maps in all three groups and characterized pairwise differences between them. Further, we performed a 2-way ANOVA and estimated regions exhibiting an interaction between the group and deconvolution factors. Results indicated that functional connectivity differences between the groups are inferred significantly differently with raw BOLD and deconvolved latent neural time series. Since the variability of the HRF could be driven by both neural and non-neural factors, we feel that it is preferable to estimated functional connectivity using deconvolved data. Finally, we discuss the role of neurochemicals such as GABA, glutamate, serotonin and nitric oxide in controlling neurosignaling pathways underlying neurovascular coupling, and how previously documented alterations of these neurochemicals in SZ and BP could, at least in part, explain the significant differences in HRF shapes observed between the groups.

Keywords: Resting-state fMRI, Deconvolution, Schizophrenia, Bipolar disorder, Hemodynamic response function (HRF), Seed-based functional connectivity.

4.1 Introduction

Schizophrenia (SZ) and bipolar disorder (BP) share significant overlap in clinical symptoms and neural characteristics [173][174][175]. SZ is a psychotic disorder characterized by altered perception, thought processes, and behaviors [176]; while BP is a mood disorder involving prolonged states of depression and mania [177]. A popular noninvasive method for characterizing the neural basis of SZ and BP is resting state functional magnetic resonance imaging (rs-fMRI)

based on the blood-oxygen-level dependent (BOLD) contrast. A primary reason for the popularity of rs-fMRI is that it does not require the subjects to perform an explicit task, which can be difficult in clinical populations. Rs-fMRI also allows us to investigate interactions between neurophysiological events in spatially remote brain regions by assessing the temporal correlation of their respective BOLD signals [178]. This is often referred to as resting state functional connectivity. It is used to characterize large-scale brain networks both in healthy and clinical populations. Specifically, to date, a number of studies have employed rs-fMRI functional connectivity in order to understand both shared and distinct neural alterations in SZ and BP as compared with healthy controls. For example, resting state connectivity related to the medial prefrontal cortex [44] and the anterior cingulate [179] have been shown to be altered in both SZ and BP. On the other hand, Meda et al reported that the connectivity between fronto-premotor and meso/paralimbic networks were reduced only in SZ, while connectivity between fronto-temporal and paralimbic networks were increased only in BP [180]. Similarly, Chai et al [44] reported that the decoupling of functional connectivity between the medial prefrontal cortex and insula/ventral lateral prefrontal cortex distinguished BP from SZ. Despite much progress, the diagnostic value of these observations remains to be demonstrated using larger samples so that they can have predictive ability at the individual subject level.

In spite of the understanding of the substrates underlying neurobiological differences between SZ, BP and healthy individuals gained from resting state fMRI, we highlight an under-appreciated issue in interpreting findings from rs-fMRI functional connectivity given that the fMRI blood

oxygenation level dependent (BOLD) contrast is an indirect measure of neural activity [46][13]. The measured BOLD signal is considered as a convolution of the latent neural activity with a transfer function – the hemodynamic response function (HRF) [20]. The issue however is that the shape of the HRF has been shown to vary not only across subjects, but also across different brain regions in the same subject [47][48]. Different factors contribute to this variability. First, it could be partly driven by differences in various neurochemicals (and associated neurosignalling pathways) controlling neurovascular coupling such as γ-aminobutyric acid (GABA), glutamate, serotonin and nitric oxide [4]. Second, it could be influenced by genetic factors [49]. Third, it could at least in part be driven by variability in non-neural factors such as baseline cerebral blood flow, vasculature differences, caffeine/alcohol/lipid ingestion, partial volume imaging of veins, hematocrit, pulse or respiration differences, global magnetic susceptibilities and slice timing differences [50][51][52]. Therefore, HRF variability could lead to two consequences: (i) It could confound functional connectivity estimates obtained from raw BOLD data. Specifically, raw BOLD data may appear to be synchronized when the underlying latent neural signals are not and vice versa [93]. (Figure 4.1) and this is problematic when HRF differences between voxels/subjects are driven by non-neural factors; (ii) HRF differences due to non-neural factors tend to be distributed randomly and when assessing systematic differences in HRF shape between clinical groups, differences in estimated functional connectivity may be driven by pathological alterations of neurochemicals controlling the neurovascular coupling (and hence HRF shape) in such groups. Specifically with reference to SZ and BP, prior studies have shown alterations in neurotransmitters

which control neurovascular coupling including GABA [58][59], nitric oxide level [63][60][181][182], serotonin [61][183][64] and glutamate[184][185][62][65], and this could potentially cause alterations in the shape of the HRF,.

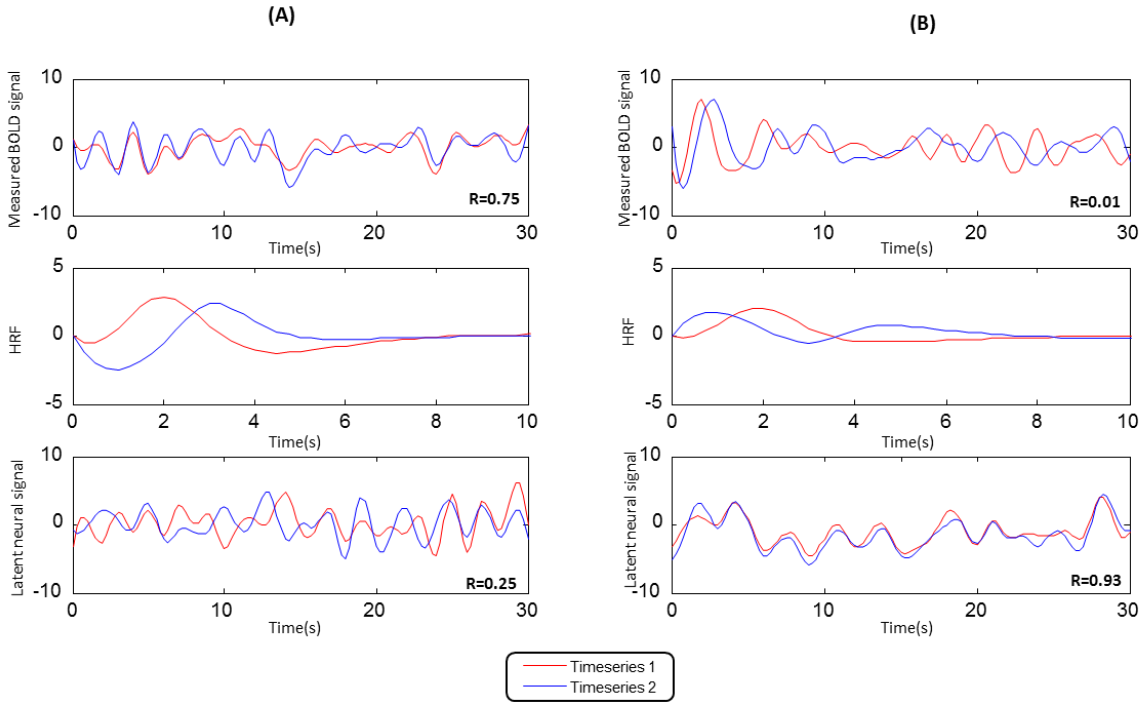

Figure 4.1. *The effect of HRF variability on Pearson's correlation between two timeseries obtained from experimental fMRI data. The measured BOLD signal, the estimated HRF and the deconvolved BOLD fMRI (or latent neural) timeseries are shown in the top, middle and bottom rows respectively. We specifically illustrate two scenarios: (A) The acquired BOLD fMRI time series are highly correlated before applying deconvolution while the correlation between underlying latent neural signals is low, and (B) The acquired BOLD fMRI time series are uncorrelated before applying deconvolution while the correlation between underlying latent neural signals is high.*

Many deconvolution methods are capable of recovering latent neural activity and voxel-specific HRFs from the measured BOLD signal [20][95]. The procedure is relatively straightforward for fMRI task paradigms because the timing of external events driving neural activity is known [72][186]. For resting state, which lacks external sensory input and explicit time

of neural events [75][96], Wu et al. [75] proposed a deconvolution method to address this scenario and we have used it in the current work. The voxel-specified HRFs were obtained by deconvolving time series at the voxel-level and were characterized in terms of three parameters: time-to-peak (TTP), response height (RH), and full-width at half-max (FMHW) (see Figure 4.2).

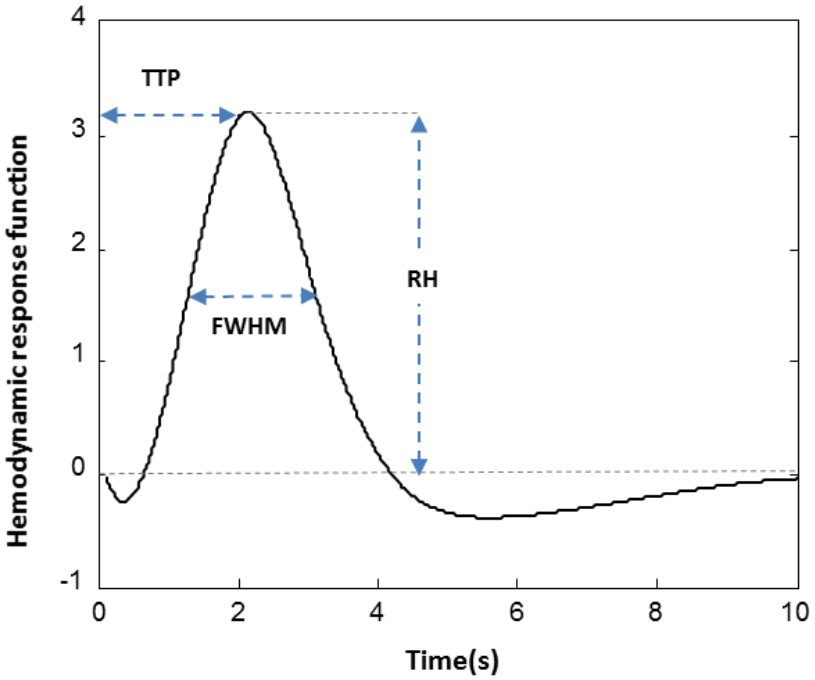

Figure 4.2. *Typical HRF with its three characteristic parameters.*
RH: response height; TTP: time-to-peak; FWHM: full-width at half max.

In this work, we sought to identify brain regions which had systematic differences in HRF shape between SZ, BP and matched healthy control groups in an effort to identify differential neurovascular coupling mechanisms in these disorders. Further, we estimated resting state functional connectivity in both the latent neural and raw BOLD spaces in an effort to identify possible confounds introduced by the variable HRF in identified functional networks.

4.2 Materials and Methods

4.2.1 Participants

The subject sample consisted of 38 patients satisfying DSM-IV criteria for SZ, 19 patients having BP with psychosis, and 35 matched healthy controls. Patients were recruited from the community-based mental health teams in Nottinghamshire and Leicestershire, United Kingdom. The diagnosis was made in a clinical consensus meeting in accordance with the procedure of Leckman et al [187]. Subjects aged under 18 or above 50, with neurological disorders, current substance dependence, or under-intelligence (Intelligence Quotient score <70 using Quick Test) subjects were excluded. All patients were in a stable phase of illness, defined as a change of no more than 10 points in their Global Assessment of Function [DSM-IV] score and no change in stability of antipsychotic, antidepressant, or mood medications in 6 weeks prior to the study.

Thirty-four healthy subjects, who are free of any psychiatric or neurological disorder and under-intelligence, were recruited from the local community via advertisements. The study was given ethical approval by the National Research Ethics Committee, Derbyshire, United Kingdom. All volunteers were given the written informed consent before scans.

4.2.2 Data Acquisition

Subject were scanned on a 3-T Philips Achieva MRI scanner (Philips, the Netherlands), using an 8-channel SENSE head coil with SENSE factor 2 in anterior-posterior direction. To enhance sensitivity, dual-echo gradient-echo echo-planar images (GE-EPI) were acquired [188] with sequence parameter setting as: TE1/TE2 25/53 ms, flip angle 85 degrees, 255 mm × 255 mm field

of view, with an in-plane resolution of 3 mm × 3 mm and a slice thickness of 4 mm, and TR of 2500 ms. At each dynamic time point, a volume data set was acquired consisting of 40 contiguous axial slices acquired in descending order, a total of 410 dynamic time points during an entire session, with 2 sessions per subject. An anatomical image was also acquired for each participant.

4.2.3 Pre-processing

The data was preprocessed by using Statistical Parametric Mapping (SPM8) [100]and Data Processing Assistant for resting-state fMRI [101]. After an initial correction for slice-timing differences, spatial realignment to the first image was carried out. Participants were excluded if movement parameters exceeded 3 mm. An interpolation method, Art Repair [189], was used to correct movement artifacts. A single weighted summation of the dual-echo dynamic time course was obtained for each subject [190], followed by retrospective physiological correction using RETROICOR [191]. Unified segmentation based on spatial normalization, and smoothing using a Gaussian kernel of 8 mm FWHM were carried out. Following this, linear detrending was performed to eliminate low frequency fluctuations and high frequency noise. Finally, variance accounted for by six head motion parameters and the global mean signal, were removed by regression. In order to reduce respiratory and cardiac effects, the white-matter signal and CSF (cerebro-spinal fluid) signal were also regressed. At this point, the pre-processing pipeline was split into two different pipelines. In the first pipeline, no further processing was done and the pre-processed data was designated as the non-deconvolved (NDC) dataset. In the second pipeline, an

additional deconvolution step using the method proposed by Wu et al. [75] was performed voxel-wise and the resulting data with voxel time series representing latent neural signals was designated as the deconvolved (DC) dataset. Finally, both DC and NDC dataset were temporally bandpass filtered in the (0.01 - 0.1 Hz) range.

4.2.4 Blind Deconvolution and HRF Estimation

We applied a blind deconvolution technique developed for resting state fMRI by Wu et. al. [75] to retrieve latent neural signals as well as estimate voxel-specific HRFs. This method is based on modeling peaks in the resting-state BOLD signal as a response to spontaneous neuronal events [103][192]. The HRF which best models the observed BOLD signal as its convolution with the underlying pseudo-random neural events is searched over a range of biologically plausible delays. Then, the voxel-specific HRFs and the latent neural signals were estimated from the raw BOLD signal using Weiner deconvolution [20]. The shape of the voxel-specific HRF was characterized using three easily interpretable parameters: response height (RH), time to peak (TTP), and full width half max (FWHM) (Figure 4.2).

4.2.5 Seed Region Selection

In order to investigate the effect of HRF variability on functional connectivity, we set out to estimate seed-based functional connectivity using DC and NDC datasets. In order to do this, we wanted to identify seed regions whose HRF shape was different in all the three groups. For each of the three HRF parameters, two sample two-tailed t-tests were conducted in three comparisons separately: SZ vs control, BP vs control, and SZ vs BP. In each comparison, maps that indicate

voxels showing significant (FDR corrected p-value<0.05, cluster-size>50) differences in three HRF parameters were obtained. This resulted in 6 maps (SZ<control, SZ>control, BP<control, BP>control, SZ<BP, and SZ>BP) per parameter and 18 maps overall. The regions identified in the intersection of all the 18 maps had altered HRF parameters in every comparison. We found only the thalamus in this intersection and hence was defined as the seed region of interest (seed ROI).

4.2.6 Seed-based Functional Connectivity

For each participant, the mean time series within the thalamus seed ROI was obtained. The functional connectivity between the thalamus seed and the remaining voxels in the brain were evaluated using Pearson's correlation coefficient between the mean time series of the seed ROI and the time series extracted from the rest of the voxels in the brain. The correlation coefficients were transformed by Fisher's z-transform to improve the normality [104][105]. The converted z-score maps are hereafter referred to as "the correlation maps". This pipeline was implemented separately for the two datasets: (i) NDC: data pre-processed without deconvolution, and (ii) DC: data pre-processed with deconvolution.

4.2.7 Group-level Analyses

For each group, the z-score maps from individual subjects were entered into a random effects one-sample t-test to determine voxels whose connectivity with the thalamus seed were significantly greater than zero. Subsequently, the correlation maps from individual subjects were also entered into a random effects two-sample t-test to identify brain regions showing significantly different connectivity with the thalamus seed ROI in three comparisons separately (SZ vs control,

BP vs control, and SZ vs BP). These procedures were also implemented separately for both DC and NDC datasets.

4.2.8 The Effect of Deconvolution

With the aim of investigating the effect of deconvolution on between-group differences in functional connectivity, we performed a two-way repeated-measures ANOVA using SPSS (version 20, IBM Inc., USA) software. In this analysis, the groups (SZ, BP, and Control) were considered as one factor and data with/without deconvolution as the other factor. We then identified the voxels showing a significant interaction between the two factors (FDR corrected p-value<0.05, cluster size>40 voxels).

4.3 Result

4.3.1 Between-group HRF Differences

In the SZ vs control comparison, we found that the bilateral thalamus, midbrain and precuneus had significantly (FDR corrected p-value<0.05) wider FWHM (Figure 4.3A) in the SZ group while the bilateral cereblum posterior lobe, left middle frontal gyrus and bilateral precentral gyrus had significantly (FDR corrected p-value<0.05) wider FWHM (Figure 4.3A) in the control group. The right anterior cingulate cortex and the right parahippocampal gyrus had significantly (FDR corrected p-value<0.05) higher RH (Figure 4.3A) in the SZ group while the bilateral cerebellum posterior lobe, posterior cingulate, precuneus and lingual gyrus had significantly (FDR corrected p-value<0.05) higher RH (Figure 4.3A) in the control group. The bilateral midbrain had

significantly (FDR corrected p-value<0.05) longer TTP (Figure 4.3A) in the SZ group while the bilateral cerebellum posterior lobe had significantly (FDR corrected p-value<0.05) longer TTP (Figure 4.3A) in the control group.

In the BP vs control comparison, we found that the bilateral anterior cingulate cortex and precuneus had significantly (FDR corrected p-value<0.05) wider FWHM (Figure 4.3B) in the BP group while the bilateral cerebellum posterior lobe, left middle temporal gyrus and bilateral precentral gyrus had significantly (FDR corrected p-value<0.05) wider FWHM (Figure 4.3B) in the control group. The bilateral anterior cingulate cortex, bilateral cingulate gyrus, bilateral medial frontal gyrus, and right supramarginal gyrus had significantly (FDR corrected p-value<0.05) higher RH (Figure 4.3B) in the BP group while the bilateral cerebellum posterior lobe, bilateral cerebellum anterior lobe, bilateral thalamus and bilateral medial frontal gyrus had significantly (FDR corrected p-value<0.05) higher RH (Figure 4.3B) in the control group. The bilateral cingulate gyrus had significantly (FDR corrected p-value<0.05) longer TTP (Figure 4.3B) in the BP group while the bilateral cerebellum posterior lobe, left middle temporal gyrus, and bilateral middle frontal gyrus had significantly (FDR corrected p-value<0.05) longer TTP (Figure 4.3A) in control group.

In the BP vs SZ comparison, we found that the bilateral cerebellum posterior lobe had significantly (FDR corrected p-value<0.05) wider FWHM (Figure 4.3C) in the BP group while the bilateral thalamus, cerebellum anterior lobe and midbrain had significantly (FDR corrected p-value<0.05) wider FWHM (Figure 4.3C) in the SZ group. The bilateral medial frontal gyrus, left

lingual gyrus, bilateral posterior cingulate and bilateral inferior parietal lobule had significantly (FDR corrected p-value<0.05) higher RH (Figure 4.3C) in the BP group while the bilateral parahippocampal gyrus and bilateral superior frontal gyrus had significantly (FDR corrected p-value<0.05) higher RH (Figure 4.3C) in the SZ group. The bilateral cerebellum posterior lobe had significantly (FDR corrected p-value<0.05) longer TTP (Figure 4.3C) in the BP group while the bilateral pons and thalamus had significantly (FDR corrected p-value<0.05) shorter TTP (Figure 4.3C) in the BP group. Detailed information such as cluster sizes, cluster centroids etc. are shown in Table 1.

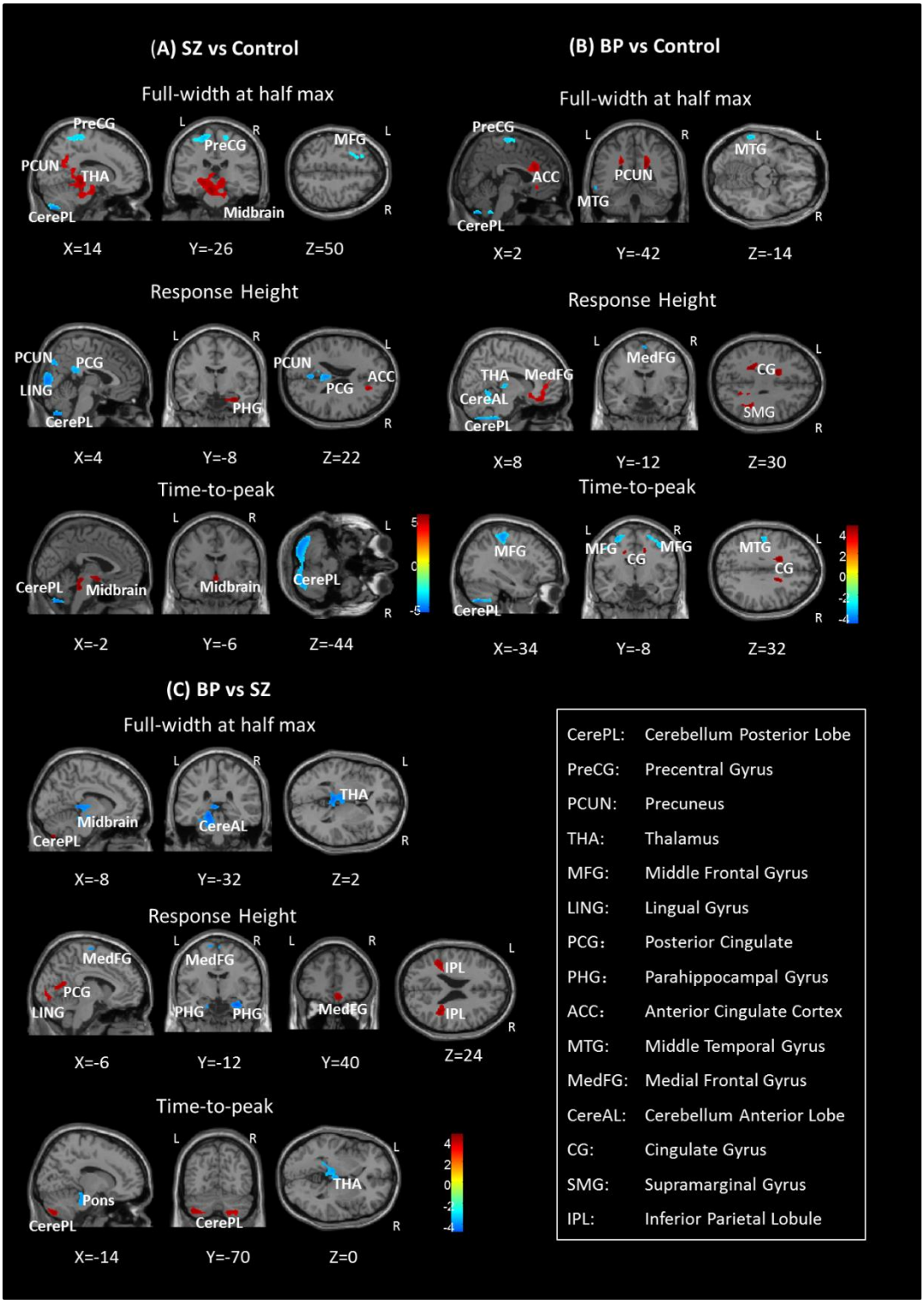

Figure 4.3 *Spatial maps showing regions with significantly different HRF parameters in the three comparisons: (A) SZ vs Control, (B) BP vs Control, and (C)BP vs SZ.*

Table 4.1. *Voxel clusters which had significantly different (FDR corrected p-value<0.05, cluster size>50 voxels) HRF parameters in three comparisons: BP vs Control, SZ vs Control, and BP vs SZ. The anatomical labels, MNI co-ordinates of cluster centroids, cluster size in terms of the number of voxels, T score, and corresponding Brodmann areas (where appropriate) are listed.*

Comparison	Cluster anatomical location	Coordinates			Cluster size	Hemisphere	BA	T score
		x	y	z				
Full-width at half max SZ>Control	Thalamus	-20	-16	0	4678	Bilateral		4.19
	Midbrain	0	-32	-14				3.91
	Precuneus	14	-56	32			31	3.52
Full-width at half max SZ<Control	Cerebellum Posterior Lobe	-62	-40	-12	4352	Bilateral	21	-4.47
	Middle Frontal Gyrus	-36	44	26	208	Left	10	-4.84
	Precentral Gyrus	18	-28	68	320	Right	4	-3.91
	Precentral Gyrus	-20	-28	66	715	Left	4	-4.48
Response height SZ>Control	Anterior Cingulate Cortex	18	36	18	104	Right	32	4.15
	Parahippocampal Gyrus	20	-4	-28	326	Right	28	4.71
Response height SZ<Control	Cerebellum Posterior Lobe	-30	-64	-50	2378	Bilateral		-3.96
	Posterior Cingulate	18	-60	4	527	Bilateral	30	-4.44
	Precuneus	-6	-52	30	1236	Bilateral	31	-3.85
	Lingual Gyrus	-4	-76	0			18	-3.55
Time-to-peak SZ>Control	Midbrain	2	-30	-14	540	Bilateral		3.70
Time-to-peak SZ<Control	Cerebellum Posterior Lobe	-26	-74	-50	1850	Bilateral		-5.08
Full-width at half max BP>Control	Anterior Cingulate Cortex	4	30	-8	1752	Bilateral	32	3.91
	Precuneus	-18	-46	30	329	Left	31	4.12
	Precuneus	14	-54	32	999	Right	31	4.57
Full-width at half max BP<Control	Cerebellum Posterior Lobe	-40	-54	-50	1229	Bilateral		-3.28
	Middle Temporal Gyrus	-62	-40	-12	86	Left	21	-3.58
	Precentral Gyrus	-18	-32	70	4352	Right	4	-4.69
	Precentral Gyrus	14	-38	72		Left	3	-3.93
Response height BP>Control	Cingulate Gyrus	-16	4	30	167	Left		3.66
	Cingulate Gyrus	-16	-26	40	228	Left	31	3.92
	Cingulate Gyrus	16	-58	28	96	Right	31	4.27
	Medial Frontal Gyrus	4	-10	66	624	Bilateral	6	4.01
	Supramarginal Gyrus	42	-48	34	438	Right	40	3.92

Response height BP<Control	Cerebellum Posterior Lobe	2	-58	-48	524	Bilateral		-4.03
	Cerebellum Anterior Lobe	20	-42	-26				-3.59
	Cerebellum Anterior Lobe	-20	-40	-26				-3.39
	Thalamus	4	-20	4	80	Bilateral		-4.65
	Medial Frontal Gyrus	-2	-10	66	481	Bilateral	6	-3.22
Time-to-peak BP>Control	Cingulate Gyrus	-10	12	34	262	Left	24	3.72
	Cingulate Gyrus	10	-6	38	150	Right	24	4.29
Time-to-peak BP<Control	Cerebellum Posterior Lobe	-10	-66	-50	909	Bilateral		-3.29
	Middle Temporal Gyrus	-36	2	-50	59	Left	20	-3.25
	Middle Frontal Gyrus	-26	-6	60	1157	Left	6	-4.12
	Middle Frontal Gyrus	32	-8	60	231	Right	6	-3.88
Full-width at half max BP>SZ	Cerebellum Posterior Lobe	-22	-80	-44	267	Left		4.36
	Cerebellum Posterior Lobe	16	-74	-50	81	Right		4.02
Full-width at half max BP<SZ	Thalamus	-6	-24	0	1126	Bilateral		-4.63
	Cerebellum Anterior Lobe	-16	-32	-18				-3.91
	Midbrain	-6	-32	-20				-3.52
Response height BP>SZ	Medial Frontal Gyrus	10	36	-20	196	Bilateral	11	4.26
	Lingual Gyrus	-12	-90	-2	477	Left	17	4.21
	Posterior Cingulate	-4	-60	18			23	3.84
	Posterior Cingulate	18	-66	8	280	Right	30	3.76
	Inferior Parietal Lobule	40	-40	26	358	Right		4.13
	Inferior Parietal Lobule	-42	-40	24	527	Left		4.24
Response height BP<SZ	Parahippocampal Gyrus	34	-6	-26	231	Right		-3.81
	Parahippocampal Gyrus	-16	-14	-26	103	Left	28	-4.06
	Medial Frontal Gyrus	-8	-12	68	218	Bilateral	6	-4.26
Time-to-peak BP>SZ	Cerebellum Posterior Lobe	-32	-78	-42	1193	Bilateral		3.56
Time-to-peak BP<SZ	Pons	-16	-26	-30	997			-3.96
	Thalamus	-8	-24	0				-3.71
Intersection	Thalamus	2	-22	4	101	Bilateral		

* Coordinates indicate location of maximum *Z*-scores for clusters or location of local maxima. For clusters with more than one peak, local maxima are listed. Cluster size in voxels. Coordinates are in standard MNI space.

* BA = Brodmann Area

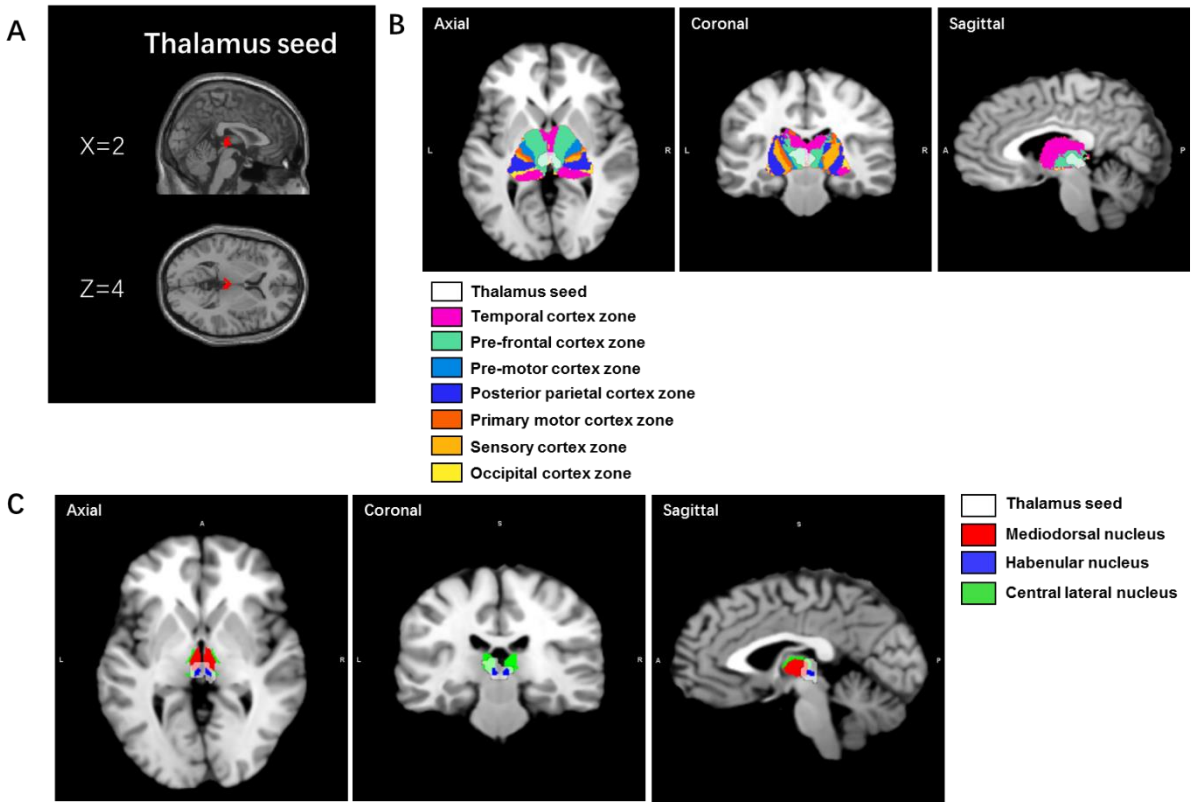

Figure 4.4. *(A) The voxels within the thalamus that showed alterations in all three HRF parameters in the following three comparisons: BP vs Control, SZ vs Control, and BP vs SZ. Sagittal (x = 2), and axial (z = 4) views are shown in standard MNI space. In the thalamus seed ROI, alterations in HRF parameters exhibited the following pattern: FWHM: SZ> Control; RH: BP< Control, and FWHM: SZ>BP. (B) The overlap of our thalamic seed (shown in white) with thalamic zones as described in the Oxford thalamic atlas* [193]. *Accordingly, diffusion tractography from the seed showed highest probability of structural connectivity with the temporal and pre-frontal lobes. (C) The overlap of our thalamic seed (shown in white) with thalamic nuclei described in the Morel thalamic atlas* [194][195]. *The seed encompasses the mediodorsal nucleus, habenular nucleus and the central lateral nucleus.*

We found that a thalamic cluster showed significant alterations in all three HRF parameters (Figure 4.4A). Note that in the identified thalamus seed ROI, the alterations in HRF parameters exhibited the following pattern: FWHM: SZ> Control, RH: BP< Control, and FWHM: SZ>BP. The overlap of our thalamic seed (shown in white, Figure 4.4B) with thalamic zones as described in the Oxford thalamic atlas [196] indicated that diffusion tractography from our seed showed

highest probability of structural connectivity with the temporal and pre-frontal lobes. By registering our seed ROI on the digital 3D Morel atlas [194][197], we found that the thalamic seed ROI encompasses the mediodorsal (MD) nucleus, habenular (Hb) nucleus and the central lateral (CL) nucleus (Figure 4.4C).

4.3.2 Thalamus-based Functional Connectivity within Groups

In the control group, the thalamus exhibited only positive functional connectivity with other brain regions. For the DC dataset, clusters significantly connected ($p<0.05$ FDR corrected, cluster size>50) to the thalamus seed included the bilateral cranial portions of the caudate, the bilateral caudal portion of the lingual gyrus, bilateral cerebellum posterior lobe, bilateral cerebellum anterior lobe, pons, bilateral posterior cingulate, bilateral anterior cingulate cortex, bilateral superior frontal gyrus and bilateral parietal lobe in DC dataset (Figure 4.5A, Table 4.2). In the NDC dataset, clusters significantly connected ($p<0.05$ FDR corrected, cluster size>50) to the thalamus seed included the bilateral cranial portions of the caudate, the bilateral caudal portion of the lingual gyrus, bilateral cerebellum posterior lobe, bilateral cerebellum anterior lobe, bilateral posterior cingulate, bilateral anterior cingulate cortex, bilateral cingulate gyrus, pons, bilateral superior frontal gyrus, and bilateral parietal lobe (Figure 4.5B, Table 4.2).

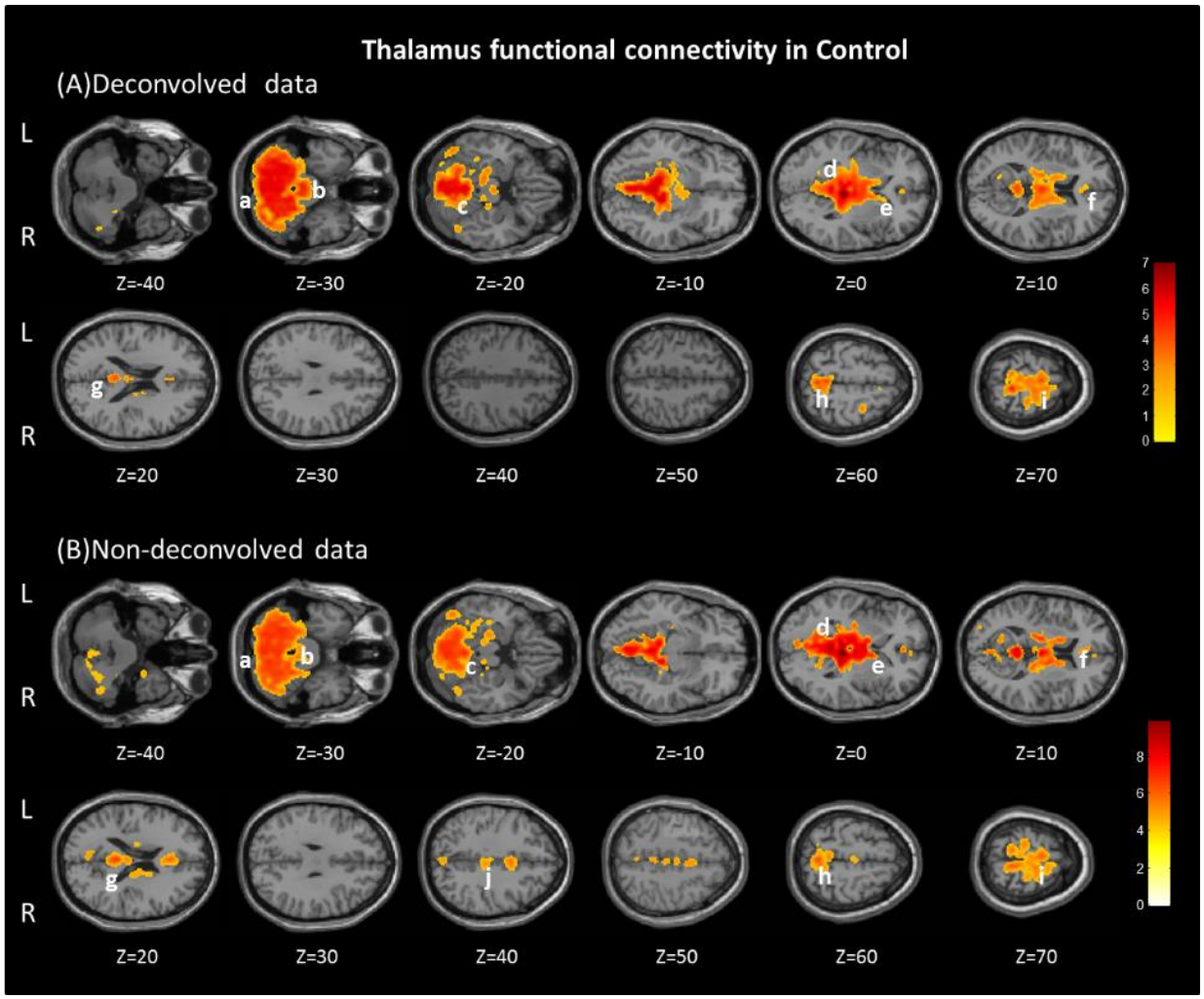

Figure 4.5. *Seed based functional connectivity of the thalamic ROI in Controls. Only positive correlations were significant. Axial views (z = -40 to 70) are presented (standard MNI space; cluster significance: p < 0.05, FDR corrected). (a) Cerebellum Posterior Lobe, (b) Pons, (c) Cerebellum Anterior Lobe, (d) Lingual Gyrus, (e) Caudate, (f)Anterior Cingulate Cortex, (g) Posterior Cingulate Cortex, (h) Parietal Lobe, (i) Superior Frontal Gyrus, (j)Cingulate Gyrus*

Table 4.2. *Thalamic seed-based functional connectivity in Controls. List of brain regions showing a significantly positive relationship with the thalamus (p<0.05 FDR corrected, cluster size>50), for both deconvolved and non-deconvolved datasets.*

Structure	BA	Coordinates			Z Score	Hemisphere
		x	y	z		
Deconvolved data						
Cluster 1, Cluster size 23577						
Cerebellum Posterior Lobe		48	-62	-34	5.44	Right

Cerebellum Posterior Lobe		-32	-66	-30	6.69	Left
Cerebellum Anterior Lobe		-2	-42	-6	4.22	Bilateral
Pons		-1	-32	-32	3.08	Bilateral
Posterior Cingulate	23	-2	-40	22	2.44	Bilateral
Lingual Gyrus	18	18	-56	2	2.23	Right
Lingual Gyrus	18	-10	-62	2	2.70	Left
Caudate		8	6	0	3.37	Right
Caudate		-8	4	0	2.95	Left
Cluster 2, Cluster size 731						
Anterior Cingulate Cortex		2	32	12	2.72	Bilateral
Cluster 3, Cluster size 324						
Superior Frontal Gyrus	32	-2	-8	70	2.21	Bilateral
Cluster 4, Cluster size 211						
Parietal Lobe	4	6	-44	68	4.02	Bilateral
Non-deconvolved data						
Cluster 1, Cluster size 24433						
Cerebellum Posterior Lobe		48	-62	-28	4.92	Right
Cerebellum Posterior Lobe		-20	-68	-30	5.12	Left
Cerebellum Anterior Lobe		-2	-42	-6	6.79	Bilateral
Pons		4	-32	-32	3.95	Bilateral
Posterior Cingulate	29	4	-50	10	4.10	Bilateral
Lingual Gyrus	30	14	-56	4	3.39	Right
Lingual Gyrus	18	-10	-62	2	4.02	Left
Caudate		10	2	2	4.27	Right
Caudate		-14	8	10	5.73	Left
Cluster 2, Cluster size 3411						
Parietal Lobe	4	8	-44	68	4.80	Bilateral
Superior Frontal Gyrus	6	-4	-6	70	3.38	Bilateral
Cluster 3, Cluster size 1379						
Anterior Cingulate Cortex	24	2	32	16	3.92	Bilateral
Cluster 4, Cluster size 412						
Cingulate Gyrus		2	2	38	3.24	Bilateral

* Z-value is the mean across the group.

* Coordinates indicate location of maximum Z-scores for clusters or location of local maxima. For clusters with more than one peak, local maxima are listed. Cluster size in voxels.

* Coordinates are in standard MNI space.

* BA = Brodmann Area.

In the SZ group, the brain regions significantly ($p<0.05$ FDR corrected, cluster size>50)

correlated with the thalamus seed in the NDC dataset included the caudal portion of the lingual gyrus, bilateral cerebellum posterior lobe, bilateral cerebellum anterior lobe, pons, bilateral posterior cingulate, bilateral cingulate gyrus, bilateral superior temporal gyrus, bilateral superior frontal gyrus and bilateral parietal lobe in DC dataset (Figure 4.6A, Table 4.3). In the NDC dataset, brain regions significantly ($p<0.05$ FDR corrected, cluster size>50) correlated with the thalamus seed in included the caudal portion of the lingual gyrus, bilateral cerebellum posterior lobe, bilateral cerebellum anterior lobe, pons, bilateral posterior cingulate, bilateral cingulate gyrus, right superior temporal gyrus, right middle temporal gyrus; bilateral superior frontal gyrus, bilateral parietal lobe and right putamen (Figure 4.6B, Table 4.3).

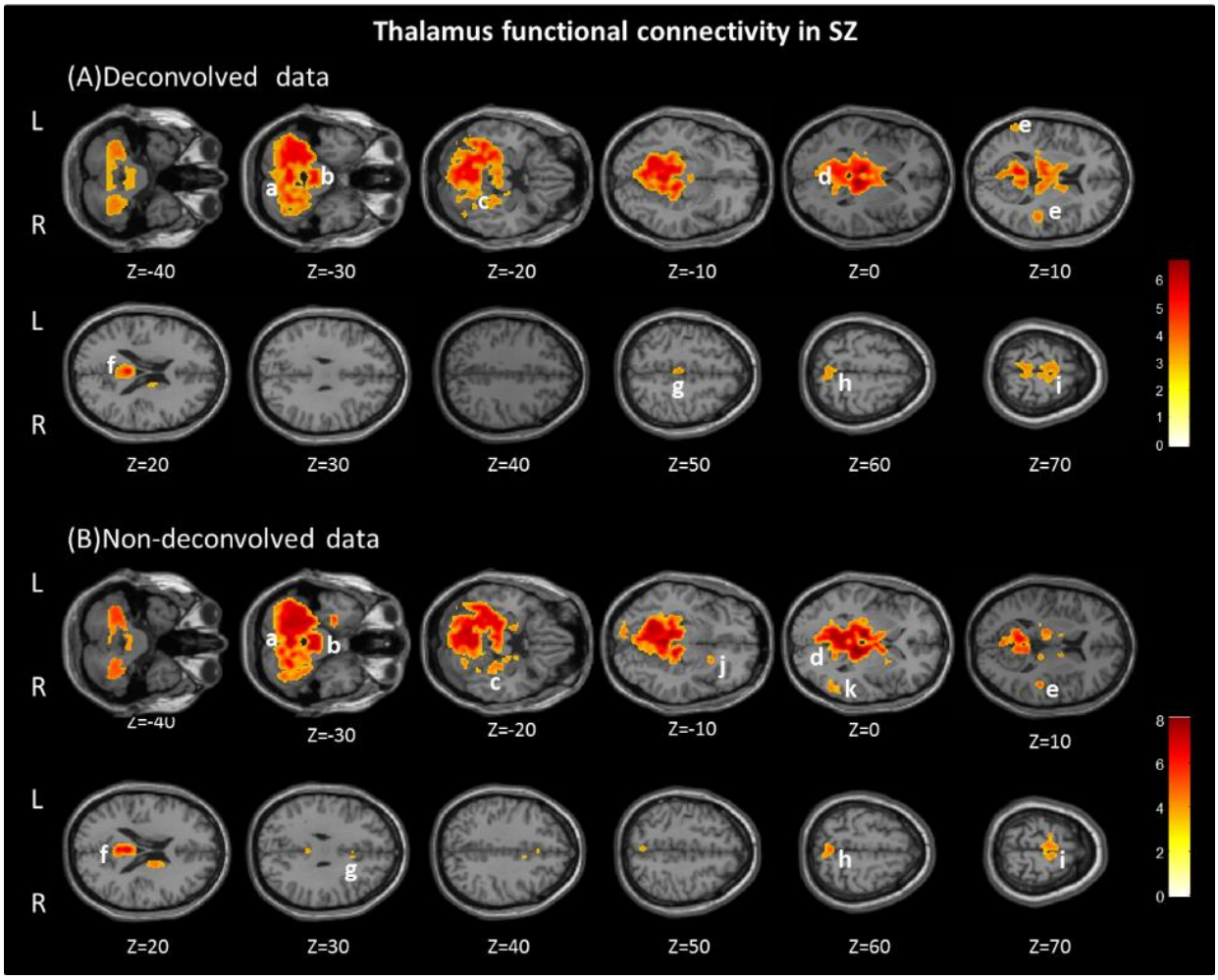

Figure 4.6. *Seed based functional connectivity of the thalamic ROI in Schizophrenia. Only positive correlations were significant. Axial views (z = -40 to 70) are presented (standard MNI space; cluster significance: p < 0.05, FDR corrected). (a) Cerebellum Posterior Lobe, (b) Pons, (c) Cerebellum Anterior Lobe, (d) Lingual Gyrus, (e) Superior Temporal Gyrus, (f) Posterior Cingulate, (g) Cingulate Gyrus, (h) Parietal Lobe, (i) Superior Frontal Gyrus, (j) Putamen, (k)Middle Temporal Gyrus*

Table 4.3. *Thalamic seed-based functional connectivity in Schizophrenia. List of brain regions showing a significantly positive connectivity with the thalamus (p<0.05 FDR corrected, cluster size>50), for both deconvolved and non-deconvolved datasets.*

Structure	BA	Coordinates			Z Score	Hemisphere
		x	y	z		
Deconvolved data						
Cluster 1, Cluster size 21557						
Cerebellum Posterior Lobe		-4	-72	-18	3.69	Bilateral
Cerebellum Anterior Lobe		0	-60	-28	3.65	Bilateral
Lingual Gyrus	18	18	-56	2	2.66	Right

Lingual Gyrus	18	-10	-62	2	3.64	Left
Pons		0	-32	-34	3.02	Bilateral
Posterior Cingulate	29	3	-52	18	3.44	Bilateral
Superior Frontal Gyrus	6	10	-8	70	3.06	Right
Superior Frontal Gyrus	6	-8	-8	70	3.00	Left
Cluster 2, Cluster size 630						
Parietal Lobe	7	4	-62	56	3.38	Bilateral
Cluster 3, Cluster size 153						
Cingulate Gyrus		4	-24	44	3.61	Bilateral
Cluster 4, Cluster size 224						
Superior Temporal Gyrus	22	-62	-54	14	3.16	Left
Cluster 5, Cluster size 346						
Superior Temporal Gyrus	41	48	-28	12	2.82	Right
Non-deconvolved data						
Cluster 1, Cluster size 21557						
Cerebellum Posterior Lobe		-2	-60	-6	6.05	Bilateral
Cerebellum Anterior Lobe		-2	-60	-26	5.56	Bilateral
Lingual Gyrus		18	-54	0	4.89	Right
Lingual Gyrus		-8	-92	-8	4.14	Left
Pons		2	-34	-34	4.22	Bilateral
Posterior Cingulate	29	2	-48	20	4.13	Bilateral
Cluster 2, Cluster size 332						
Superior Frontal Gyrus	6	-6	-10	70	5.03	Left
Superior Frontal Gyrus	6	8	-10	70	5.17	Right
Cluster 3, Cluster size 298						
Parietal Lobe	7	0	-60	58	4.43	Bilateral
Cluster 3, Cluster size 159						
Cingulate Gyrus	32	4	16	34	4.77	Bilateral
Cluster 4, Cluster size 160						
Middle Temporal Gyrus		56	-60	0	3.53	Right
Cluster 5, Cluster size 104						
Superior Temporal Gyrus	42	66	-52	12	3.55	Right
Cluster 6, Cluster size 138						
Putamen		22	14	-10	3.71	Right

* Z-value is the mean across the group.

* Coordinates indicate location of maximum Z-scores for clusters or location of local maxima. For clusters with more than one peak, local maxima are listed. Cluster size in voxels.

* Coordinates are in standard MNI space.

* BA = Brodmann Area.

In the BP group, the brain regions which were significantly ($p<0.05$ FDR corrected, cluster size>50) correlated with the thalamic seed included the caudal portion of the left lingual gyrus, bilateral cerebellum posterior lobe, bilateral cerebellum anterior lobe, pons, bilateral posterior cingulate, bilateral cingulate gyrus, and bilateral insula in the DC dataset (Figure 4.7A, Table 4.4). In the NDC dataset, the brain regions which were significantly ($p<0.05$ FDR corrected, cluster size>50) correlated with the thalamic seed included the caudal portion of the left lingual gyrus, bilateral cerebellum posterior lobe, bilateral cerebellum anterior lobe, bilateral cingulate gyrus, pons, bilateral posterior cingulate, bilateral parietal lobe, bilateral anterior cingulate cortex, bilateral insula, right superior temporal gyrus and right middle temporal gyrus (Figure 4.7B, Table 4.4).

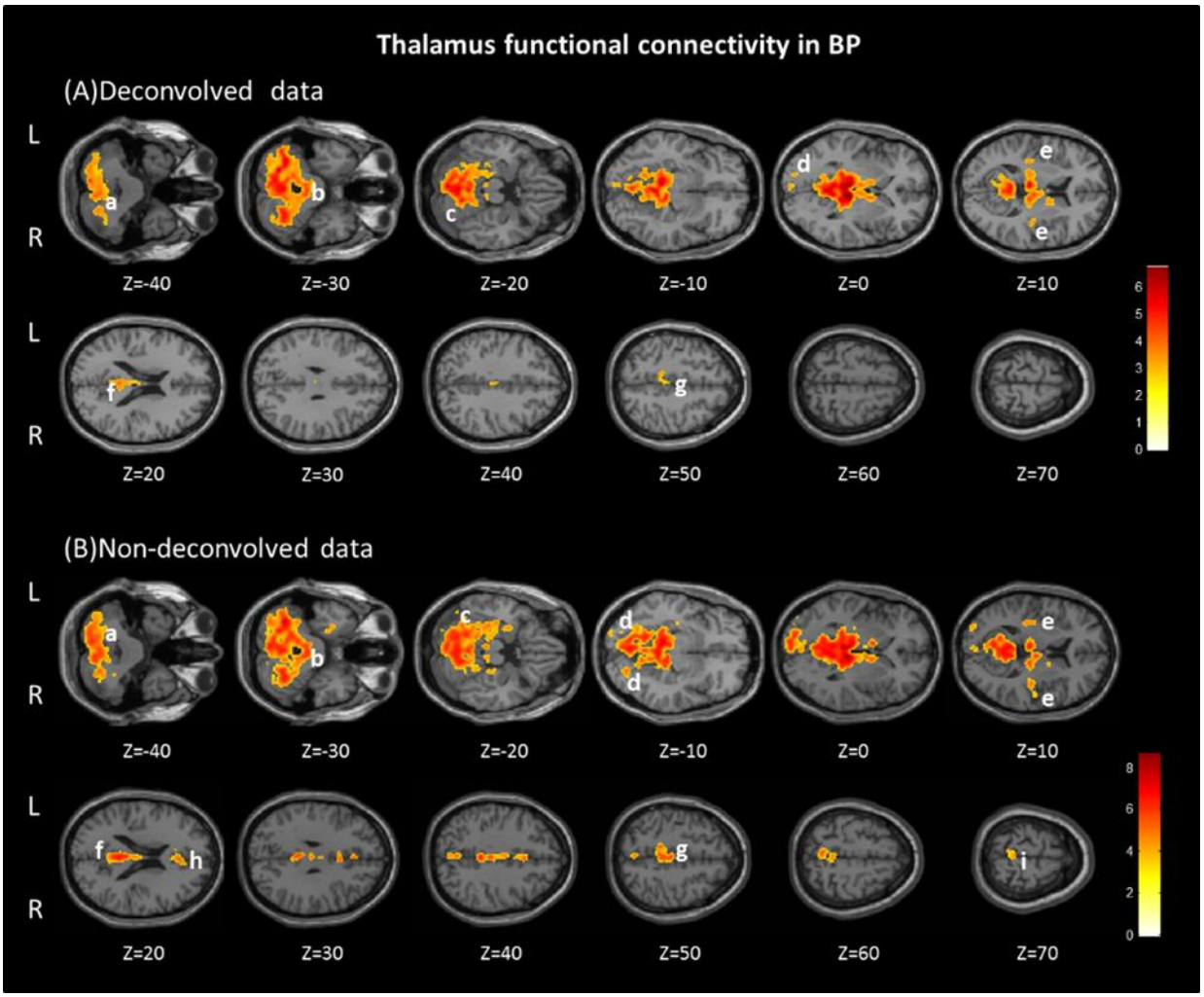

Figure 4.7 *Seed based functional connectivity of the thalamic ROI in Bipolar Disorder. Only positive correlations were significant. Axial views (z = -40 to 70) are presented (standard MNI space; cluster significance: p < 0.05, FDR corrected). (a) Cerebellum Posterior Lobe, (b) Pons, (c) Cerebellum Anterior Lobe, (d) Lingual Gyrus, (e) Insula, (f) Posterior Cingulate, (g) Cingulate Gyrus, (h) Anterior Cingulate Cortex, (i) Parietal Lobe*

Table 4.4. *Thalamic seed-based functional connectivity in Bipolar Disorder. List of brain regions showing a significantly positive connectivity with the Thalamus (p<0.05 FDR corrected, cluster size>50), for both deconvolved and non-deconvolved datasets.*

Structure	BA	Coordinates			Z Score	Hemisphere
		x	y	z		
Deconvolved data						
Cluster 1, Cluster size 14661						
Midbrain		-4	-12	4	6.71	Bilateral
Cerebellum Posterior Lobe		34	-60	-28	3.41	Right

Cerebellum Posterior Lobe		-34	-70	-36	3.44	Left
Cerebellum Anterior Lobe		2	-52	-2	4.08	Bilateral
Pons		0	-32	-28	3.32	Bilateral
Posterior Cingulate	30	2	-46	18	4.25	Bilateral
Cluster 2, Cluster size 93						
Insula	13	40	-20	8	3.06	Right
Cluster 3, Cluster size 56						
Insula	13	-34	-24	10	2.58	Left
Cluster4, Cluster size 73						
Lingual Gyrus		-18	-92	-4	3.28	Left
Cluster5, Cluster size 154						
Cingulate Gyrus		0	-24	34	2.86	Bilateral
Non-deconvolved data						
Cluster 1, Cluster size 20195						
Midbrain		-4	-12	4	8.61	Bilateral
Cerebellum Posterior Lobe		26	-62	-32	5.44	Right
Cerebellum Posterior Lobe		-20	-52	-24	6.68	Left
Cerebellum Anterior Lobe		2	-52	-2	5.83	Bilateral
Posterior Cingulate	30	2	-50	16	4.51	Bilateral
Pons		0	-32	-32	3.85	Bilateral
Cluster 2, Cluster size 182						
Insula	13	40	-20	10	4.86	Right
Cluster 3, Cluster size 115						
Insula	13	-34	-26	8	4.21	Left
Cluster 4, Cluster size 147						
Lingual Gyrus		24	-78	-8	3.89	Right
Cluster 5, Cluster size 292						
Lingual Gyrus		-18	-90	-4	3.52	left
Cluster 6, Cluster size 172						
Parietal Lobe	7	-2	-76	38	4.71	Bilateral
Cluster 7, Cluster size 331						
Anterior Cingulate cortex		0	28	24	4.34	Bilateral
Cluster 8, Cluster size 279						
Cingulate Gyrus		2	14	38	4.55	Bilateral

* Z-value is the mean across the group.

* Coordinates indicate location of maximum Z-scores for clusters or location of local maxima. For clusters with more than one peak, local maxima are listed. Cluster size in voxels.

* Coordinates are in standard MNI space.

* BA = Brodmann Area.

4.3.3 Thalamus-based Connectivity Differences between Groups

In the comparison of the SZ group with healthy controls, differences in thalamic functional connectivity pattern were ascertained using both DC and NDC datasets. In the DC dataset, functional connectivity between the thalamic seed and the following regions were stronger in the SZ group: bilateral cerebellum anterior lobe, pons, bilateral posterior cingulate, bilateral superior temporal gyrus and bilateral cingulate gyrus. In contrast functional connectivity between the thalamic seed and the following regions were weaker in the SZ group: bilateral cerebellum posterior lobe, bilateral anterior cingulate cortex and right caudate (Figure 4.8A, Table 4.5). In the NDC dataset, functional connectivity between the thalamic seed and the following regions were stronger in the SZ group: bilateral cerebellum anterior lobe, pons, bilateral posterior cingulate, pons, and right superior temporal gyrus. In contrast functional connectivity between the thalamic seed and the following regions were weaker in the SZ group: bilateral cerebellum posterior lobe and bilateral anterior cingulate cortex (Figure 4.8B, Table 4.5).

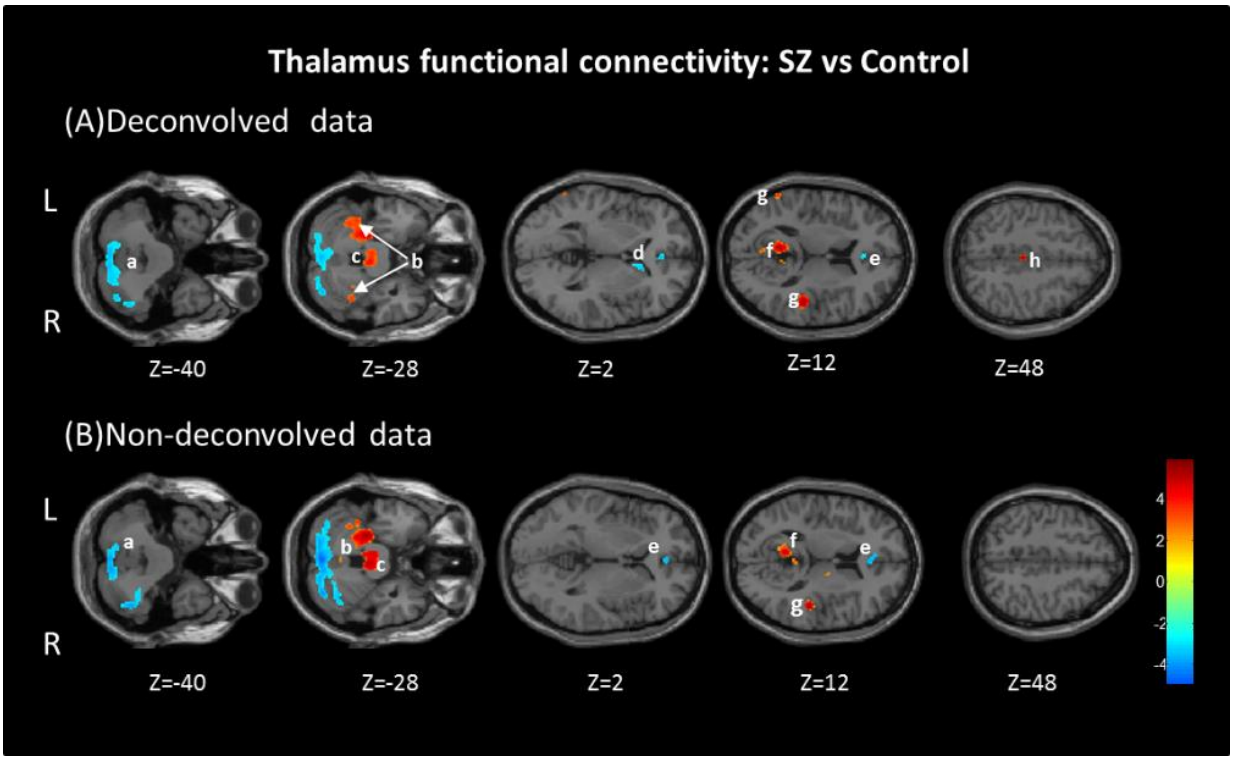

Figure 4.8 *Group differences in the functional connectivity of the thalamic seed for SZ vs Control comparison. Warm/cool colours indicate regions which had stronger/weaker functional connectivity with the thalamic seed in the SZ group, respectively. Axial views are presented (Z = -40, -28, -4, 2, 12 and 48), (standard MNI space; cluster significance: p < 0.05, FDR corrected). (a) Cerebellum Posterior Lobe, (b) Cerebellum Anterior Lobe, (c) Pons, (d) Caudate, (e)Anterior Cingulate Cortex, (f) Posterior Cingulate, (g) Superior Temporal Gyrus, (h) Cingulate Gyrus.*

Table 4.5. *Regions showing significant differences in functional connectivity of the thalamic seed for the SZ vs Control comparison (p<0.05 FDR corrected, cluster size>50), for both deconvolved and non-deconvolved datasets.*

Structure	BA	Coordinates			T Score	Z Score in SC group	Z Score in control group	Hemisphere
		x	y	z				
Deconvolved data								
SC>Control								
Cluster 1, Cluster size 4425								
Cerebellum Anterior Lobe		-22	-32	-24	5.00	3.23	2.04	Bilateral
Pons		4	-34	-34	4.12	2.96	2.87	Bilateral
Cluster 2, Cluster size 329								
Posterior Cingulate		10	-52	8	5.24	2.74	0.96	Right
Posterior Cingulate		-10	-54	10	4.92	3.48	1.61	Left
Cluster 3, Cluster size 94								

Cerebellum Anterior Lobe		34	-52	-22	4.06	2.55	1.03	Right
Cluster 4, Cluster size 233								
Superior Temporal Gyrus	41	48	-26	12	4.39	2.52	1.69	Right
Cluster 5, Cluster size 88								
Superior Temporal Gyrus	22	-62	-52	16	3.87	2.66	1.18	Left
Cluster 6, Cluster size 40								
Cingulate Gyrus		4	-24	44	3.92	3.41	1.52	Bilateral
SZ<Control								
Cluster 1, Cluster size 2433								
Cerebellum Posterior Lobe		12	-46	-50	-4.60	2.25	2.77	Bilateral
Cluster 2, Cluster size 30								
Caudate		12	20	2	-3.79	2.19	1.54	Right
Cluster3, Cluster size 56								
Anterior Cingulate Cortex		2	40	0	-3.76	2.34	1.08	Bilateral
Non-deconvolved data								
SZ>Control								
Cluster 1, Cluster size 3638								
Cerebellum Anterior Lobe		-24	-32	-24	2.89	5.24	2.45	Bilateral
Posterior Cingulate		-10	-58	6	2.72	3.70	3.19	Bilateral
Pons		6	-30	-26	2.66	3.43	3.03	Bilateral
Cluster 2, Cluster size 51								
Cerebellum Anterior Lobe		12	-44	-6	2.71	5.55	3.61	Bilateral
Cluster 3, Cluster size 59								
Superior Temporal Gyrus	41	48	-28	10	3.09	3.62	0.53	Right
SZ<Control								
Cluster 1, Cluster size 1747								
Cerebellum Posterior Lobe		-4	-80	-40	-2.88	2.35	3.61	Bilateral
Cluster 2, Cluster size 150								
Anterior Cingulate Cortex	32	2	42	-2	-2.52	1.61	3.42	Bilateral

* Z-value is the mean across the group.

* Coordinates indicate location of maximum Z-scores for clusters or location of local maxima. For clusters with more than one peak, local maxima are listed. Cluster size in voxels.

* Coordinates are in standard MNI space.

* BA = Brodmann Area.

In the comparison BP group with healthy controls, the thalamus seed ROI had stronger connectivity in the BP group with the following ROIs: bilateral cerebellum anterior lobe, bilateral

cerebellum posterior lobe, pons, bilateral posterior cingulate, left lingual gyrus and right insula, while the following regions has weaker connectivity in the BP group: bilateral anterior cingulate cortex, bilateral superior frontal gyrus and right caudate (Figure 4.9A, Table 4.6). In the NDC dataset, the following regions had stronger connectivity with the thalamic ROI in the BP group: bilateral cerebellum anterior lobe, pons, bilateral posterior cingulate, bilateral cerebellum posterior lobe, bilateral lingual gyrus, bilateral cingulate gyrus, and right insula, while the following regions had weaker connectivity with the thalamic ROI in the BP group: bilateral anterior cingulate cortex, bilateral superior frontal gyrus (Figure 4.9B, Table 4.6).

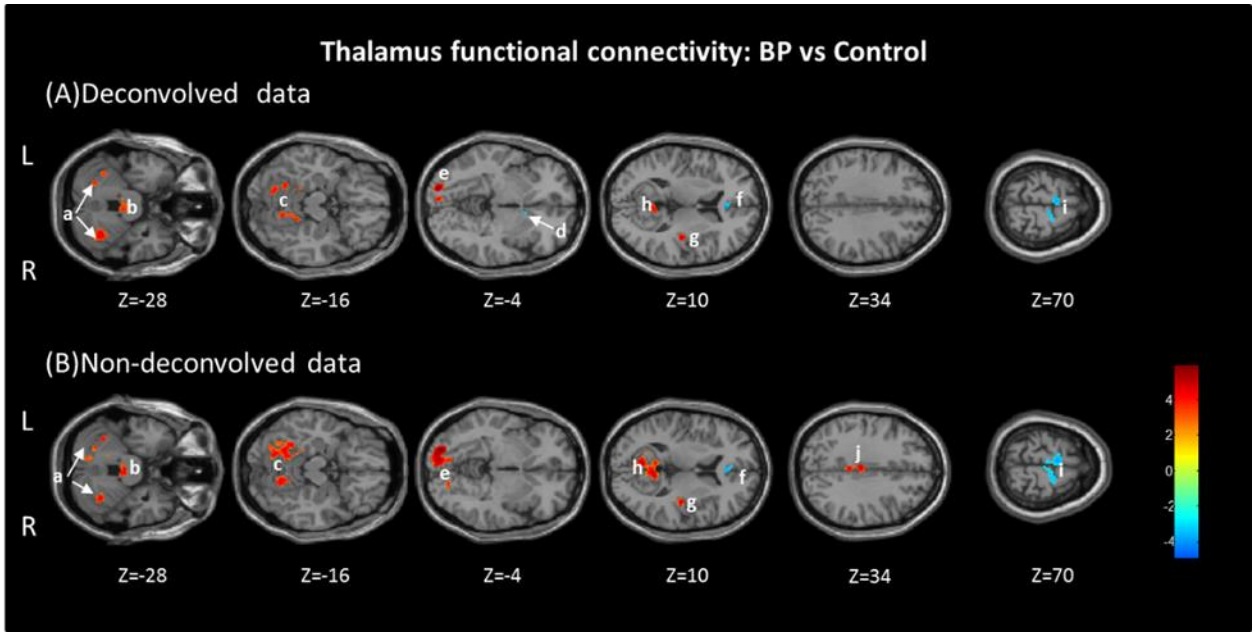

Figure 4.9 *Group differences in the functional connectivity of the thalamic seed for BP vs Control comparison. Warm/cool colours indicate regions which had stronger/weaker functional connectivity with the thalamic seed in the SZ group, respectively. Axial views are presented (Z = -28, -16, -4, 10, 34 and 70). (standard MNI space; cluster significance: p < 0.05, FDR corrected). (a) Cerebellum Posterior Lobe, (b) Pons, (c)Cerebellum Anterior Lobe, (d) Caudate, (e) Lingual Gyrus, (f) Anterior Cingulate, (g) Insula, (h)Posterior Cingulate, (i)Superior Frontal Gyrus, (j)Cingulate Gyrus*

Table 4.6. *Regions showing significant differences in functional connectivity of the thalamic seed for the BP vs Control comparison (p<0.05 FDR corrected, cluster size>50), for both deconvolved and non-deconvolved datasets.*

Structure	BA	Coordinates			T Score	Z Score in BP group	Z Score in control group	Hemisphere
		x	y	z				
Deconvolved data								
BP>Control								
Cluster 1, Cluster size 938								
Cerebellum Anterior Lobe		-16	-54	-12	3.91	2.77	2.20	Left
Cerebellum Anterior Lobe		10	-60	-12	3.33	3.08	2.62	Right
Posterior Cingulate	29	4	-52	12	2.61	3.14	2.84	Bilateral
Cluster 2, Cluster size 122								
Cerebellum Posterior Lobe		-18	-70	-18	3.92	2.76	2.21	Left
Cluster 3, Cluster size 63								
Cerebellum Posterior Lobe		40	-58	-30	3.23	2.73	1.72	Right
Cluster 4, Cluster size 33								
Pons		-6	-40	-36	2.64	3.18	2.27	Bilateral
Cluster 5, Cluster size 66								
Lingual Gyrus		-20	-90	-4	2.52	2.33	0.90	Left
Cluster 6, Cluster size 82								
Insula	13	40	-20	8	3.56	3.06	0.07	Right
BP<Control								
Cluster 1, Cluster size 64								
Anterior Cingulate Cortex		2	32	10	-3.47	0.17	2.71	Bilateral
Cluster 2, Cluster size 58								
Caudate		12	18	4	-3.35	1.40	2.05	Right
Cluster 3, Cluster size 149								
Superior Frontal Gyrus		-4	-10	70	-3.11	1.08	3.34	Bilateral
Non-deconvolved data								
BP>Control								
Cluster 1, Cluster size 538								
Lingual Gyrus		-20	-90	-4	4.46	4.01	1.41	Bilateral
Cerebellum Anterior Lobe		-20	-50	-22	4.21	4.73	3.10	Bilateral
Posterior Cingulate		-8	-52	8	2.67	4.56	2.48	Bilateral
Cluster 2, Cluster size 186								
Cerebellum Anterior Lobe		14	-64	-14	3.56	3.57	2.87	Bilateral
Cluster 3, Cluster size 47								
Cerebellum Posterior Lobe		34	-58	-28	3.16	5.16	3.20	Bilateral

Cluster 4, Cluster size 171								
Cingulate Gyrus	23	-2	-24	34	2.86	4.43	2.08	Bilateral
Cluster 5, Cluster size 76								
Lingual Gyrus		24	-80	-8	3.64	2.25	0.84	Right
Cluster 6, Cluster size 48								
Insula	13	40	-20	10	4.27	4.07	0.03	Right
Cluster 7, Cluster size 239								
Pons		2	-32	-30	3.25	4.61	3.58	Bilateral
BP<Control								
Cluster 1, Cluster size 50								
Anterior Cingulate Cortex	24	2	30	10	-4.41	1.88	3.16	Bilateral
Cluster 2, Cluster size 184								
Superior Frontal Gyrus		-4	-8	70	-3.36	1.23	3.52	Bilateral

* Z-value is the mean across the group.
* Coordinates indicate location of maximum Z-scores for clusters or location of local maxima. For clusters with more than one peak, local maxima are listed. Cluster size in voxels.
* Coordinates are in standard MNI space.
* BA = Brodmann Area.

In the comparison of BP with SZ patients using the DC dataset, the thalamic seed ROI had stronger connectivity in the BP group with the bilateral cerebellum posterior lobe and right insula, while it had weaker connectivity with bilateral cerebellum anterior lobe, bilateral posterior cingulate, bilateral superior temporal gyrus, bilateral superior frontal gyrus and bilateral cingulate gyrus (Figure 4.10A, Table 4.7). In the NDC dataset, the thalamic seed ROI had stronger connectivity in the BP group with bilateral cerebellum posterior lobe, left lingual gyrus, bilateral cingulate gyrus, and anterior cingulate cortex, and weaker connections with bilateral cerebellum anterior lobe, right superior temporal gyrus and bilateral superior frontal gyrus (Figure 4.10B, Table 4.7). All between-group differences found with both DC and NDC datasets are summarized in Figure 4.11.

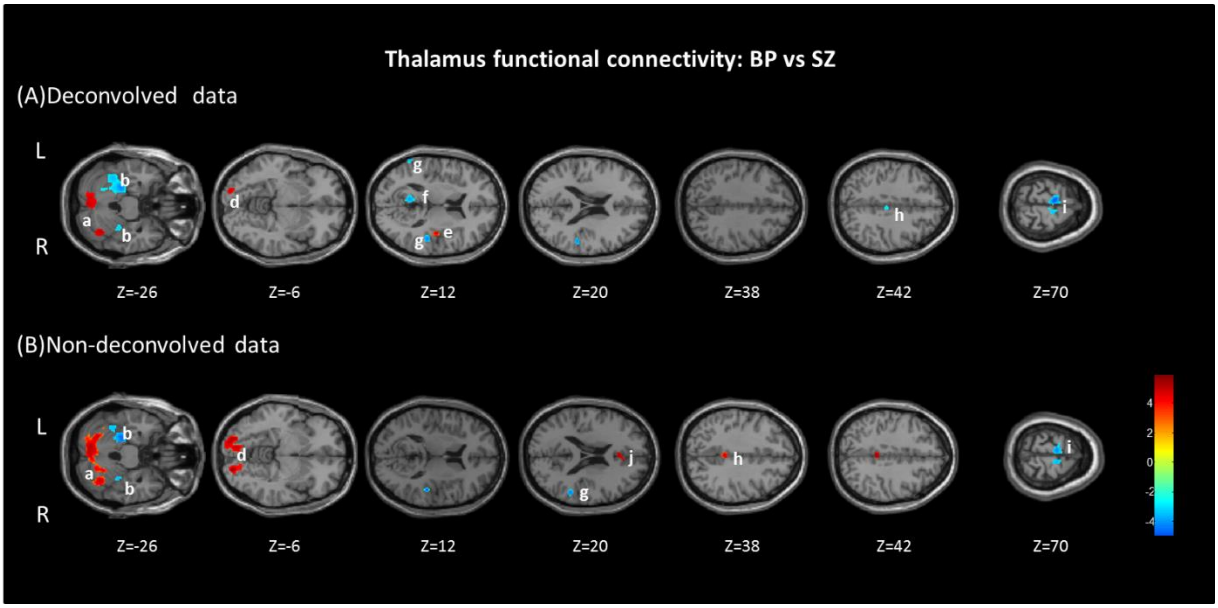

Figure 4.10 *Group differences in the functional connectivity of the thalamic seed for BP vs SZ comparison. Warm/cool colours indicate regions which had stronger/weaker functional connectivity with the thalamic seed in the SZ group, respectively. Axial views are presented (Z = -26, -6, 12, 20, 38, 42 and 70). (standard MNI space; cluster significance: p < 0.05, FDR corrected). (a) Cerebellum Posterior Lobe, (b) Cerebellum Anterior Lobe, (c) Pons, (d) Lingual Gyrus, (e) Insula, (f) Posterior Cingulate, (g) Superior Temporal Gyrus, (h) Cingulate Gyrus, (i) Superior Frontal Gyrus, (j) Anterior Cingulate Cortex.*

Table 4.7. *Regions showing significant differences in functional connectivity of the thalamic seed for the BP vs SZ comparison (p<0.05 FDR corrected, cluster size>50), for both deconvolved and non-deconvolved datasets.*

Structure	BA	Coordinates			T Score	Z Score in BP group	Z Score in SC group	Hemisphere
		x	y	z				
Deconvolved data								
BP>SZ								
Cluster 1, Cluster size 284								
Cerebellum Posterior Lobe		-12	-80	-38	3.04	2.89	2.47	Left
Cluster 2, Cluster size 60								
Cerebellum Posterior Lobe		38	-60	-28	2.92	2.92	0.61	Right
Cluster 3, Cluster size 70								
Insula		40	-18	0	2.93	2.95	0.94	Right
BP<SZ								
Cluster 1, Cluster size 1735								
Cerebellum Anterior Lobe		6	-64	-6	-4.03	1.31	3.28	Bilateral
Posterior Cingulate		-8	-54	10	-3.55	1.93	3.33	Bilateral
Cluster 2, Cluster size 111								

Superior Temporal Gyrus		50	-30	14	-3.51	0.57	2.61	Right
Cluster 3, Cluster size 75								
Superior Temporal Gyrus		-62	-50	16	-3.38	0.53	2.73	Left
Cluster 4, Cluster size 99								
Superior Frontal Gyrus	6	-6	-10	72	-4.89	0.95	2.34	Left
Cluster 5, Cluster size 66								
Superior Frontal Gyrus	6	12	-10	74	-3.78	1.34	2.70	Right
Cluster 6, Cluster size 101								
Cingulate Gyrus		4	-24	44	-3.14	1.05	3.41	Bilateral
Non-deconvolved data								
BP>SZ								
Cluster 1, Cluster size 2233								
Cerebellum Posterior Lobe		-16	-80	-36	3.11	5.04	3.67	Bilateral
Cluster 2, Cluster size 54								
Cingulate Gyrus	31	2	-38	38	2.46	4.91	2.52	Bilateral
Cluster 3, Cluster size 248								
Lingual Gyrus		-20	-92	-2	2.94	3.56	1.29	Left
Cluster 4, Cluster size 43								
Anterior Cingulate Cortex		4	46	-2	2.85	2.24	0.71	Bilateral
BP<SZ								
Cluster 1, Cluster size 1702								
Cerebellum Anterior Lobe		-24	-32	-26	-2.68	2.54	4.92	Left
Cluster 1, Cluster size 71								
Superior Temporal Gyrus		54	-42	18	-3.37	0.14	3.00	Right
Cluster 1, Cluster size 154								
Superior Frontal Gyrus	6	-4	-10	72	-5.04	1.34	4.34	Left
Cluster 1, Cluster size 2233								
Superior Frontal Gyrus	6	10	-14	74	-3.32	0.97	3.12	Right

* Z-value is the mean across the group.

* Coordinates indicate location of maximum *Z*-scores for clusters or location of local maxima. For clusters with more than one peak, local maxima are listed. Cluster size in voxels.

* Coordinates are in standard MNI space.

* BA = Brodmann Area.

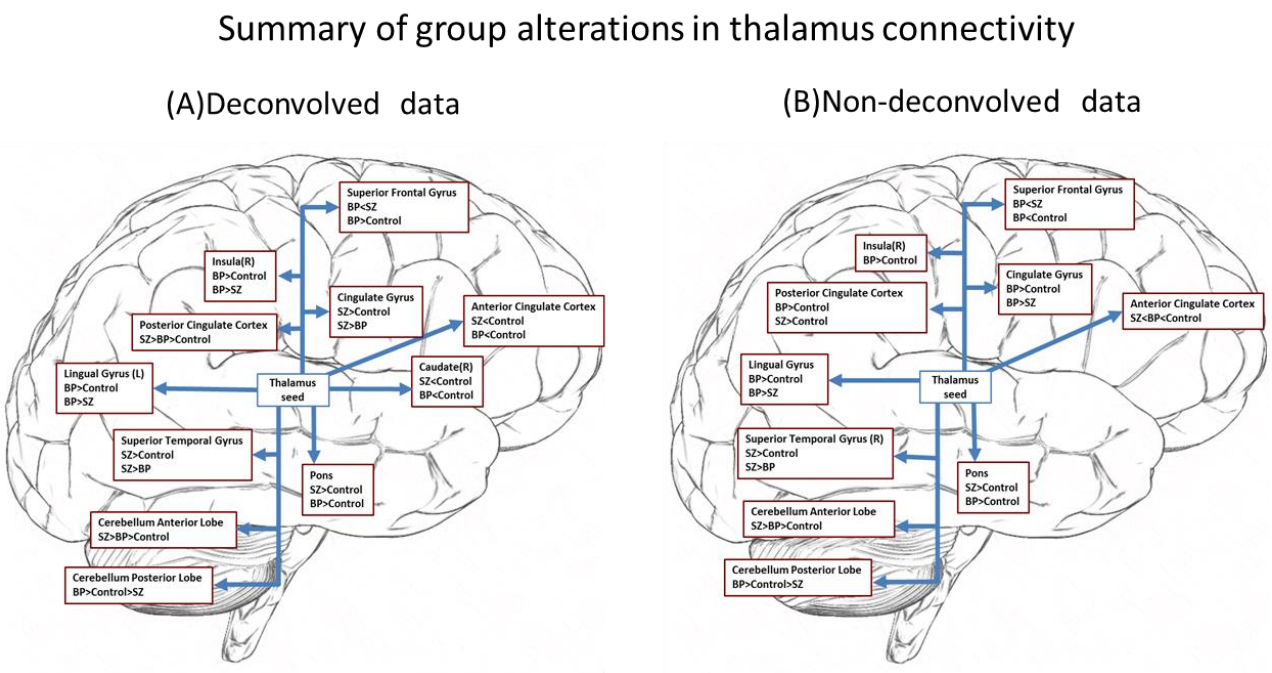

Figure 4.11 *Summary of between-group differences in thalamus seed-based functional connectivity for deconvolved (A) and non-deconvolved (B) datasets.*

4.3.4 The Effect of Deconvolution

Voxel clusters in bilateral lingual gyrus, bilateral insula and bilateral superior frontal gyrus showed a significant ($p<0.05$ FDR corrected, cluster size>40) interaction effect between the group factor (Control vs BP vs SZ) and the deconvolution factor (data with and without deconvolution) (Figure 4.12, Table 4.8). This implies that the seed-based functional differences between the three groups (SZ, BP, and controls) in these regions will be deduced differently in DC and NDC datasets.

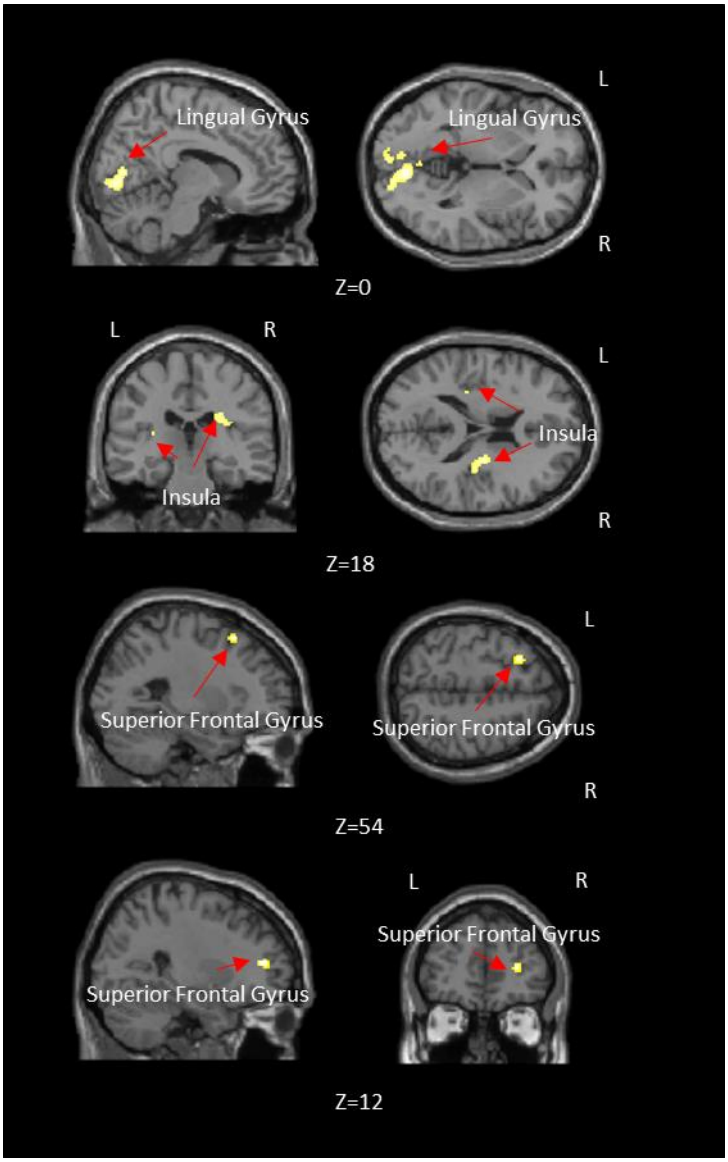

Figure 4.12. *Brain regions showing significant (p-value<0.05, FDR corrected, cluster>40) interaction between the group factor (Control vs BP vs SZ) and the deconvolution factor (data with and without deconvolution)*

Table 4.8. *Anatomical labels, cluster size and p-value of local maxima in brain areas showing significant interaction (p-value<0.05, FDR corrected, cluster>40) between the group factor (Control vs BP vs SZ) and the deconvolution factor (data with and without deconvolution)*

Cluster anatomical location	Peak coordinates			Cluster size	Hemisphere
	x	y	z		
Lingual Gyrus	-8	84	-4	728	Bilateral
Insula	-30	-28	12	42	left
Insula	30	-18	22	190	Right
Superior Frontal Gyrus	-24	20	54	45	Left
Superior Frontal Gyrus	28	44	10	41	Right

*Coordinates referring to the peak of the cluster in MNI Space.

* Anatomical labels based on Automated Anatomical Labeling (AAL)

4.4 Discussion

In this work, we test the hypothesis that neurovascular coupling mechanisms are different between SZ, BP and matched healthy control groups by characterizing such aberrations in terms of differences in the shape of voxel-specific HRFs across the groups. We employed a blind deconvolution procedure to estimate voxel-specific HRFs and demonstrate that brain regions, many of which are implicated in the pathology of SZ and BP, are characterized by HRFs whose parameters – RH, FWHM and TTP – are significantly different between the groups. One such regions, the thalamus, exhibited aberrations in all three HRF parameters between all three groups. Consequently, we calculated thalamic seed-based functional connectivity before and after deconvolution in order to characterize distortions of functional connectivity introduced by such spatial variability of the HRF when connectivity is estimated from raw BOLD data.

The variability in the shape of the HRF across brain regions and subjects due to non-neural factors tend to be more randomly distributed [47][48][91][198][199] and would tend to cancel out when comparing different populations. On the other hand, pathological alterations in neurochemicals tend to introduce more systematic differences in the shape of the HRF between groups. Specifically, Figure 4.13 shows a schematic of neurovascular coupling mechanisms which are controlled by specific neurochemicals such as GABA, serotonin, glutamate and nitric oxide (NO) [4]. The signaling pathways involving these neurochemicals couple the energy demand caused by neural activation to blood flow changes by mediating vasoconstriction or vasodilation. Specifically, GABAergic and glutamatergic interneurons release neuromodulators which could control local cerebral blood flow [200], and hence the HRF [201]. Glutamate causes dilation of blood vessels when brain regions are locally activated and this mechanism is mediated by its actions on N-methyl-D-aspartate (NMDA) receptors [111]. Quicker, taller, and narrower HRFs have been observed in regions with lower concentrations of GABA [117]. Below, we discuss previous literature showing alterations of these chemicals in SZ and BP groups and speculate on how such alterations might have resulted in HRF changes we have observed.

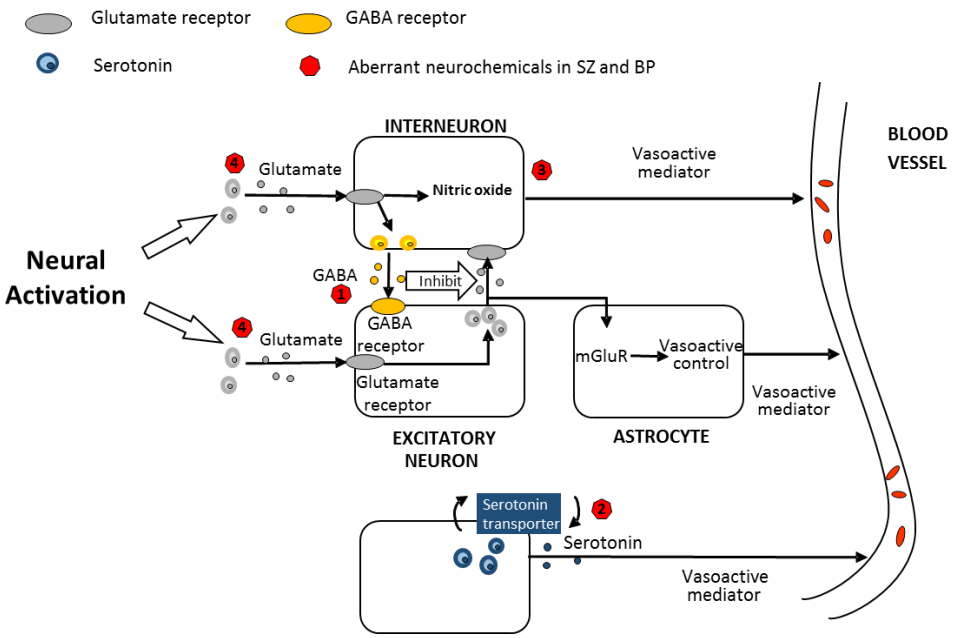

Figure 4.13 *A schematic illustrating the hemodynamic coupling between neural activity and blood flow. The HRF is a mathematical function which represents this neurovascular coupling mechanism. The aberrations of neurochemicals in SZ and BP subjects which may impact neurovascular coupling and hence the shape of the HRF are shown. Abnormalities in GABA are shown as 1, serotonin is shown as 2, nitric oxide is shown as 3, and glutamate is shown as 4.*

The resting GABA concentration is correlated with the amplitude of the hemodynamic response [112][113]. As mentioned before, quicker, taller, and narrower HRFs have been observed in regions with lower concentrations of GABA [117]. Reduced GABA in anterior cingulate cortex has been reported in SZ [202], which could result in higher RH in this region (Figure 4.3A). Decreased GABA level was reported in the medial frontal lobe in older SZ patients [203], which could explain lower FWHM we observed in this region. Further, postmortem studies linking molecular deficits with *in vivo* observations in SZ patients [204] have reported reduced glutamic

acid decarboxylase, a synthetic enzyme for GABA, in dorsolateral prefrontal cortex [205], primary motor cortex (BA 4) [206], and hippocampus [207]. We have detected shorter FWHM in dorsolateral prefrontal cortex and primary motor cortex (BA 4, Precentral Gyrus), and higher RH in parahippocampus, which reinforce the relationship between GABA and the shape of HRFs. The altered expression of GABA receptors also suggests altered GABA concentration; however, their precise mechanistic relationship is unclear.

Unlike SZ, relatively fewer studies have investigated neurochemical alterations in BP. For example, a higher GABA concentration was reported in anterior cingulate cortex [208], which could produce an HRF with wider FWHM in this region (Figure 4.3B). Also, reduced protein expression of the GABA receptor was reported in cerebellum [209], which may be related to the lower RH, FWHM and TTP we found in BP (Figure 4.3B). More studies are needed to investigate neurochemical alterations in BP and further elucidate possible mechanisms by which they could explain HRF alterations in this population.

Serotonin is a powerful vasoconstrictor [8] and hence has the potential to affect the shape of the HRF. However, unlike GABA, less is known about how serotonin impacts HRF parameters. Previous studies have detected aberrations of the serotonergic system both in SZ [61][183][210][211] and BP [64][211][212][213] populations. In the SZ group, several aspects of serotonin expression were altered in the cerebellum, including mRNA, protein and binding sites of serotonin gene [214]. The serotonin binding site densities were reported to be significantly increased in dorsolateral prefrontal cortex, anterior cingulate cortex, and parahippocampal gyrus;

and the serotonin receptor mRNA abundance was reported to be reduced in dorsolateral prefrontal and anterior cingulate [215]. There findings might be related to the altered HRF shape observed by us in these regions (Figure 4.3A). In the BP group, the mean serotonin transporter binding potential was reported to be aberrant in the thalamus, dorsal cingulate cortex, medial prefrontal cortex [216] and anterior cingulate cortex [217]. These aberrations could potentially alter the HRF shape in these regions (Figure 4.3B).

Glutamate tigers astrocytic activation, which can release a number of vasoactive molecules to regulate vascular tone, including vasodilation and vasoconstriction [9]. Therefore, the aberrant glutamate level and the dysfunction of glutamate receptors on astrocytes could disrupt normal neurovascular coupling and give rise to altered shape of the HRF. In SZ, higher expression of glutamate transporters [218] and decreased glutamate receptor binding [219] had been demonstrated in the thalamus. Increased subunit mRNA expression of NMDA glutamate receptors was found in the prefrontal lobe [220]. Postmortem studies have reported increased expression of glutamate transporters in the dorsolateral prefrontal [221] and anterior cingulate cortices [221][222]. In the BP group, absolute concentrations of glutamate was observed to be significantly higher in the anterior cingulate cortex and medial prefrontal lobe [223]. Elevated thalamic N-acetylaspartate, a reservoir for glutamate, was reported in males diagnosed with BP [224]. Decreased mRNA expression of glutamate transporters has been reported in the medial temporal lobe of participants with BP [225]. Taken together, previously reported alterations of the glutamatergic system in SZ and BP, could in principle, alter HRF shape in the corresponding

regions (Figure 4.3).

Nitric oxide modulates neurovascular coupling as a vasodilator [138][139]. In the SZ group, increased nitric oxide synthase have been reported in cerebellum [226], a region which also showed altered HRF shape in our study (Figure 4.3). For the BP group, literature on regional alterations of NO are sparse. However, the contribution of NO to the pathology of BP was confirmed by Savas et al [227].

We detected a cluster of voxels within the thalamus (Figure 4.4A) that showed significant differences in the HRF parameters across all three groups. According to the Morel thalamic atlas [194][195], the thalamus seed we have used encompasses the MD nucleus, the Hb nucleus and the CL nucleus (Figure 4.4C). Diffusion tractography studies have suggested a high probability of structural connections between caudodorsal MD nucleus and medial frontal/cingulate cortex as well as dorsolateral frontal cortex [228]. CL nucleus was shown to be connected with the basal ganglia in animals [229][230][231]. Although reports of specific connections from the human CL nucleus were not to be found, the intralaminar nucleus, which includs the CL nucleus, was reported to be connected to the basal forebrain, cerebral cortex, basal ganglia, sensori-motor cortex, and hypothalamus by a diffusion tensor tractography study in humans [232]. Also, by registering our thalamic seed on the Oxford thalamic atlas based on diffusion tractography [193] (Figure 4.4B), we found that the strucutral connections from our thalamic seed with the temporal and pre-frontal lobes showed the highest probability. Kumar et al [233] proposed a thalamic parcellation based on both rs-fMRI functional connectivity and structural connectivity of the thalamus. They compared

their parcellations with the Morel atlas as well [194][195]. They reported that their parcellated thalamic clusters which overlapped with MD and CL thalamic nuclei exhibited notable differences in their structural as well as functional connectivity with the rest of the brain. Direct and indirect tracts from MD and CL were reported to be confined to the posterior fornix, precuneus, posterior cingulum, hippocampus including the parahippocampal gyrus, subthalamic nucleus and brainstem. On the other hand, rs-fMRI functional connectivity analyses by Kumar et al reported that MD and CL were functionally connected at rest with the occipital and parietal lobes, the temporoparietal junction, pre- and postcentral gyrus, cuneus, inferior and medial temporal lobe, the anterior cingulate, and parts of the medial and lateral prefrontal cortex. The Hb nucleus has been shown to be structurally connected to both the limbic system and key brainstem nuclei [234][235]. Literature indicates that the Hb nucleus may act as a hub between forebrain and midbrain regions.

The connectivity of the cerebellum and the thalamus is complex. The thalamus receives major projections from the cerebellum [236][237] and different thalamic nuclei mediate the relationship between the cerebellum and different parts of the cortex [238][239][240]. The ventral lateral thalamic nuclei that receive projections from the deep cerebellar nuclei [241] through three distinct routes. The direct route passes in the anterolateral direction under the thalamus and enters from the ventral side. The second route following the posterior pathway turns dorsally from the midline at the posterior side of the thalamus, entering the thalamus from various positions. The third route following the anterior route passes laterally in the subthalamus and enters the external medullary lamina. Within the lamina, fibers turn posteriorly and enter the dorsal side of the thalamus [242].

Divergent pathways originate from the same axon but travel different routes and target different terminal fields. Previous studies also reported aberrations in thalamic connectivity in SZ [243][244][245][246] [247] and BP [247][248] similar to those found by us and we will not elaborate on them further here. Taken together, these patterns of connectivity between the MD, CL and Hb thalamic nuclei and the rest of the brain, as well as those between the cerebellum and thalamus found in previous studies are in general agreement with functional connectivity obtained from our thalamic seed in controls, as well as observed aberrations of such functional pathways in SZ and BP disorders.

It is noteworthy that the group connectivity patterns were different between DC and NDC data (Figures 4.5, 4.6, 4.7). In some instances, although similar overarching regions were identified with both DC and NDC data, the size and peak co-ordinates of some clusters were shifted. In other instances certain between-group differences of functional connectivity were observed only in the DC dataset. For example, aberrant connectivity between the thalamus and right caudate in SZ and BP group were detected only in the DC dataset (Figure 4.11A) but not in the NDC dataset (Figure 4.11B). This makes sense given that the caudate is structurally connected specifically with the MD nucleus in the thalamus [249][250] which was part of our thalamic seed.

Finally, we applied repeated-measures ANOVA to investigate whether brain regions show an interaction between deconvolution and group factors. We found that the interaction effect was exhibited in the functional connectivity paths between the thalamus seed and the following regions: bilateral lingual gyrus, bilateral insula and bilateral superior frontal gyrus (Figure 4.11, Table 4.9).

This implies that the connectivity differences across the groups between the thalamic seed and these regions would be deduced differently in the NDC and DC datasets. This finding suggests that if the estimated functional connectivity should be interpreted purely in terms of the underlying neural metabolism rather than in terms of non-neural and neural (such as neurovascular signaling mechanisms) components affecting the HRF, then it would be preferable to characterize functional connectivity in the latent neural space rather than the raw BOLD space.

The limitation of this study is that we investigated the effect of HRF variability only on thalamus-seed based connectivity pattern in the three groups. However, a similar analysis at the whole brain level, though computationally expensive, may provide a more complete picture. Also the discussion we provided regarding how the neurochemical factors might affect the shape of the HRF is still speculative. In the absence of direct measurement of neurochemicals (using *in vivo* MR spectroscopy, positron emission tomography or single-photon emission computed tomography) in regions showing alterations in the shape of the HRF, it is not possible to make definitive claims regarding how these neurochemicals might control different aspects of the HRF shape.

Chapter 5

Enhancing Creativity and Insight using fMRI Neurofeedback

Abstract

The neural correlates of creativity, specifically insight, is a matter of intense interest. Insight problem-solving is not deduced logically and the solution is typically very hard to get (probability of success approximates 0% [40]) and requires "out of the box" thinking . By using the transcranial direct current stimulation (tDCS), Chi et. al. [66] demonstrated that increasing the excitability of the right anterior temporal lobe (rATL) mitigated cognitive biases and enabled surprisingly large number of people to solve insight problems such as the nine-dot puzzle. Here we test this hypothesis using real-time fMRI (rt-fMRI) based neurofeedback under the premise that if subjects are enabled to up-regulate activity in their rATL using neurofeedback, it must mimic the effect of tDCS and hence enable them to solve the problem. Our results show that approximately 40% of subjects were able to solve the nine-dot problem using rt-fMRI neurofeedback, which is similar to the percentage of subjects who were able to solve the puzzle using tDCS as reported by Chi et al. Subjects who solved the puzzle were able to significantly up-regulate activity over their rATL as compared to those who did not. Further, the rATL was predominantly driven by other (specifically, frontal) regions in unsuccessful subjects while it predominantly drove other regions in successful

subjects. The frontal regions are likely involved in top-down modulation (which impose cognitive biases while solving problems) of temporal regions, forcing individuals to see a Gestalt, i.e. a square bounding box for the nine dots, which likely prevents them from "thinking out of the box". Therefore, up-regulation of activity in rATL will likely mitigate this bias. Furthermore, our study demonstrates that neurofeedback could potentially be used to mimic effects similar to brain stimulation techniques such as tDCS. This provides a likely framework for cross-pollination between brain stimulation and neurofeedback paradigms.

Key works: Insight Problem Solving; Real-time fMRI; Effective Connectivity; Dynamic Granger Causality.

5.1 Introduction

Insight problem solving is generally characterized by a time interval wherein it does not appear to the subject that he/she is progressing towards the solution in a logical step-by-step manner, followed by a rapid arrival to the solution. Consequently, the subject is not able to trace back on how he/she arrived at the solution, and the solution simply appears to occur to them from nowhere. This creates a subjective "aha!" experience for the subject [251]. Human creativity is thought to follow the framework outlined above for insight problem solving, although all creative expressions are not necessarily borne out of the necessity to solve a problem. Therefore, creativity has a broader context and insight problem solving is a specific instantiation of the creative thought process. Although insight problem solving shares common underlying cognitive processes (e.g. memory retrieval, decision-making, categorization, and perception) with most other types of

solving strategies, it differs from common problem solving in that the key to generating the solution is conceptual restructuring rather than analytical thinking. Specifically, Ohlsson [252] suggested that the insight problem solving is best described as "impasse followed by restructuring". During insight problem solving, the solvers try to minimize the difference between the current state of problem solving and the goal state. Insight occurs only when the solver realizes that the following analysis steps couldn't achieve the goal and that a new analysis must be sought.

With the development of neuroimaging techniques such as functional magnetic resonance imaging (fMRI) and electroencephalography (EEG), investigations into the neural basis of insight problem solving and creativity have characterized brain activations throughout the solving period. Accumulated evidence indicates the dominant involvement of the right hemisphere in insight problem solving [253][254][255][256][257]. Many have theorized that insight problem solving involves several component processes [258][259][260][261]. Accordingly, many have tried to explain insight problem solving in terms of two cognitive processes separately. Breaking the mental set [262][263] or cognitive restructuring is considered as one of the key processes. A mental set is defined as the tendency to solve problems in a fixed way based on previous solutions to similar problems [264]. Therefore, breaking the mental set is defined as the moment when the subject realizes that the solution requires different methods and tries to move away from the current mental set. Another important process is forming novel associations, which refers to associating existing concepts or skills in novel ways based on current task demands [265]. Existing empirical evidence does not allow for any systematic conclusion that isolates the neural correlates of these

two processes. However, experimental paradigms that emphasize one process over another could provide the neural basis of these two processes and reveal different parts of insight problem solving. Ding et al [266] suggest that the cingulate gyrus may be involved in detecting conflict and breaking mental set, middle and inferior frontal gyrus may play an important role in cognitive restructuring, and inferior parietal lobule, and the superior temporal gyrus may be associated with forming novel association. Qiu et al [267] required participants to find the solution on their own initiative during solving Chinese logogriphs, and suggested that the precuneus might be involved in retrieval of heuristic information, left inferior/middle frontal cortex might be related to breaking the mental set and forming novel associations.

Regions within the temporal cortex have been consistently identified as essential for creativity and insight problem solving. Specifically, superior temporal gyrus in the right anterior temporal lobe (rATL) has been highlighted because EEG data revealed a sudden burst of high-frequency (gamma-band) neural activity in rATL prior to the emergence of insight solutions [255]. Other studies have revealed an increased fMRI signal in the right anterior superior temporal gyrus for insight but not non-insight solutions [255][262]. Taking cue from these results, Chi et al [66] applied transcranial direct current stimulation (tDCS) to inhibit the activation of left anterior temporal lobe (lATL) and facilitate the activation rATL, while participants were engaged in solving an inherently difficult insight problem called the nine-dot puzzle [268]. They showed that tDCS enabled a surprisingly large number of people (40%) to solve the nine-dot puzzle while the probability of an individual solving the nine-dot puzzle without tDCS is close to zero [40]. The

nine-dot problem requires that nine dots be arranged in a square connected by four straight lines drawn without lifting the pen from the paper and without retracing any lines (Figure 5.1). This problem is ridiculously simple in the formal sense that there are only a few possible solutions to try, but ridiculously difficult in the psychological sense that the probability of success approximates 0% [40]. The explanation for this phenomenon is because our brains, especially the left hemisphere, are wired to interpret the world though the filter of our past experiences, and we are inclined to see the nine-dots as a square, with imposed rigid boundaries. This mechanism is mostly unconscious and cannot be easily overridden. In Chi's study [66], they showed that tDCS enabled a surprisingly large number of people (40%) to solve the nine-dot puzzle while the probability of an individual solving the nine-dot puzzle without tDCS is close to zero [40].

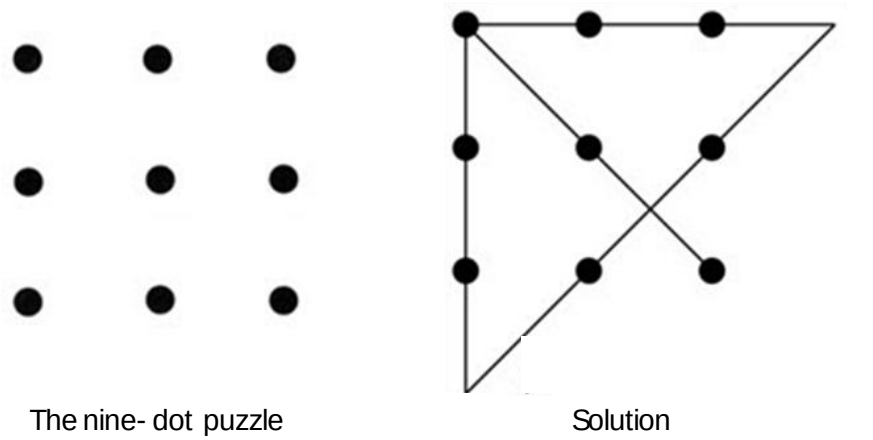

Figure 5.1 *The nine-dot problem and its solution.*

Inspired by this work, we hypothesized that real-time functional magnetic resonance imaging (rt-fMRI) neurofeedback [34] can mimic the effects of tDCS and enable individuals to solve the

nine-dot puzzle. Specifically, when an individual is solving the nine-dot puzzle inside an MRI scanner, we extracted the signal from the participant's rATL and provided that as a feedback to the participant in near real-time. The participant was required to adopt strategies for solving the nine-dot puzzle which increased the rATL feedback signal. We hypothesized that this will mimic the excitatory effects of tDCS on rATL and enable about 40% of the subjects to arrive at the solution. Further, using brain connectivity modeling, we contrast brain networks obtained from individuals who solved the puzzle versus those who did not, providing putative neural mechanisms underlying creativity and insight problem solving

Rt-fMRI neurofeedback allows participants to selectively regulate their own brain activity by gaining volitional control over the BOLD signal from specific regions of their own brains provided as a feedback [34][35]. The self-regulation of brain activity has been achieved in various regions, e.g., the anterior cingulate cortex for pain control [36], the amygdala for the emotional regulation of fear [37], etc. The learned control over the local brain activity via rt-fMRI neurofeedback training were also demonstrated to lead to specific changes in behavior [34][35]. However, our proposal to use rt-fMRI as a non-invasive proxy for brain stimulation is novel.

Finally, using post-hoc analysis of task data, we investigated brain regions differentially activated in individuals who were successful in solving the puzzle with the aid of neurofeedback versus those who were unsuccessful. Further, we also characterized the underlying directional brain networks in these groups of participants in order to understand the role of top-down inputs into the rATL in enhancing or suppressing creative insight.

5.2 Methods

5.2.1 Participants

The sample consisted of 26 healthy participants (13 women, 13 men), aging from 22-28 years (averaged age: 24.8 years). Participants had no history of psychiatric or neurological disorders and were compatible to be scanned in an MRI scanner. Further, they were interviewed before recruitment to make sure that they had not heard of the nine-dot puzzle and did not know the solution to the puzzle *a priori*. The research protocol was approval by the Institutional Review Board (IRB) at Auburn University. All subjects provided written informed consent. Three participants were excluded due to unacceptable data quality. The analyzed data consisted of 10 participants who solved the nine-dot puzzle and 13 participants who did not.

5.2.2 Experimental Design

Protocol

Participants were informed that they would receive a neurofeedback signal that represents the activation of a specific region of their own brain throughout the scans. The BOLD signal from the rATL region was shown to the participants as an increasing/decreasing curve. The participants were instructed to attempt to solve the nine-dot problem by pursuing strategies that will enhance the neurofeedback BOLD signal. A button box was given to the participants and they were asked to press a specific button when they thought that they had arrived at the solution. This was done in order to record the moment in time when the participants solved the puzzle and the scanning continued irrespective of the button press.

The experimental paradigm consisted of 4 runs per subject. Each run had 300 TRs (TR=2s) in total. The block design consisted of 10 TRs of rest followed by 20 TRs of task, which repeated throughout the whole run, as depicted in Figure 5.2.

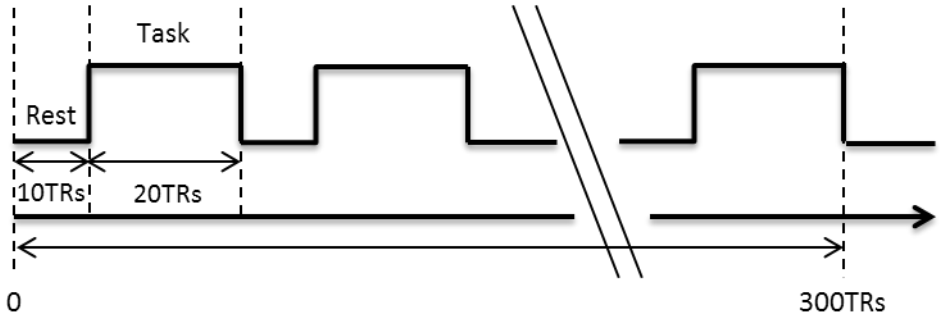

Figure 5.2 *fMRI block design consisted of rest blocks (10 TR) and task blocks (20TR) alternating each other. Each run consisted of a total of 300 TRs (TR=2s). During the task blocks, participants attempted to solve the puzzle while receiving neurofeedback, and were asked to adopt strategies that increased the neurofeedback signal.*

Behavioral report

Before the scan, the subjects were instructed as following: (1) Try to solve the problem when the color of line turns red and a word of "task" shows up (Figure 5.3). (2) Rest when the color of line turns blue and a word of "rest" shows up (Figure 5.3). (3) During solving the problem, try to increase the changing curve which represents the increasing activity in rATL (Figure 5.3). (4) Hit the button box right after they think they have solved the problem. (5) After hitting the button box, keep thinking the problem, check the answer (because their answer could be wrong), and continues controlling the curve. The button box could be hit for multiple times if they think the new solution is right. (6) We will check the answer and time of right solution appearing with them after each run.

After each run, the subjects were pulled off the scanner. We checked the following questions with subjects: Whether they have the solution; Whether the solution is right; how many times they had hit the button and which one is the time they had the right solution? Especially after first and second runs, the subject were asked about their performance of mastering the instruction. We asked them that whether they have actual rest during the rest block, and whether they have the feeling of they can control the curve.

After four runs, we talked with the subjects. In successful group, the subjects exhibited comprehension of the whole task. Most of them stated that when they focus on insight problem solving, the curve goes up very easily. When they try to think about something else, such as music, movies, the curve goes down quickly. And most of them stated that they felt they started generating control to the curve in second and third run. In unsuccessful group, most subjects stated they didn't feel that they have acquired the ability in managing the curve. Also, they couldn't build the connection of their problem solving with the changing of curve.

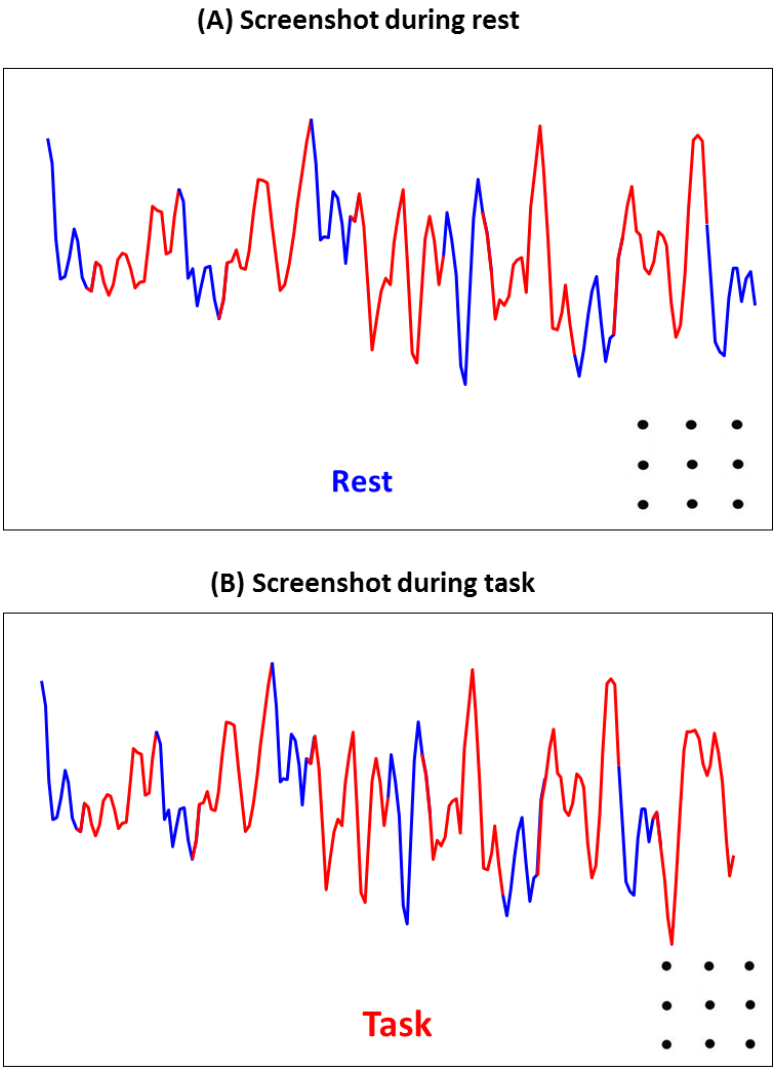

Figure 5.3 *The screenshot of feedback image provided to the subjects. (A) A screenshot during the rest block. The blue line and a blue word of "rest" are provided to remind subjects for resting. (B) A screenshot during task block. The red line and a red word of "task" are provided to remind subjects of performing task. A picture of nine dots is provided at the left button of screen for reminding the problem to subjects. The changing image is adjusted to fit the size of screen automatically.*

5.2.3 Real-time Data Acquisition

The subjects were scanned in a 7T Siemens MAGNETOM scanner. For each subject, a high-resolution anatomical scan was acquired using a magnetization-prepared rapid gradient echo (MPRAGE) sequence with repetition time (TR) = 2200 ms, echo time (TE) = 2.9 ms, inversion

time (TI) = 105 ms, flip angle (FA) = 7°, number of slices =256, slice thickness = 0.7mm, and field of view (FOV)=224mm. After the anatomical images were collected, functional images were acquired by using an echo-planar imaging (EPI) sequence with TR = 1500 ms, TE =25 ms, number of slices =32, voxel size=3.0×3.0×3.0 mm^3, FOV=192 mm, flip angle =70°, and 300 measurements. A 32-channel head coil (Nova Medical) was used. During each scan, after on-line reconstruction of the data, the images were sent to a computer (Figure 5. 4 C) where the data was subjected to accelerated motion correction as described in Scheinost et al [269] and temporal denoising by using the Yale BioImage Suite software [270] (www.bioimagesuite.org). The feedback signal was selected from a pre-defined ROI of rATL (central MNI coordinates: x: 45; y: -9 ; z:-47) and displayed to the subject as a changing curve via Avotec's MR-compatible projection system. The BioImage Suite software package has the ability to process data in near real-time. The time lag between actual brain activity and the display of feedback signal was under 2s. The system architecture is illustrated in Figure 5.4.

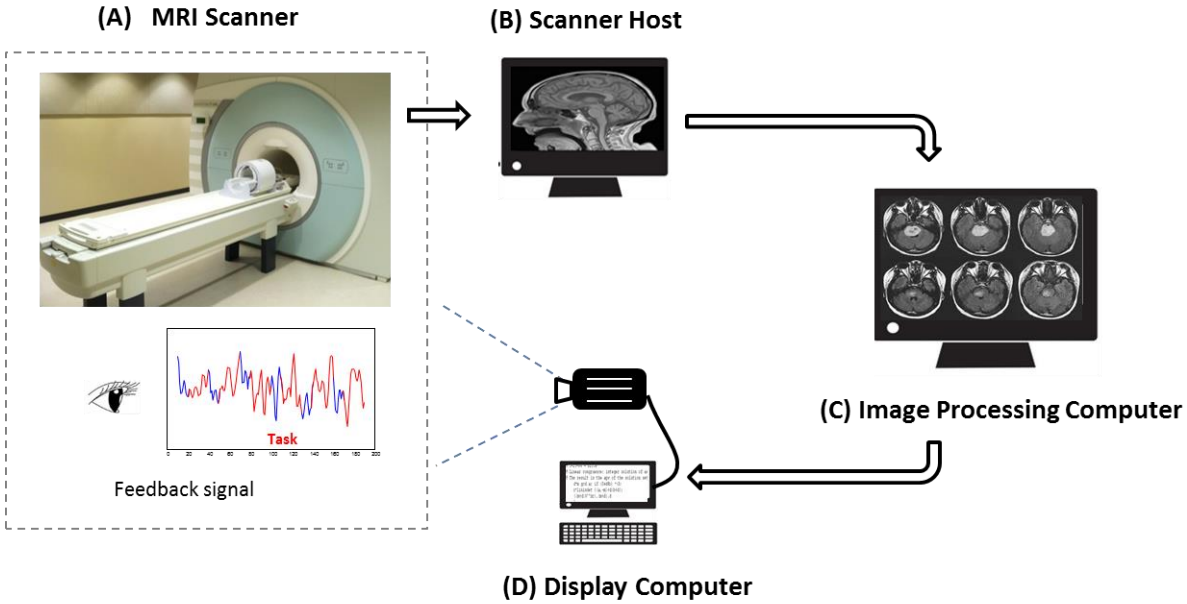

Figure 5.4 *The experimental setup for real time fMRI which consisted of (A)The 7T MRI scanner, (B) Scanner host computer, (C) Image processing computer, and (D) Display computer with projector. The raw k-space MR data were processed by the reconstruction system on the scanner host computer, which creates images of each slice/volumes. The image processing computer retrieved slices/volumes from the scanner host computer and analyzed slices/volumes in real time by using BioImage Suite software. Its output was the fMRI signal from the rATL ROI which was sent to the display computer to be shown to the subject as a curve. When the curve goes up (or down), it represented increased (or decreased) brain activity.*

5.2.4 Image Processing before Biofeedback Scans

The rATL ROI was defined in MNI space. In each scanning session, after the anatomical images were collected, the rATL ROI was pre-transformed from the MNI space to the functional space of the given subject using three concatenated transformations (Figure 5.5A). Firstly, the rATL ROI was transferred from MNI space to the given subject's MPRAGE image by applying nonlinear registration (Figure. 5.5B). Secondly, axial adjustment of rATL ROI was performed by applying a linear rigid transformation to the space of the given subject's axial-oblique anatomical data [271] (Figure. 5.5C). Lastly, the structural images of rATL ROI were registered to the

individual's functional space by applying a linear rigid transformation (Figure 5.5D). All transformations were performed by using appropriate modules of the Yale BioImage Suite software package, including "combine transformations", "linear registration", "linear RPM" etc. [270]. In this manner, the rATL ROI was translated into the functional space of each participant before the neurofeedback scans involving four EPI runs.

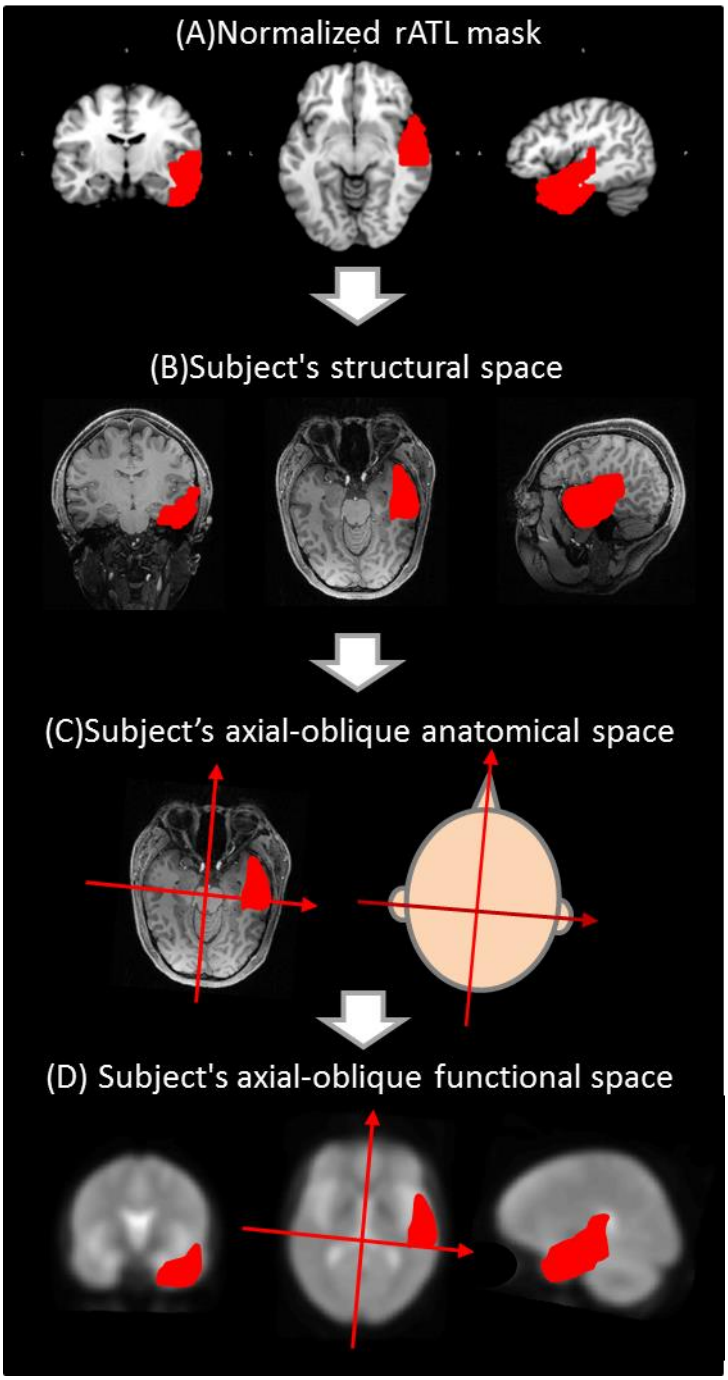

Figure 5.5 *Illustration of the registration of the normalized rATL mask into the space of subject's functional space. (A) The normalized rATL mask as defined on the MNI space. (B) The transformed (via a nonlinear registration) rATL mask in the space of the subject's high-resolution structural data. (C) The transformed rATL mask in the space of the subject's axial-oblique anatomical data. (D) The transformed rATL mask in the space of the subject's axial-oblique functional reference space.*

5.2.5 On-line Real-time fMRI Process

In this system, the on-line rt-fMRI image processing was implemented by modifying the image reconstruction pipeline of Siemens' Image Calculation Environment (ICE) [269]. More specifically, a new local “functor” was inserted in the online processing chain, immediately after each slice of the image was acquired and reconstructed by scanner host (Figure 5.4 B) and before the scanner host sent image to real-time system (Figure 5.4). This “functor” wrote the slice image as a file in a directory accessible to a separate image processing computer (Figure 5.4 C) connected by local area network. Since the strategy of real-time fMRI is minimize the delay of processing raw image associated with standard offline methods. The image processing computer applied “image analysis program” (a module of BioImage Suite: www.bioimagesuite.org) to accelerated the motion correction in real-time. The system takes advantage of the interleaved acquisition of fMRI (where the odd-numbered slices are acquired first followed by the even-numbered slices). The image processing computer (Figure 5.4C) read and stored the slices in local memory as they appeared. When all the odd slices had arrived, the “image analysis program” computed a linear rigid transformation between the incoming data and the functional reference volume. Once the complete volume had arrived, the computed transferred function was applied to transform the given volume into the space of the functional reference volume. Through this manner, the accelerated motion correction would be achieved. The average signal in the rATL ROI was then computed and sent to the display computer (Figure 5.4D) via serial port. In the display computer, the stimulus/neurofeedback presentation was executed.

5.2.6 Offline Pre-processing

Pre-processing was performed offline using the Data Processing Assistant (DPARSF) toolbox [99] based on Statistical Parametric Mapping (SPM8) software package [100]. The first five images were discarded to ensure the equilibration of magnetization. The images were preprocessed separately for each subject with the following steps: slice timing correction by shifting the signal measured in each slice relative to the acquisition of the slice at the mid-point of each TR, realigning of all the images using six rigid body parameters (registered to the first image and then registered to the mean of the images after the first realignment) in order to correct for motion. For every individual, the functional images were co-registered to the structural images (T1-weighted MPRAGE) by using a linear transformation as well as spatially normalized to the MNI avg152 T1 template, in MNI stereotaxic coordinates. The functional images were spatially smoothed with a 2 mm^3 full-width at half-maximum (FWHM) Gaussian smoothing kernel [272]. Head motion effects and low frequency scanner drifts were regressed out from the fMRI signal by utilizing a 24-parameter (6 head motion parameters, 6 head motion parameters one time point before, and the 12 corresponding squared items) model [102]. The signals from white matter and cerebrospinal fluid were regressed out to reduce respiratory and cardiac effects.

5.2.7 Offline Analysis of fMRI Task Data

As mentioned above, the experimental paradigm required participants to adopt problem solving strategies that would up-regulate the BOLD signal extracted from the rATL region of their own brains and provided as a neurofeedback signal during the task blocks. We predicted that this

would enable the subjects to solve the nine-dot problem. In order to understand the neural basis of success or failure in solving the nine-dot problem, we estimated the incremental task-induced BOLD signal change in the rATL across runs. For each run and subject, the preprocessed BOLD signal was abstracted from the rATL ROI mask used during neurofeedback in the data acquisition phase. The signal changes in rATL averaged over individual task blocks relative to the baseline was computed individually for each subject on a trial-by-trial basis. More specifically, the incremental percentage BOLD signal change was computed by using the following equation:

$$\Delta\text{signal} = \frac{\text{mean(task)} - \text{mean(rest)}}{\text{mean(rest)}} \times 100\% \quad (5.1)$$

Furthermore, a linear regression analysis that used the trial-specific signal changes as the dependent variable and time as the independent variable was conducted to evaluate the learning effects over time.

The increment of corrected $T2^*$-weighted images during regulation with respect to the baseline was evaluated by using SPM8. Voxels showing significant positive changes during task blocks with respect to the baseline were inferred to be activated. This resulted in statistical contrast maps showing activated regions for each participant separately. In order to understand the neural basis of success or failure in solving the nine-dot problem, we divided the sample into two groups – those who were successful in solving the nine-dot problem and those who were not. In the current study, 10 subjects solved the nine-dot problem and were designated as the 'successful group', while 13 subjects did not solve the nine-dot problem were defined as the 'unsuccessful group'. The statistical contrast maps from individual were input into a random-effects one-sample t-test to

assess group-level activation maps separately in both the groups. The statistical contrast maps from individual subjects in both the groups were also compared directly using a random-effects two sample t-test. The between-group activation differences were examined using the following contrasts: successful group> unsuccessful group and unsuccessful group > successful group. The location of activated clusters (in MNI coordinates) at a significance level of $p < 0.05$ FDR corrected was determined.

5.2.8 Offline Analysis of Effective Connectivity Networks

ROI Definition

We aimed to examine the patterns of connectivity between brain regions involved in solving the nine-dot puzzle and investigate differential connectivity patterns in individuals who were successful in solving the puzzle as compared to those who were not. We selected 9 ROIs activated by the task and identified by the GLM analysis described above. Among these, 5 ROIs were activated in the successful group > unsuccessful group contrast and 4 ROIs were activated in the unsuccessful group > successful group contrast. All ROIs were cubes of 5 mm per side, centered on the peaks of activation.

Dynamic Granger Causality (DGC) Analyses

The concept underlying Granger causality (GC) [78][78]to forecast the future of one signal "S_1" by using the past and present of another signal "S_2" [78][273][274][275]. A successful prediction is inferred as a causal influence from S_2 to S_1. The causal influences between multiple time series can be inferred by using a multivariate vector autoregressive model (MVAR)

[276][277]. In neuroimaging, the time series are obtained from activated brain regions. In this way, the MVAR model can be used to infer causal relationships between activated ROIs in brain networks [274][278][279][280]. The advantage with this approach is that it is data driven and does not require specification of candidate models as in dynamic causal modeling and structural equation modeling [275].

When using this approach in a block or event-related fMRI paradigm, it is necessary to be able to distinguish causal influences between activated ROIs during events of interest from those obtained from inter-trial intervals or control conditions. In order to achieve this, the MVAR model can be made 'dynamic' by allowing the model coefficients to vary across the time. Let us assume *k* ROI time series from *k* activated brain regions as follows:

$$X(t) = [x_1(t), x_2(t), \cdots, x_k(t)] \quad (5.2)$$

The dynamic MVAR model[81][281] is then given by:

$$X(t) = A^{(0,t)}X(t) + A^{(1,t)}X(t-1) + \cdots + A^{(p,t)}X(t-p) + E(t) \quad (5.3)$$

Where the dynamic model coefficients A are a function of both time t and model order p. It is to be noted that in $A^{(0,t)}$, diagonal elements representing auto-correlation were set to zero and only cross-correlation between time series were modeled in order to compensate for zero-lag correlation effects (referred to as correlation-purged Granger causality) [282]. The model coefficients were then estimated in a Kalman filter framework using variable parameter regression [82], which calculates the optimal set of coefficients that minimizes the model error E(t) [283]. The coefficient $A'^{(p,t)}$ indicates the degree to which the past $X(t-p)$ can predict the

present $X(t)$, where p is an arbitrary time delay or model order [83]. The sum of all coefficients corresponding to all delays at time t would be represented as:

$$DGC_{ij}(t) = \sum_{n=1}^{p} a_{ij}\,(n,t) \qquad (5.4)$$

Where a_{ij} are the elements of coefficient matrix A. In this framework, DGC_{ij} represents dynamic Granger causality and is the strength of causal relationship from ROI i to ROI j at time instant t [284]. In this study, in order to examine the causal relationships arising from neural delays less than a TR [285][286], we used a first order model by choosing the model order p as 1.

The time series to be used in the model described above were obtained from ROIs which were activated in the successful>unsuccessful as well as unsuccessful>successful contrasts (more on this in the results section). Before performing DGC analysis, deconvolution was performed on the average time series extracted from each of the ROI identified in the above contrasts separately for each run and each participant. Inter-subject and spatial variability of the hemodynamic response function (HRF) [47][48][91] could lead to false inferences of directional connectivity. This can be addressed by applying hemodynamic deconvolution, wherein the variability of the HRF and its smoothing effect can be minimized so that directional connectivity is more accurately estimated [53][287][93].

We performed deconvolution to obtain latent neuronal variables by using a blind deconvolution algorithm [72], which jointly estimates latent neuronal time series as well as ROI-specific HRF [288][289] based on the Cubature Kalman filter [290][291][292]. Further, it has been demonstrated that this model likely does not overfit the data [186]. The estimated latent neural

time series from each ROI were put into the MVAR based DGC model to estimate directional connectivity between the ROIs at each time point.

The DGC values associated with task blocks and rest blocks (Figure.5.1) were extracted for each path and each individual subject separately [293]. Then, the task-related DGC values were collated into two different samples corresponding to subjects from the 'successful group' and the 'unsuccessful group'. Connectivity paths significantly (p-value<0.01, FDR corrected) different between the groups were evaluated by comparing the task-specific connectivity samples obtained from the two groups using two sample t-tests. The connectivity paths which were significantly stronger in the successful group and vice versa were examined.

In successful group, the DGC values were also extracted in male subjects and female subjects. The altered path between genders were examined (p-value<0.01, FDR corrected) by performing two sample t-tests between the task-specific connectivity samples obtained from the male subjects and female subjects in successful group. In these contrasts, the DGC matrixes acquired from the timeseries after the occurrence of solution in successful group were not put into the analysis.

In successful group, we also extract the DGC values form the 10 task timepoints (22 seconds) before the generation of the solution and the 10 task timepoints (22 seconds) after the generation of solution. Connectivity paths significantly (p-value<0.01, FDR corrected) were evaluated.

The complete workflow of DGC analysis is depicted in Figure 5.6.

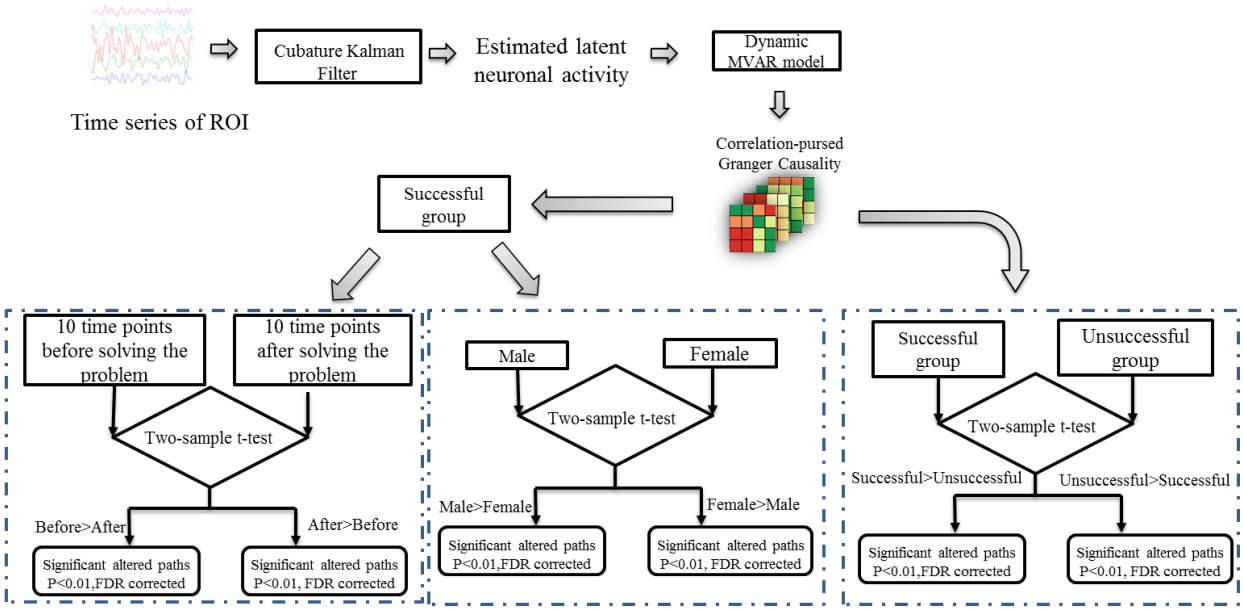

Figure 5.6 *An illustration of the workflow of DGC analysis. After deconvolution, the estimated latent neural activity of each ROI were input into the dynamic MVAR model. The significantly different (p-value<0.01, FDR corrected) paths in the contrasts of successful group>unsuccessful group, unsuccessful group>successful group were calculated by comparing the task-related DGC values between two group. In successful group, the contrast of 10 task timepoints before solving the problem between after solving the problem and the contrast between genders were calculated by comparing the task-related DGC values.*

5.3 Result

5.3.1 The rt-fMRI Neurofeedback Signal Regulation

As mentioned before, 10 subjects were successful in solving the nine-dot puzzle while 13 subjects were not. The percentage of participants who solved the puzzle (43.5%) is surprisingly similar to the percentage of participants who solved with puzzle with tDCS applied to rATL [66]. The amount of percentage signal increase in rATL that the subjects were able to achieve in each of the four runs is shown in Figure 5.7 for both the successful and unsuccessful groups. The average BOLD activity in the rATL increased progressively across the neurofeedback runs for the successful group and reached a maximum during the final neurofeedback run (run 4) (Figure 5.7,

blue line). For the unsuccessful group, the average BOLD activity in the rATL failed increase significantly beyond the first run and decreased precipitously from run-3 to run-4 (Figure 5.7, red line). The percent BOLD signal change was significantly larger in the successful group as compared to the unsuccessful group only in run-4 (Figure 5.7, asterisk). These results demonstrate the ability of the participants in the successful group to upregulate BOLD activity over their rATL region via rt-fMRI neurofeedback while the unsuccessful group clearly failed to do so. Given that all subjects reached the solution in run-4, our results indicate that more that 60% signal change in rATL may be required to gain creative insight. Since we examine the general performance of regulating rATL, and the subjects didn't stop regulation after the get the solution (cause its accuracy was not check), this analysis includes all the time series of run 4 in successful group.

A repeated measures ANOVA was performed to examine the interaction between group and BOLD signal change. We considered the 4 runs as different measurements and group as a factor. The significant interaction between runs and group was found in Sphericity assumption (Table 5.1).

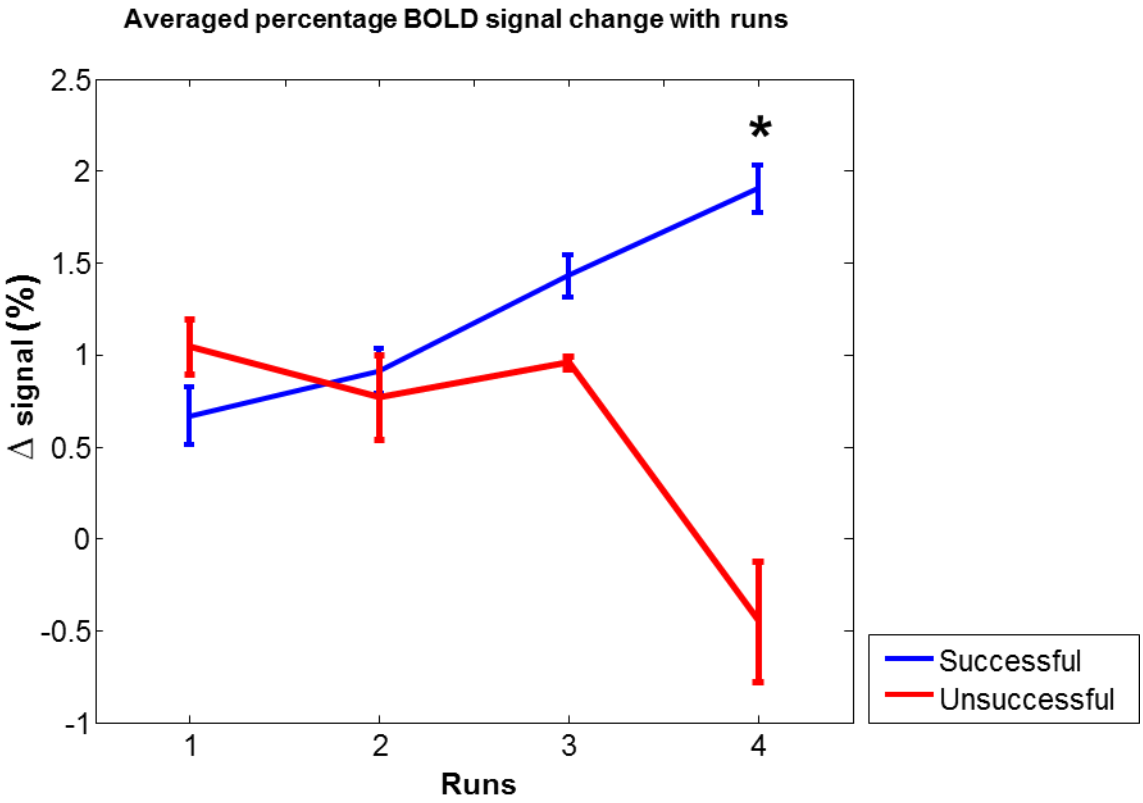

Figure 5.7 *Percentage BOLD signal change within each run and associated changes across runs (run-1 to run-4) for both the successful group that solved (blue) and the unsuccessful group that did not solve (red) the puzzle. Each error bar represents the standard derivation of percent BOLD signal change within the group. The percent BOLD signal change was significantly larger in the successful group as compared to the unsuccessful group only in run-4.*

Table 5.1 *Tests of Within-Subjects Effects*

Source		Type III Sum of Squares	df	Mean Square	F	Sig.
Percentage BOLD signal change	Sphericity Assumed	2.876	3	.959	.488	.692
	Greenhouse-Geisser	2.876	1.951	1.474	.488	.613
	Huynh-Feldt	2.876	2.251	1.278	.488	.639
	Lower-bound	2.876	1.000	2.876	.488	.492
Percentage BOLD signal change * group	***Sphericity Assumed***	***16.132***	***3***	***5.377***	***2.739***	***.050***
	Greenhouse-Geisser	16.132	1.951	8.269	2.739	.078
	Huynh-Feldt	16.132	2.251	7.168	2.739	.069
	Lower-bound	16.132	1.000	16.132	2.739	.113

Error(Percentage BOLD signal change)	Sphericity Assumed	123.691	63	1.963		
	Greenhouse-Geisser	123.691	40.970	3.019		
	Huynh-Feldt	123.691	47.262	2.617		
	Lower-bound	123.691	21.000	5.890		

*The significant is labeled as bold and italics.

5.3.2 Between-group Activation Differences

Brain regions activated significantly ($p<0.05$, FDR corrected, minimum cluster size set to 20 voxels) more in the successful group as compared to the unsuccessful group during the neurofeedback regulation task are shown in Figure 5.8. It revealed activations in the left Anterior Temporal Lobe (lATL), right Anterior Temporal Lobe (rATL), left Angular Gyrus (lAG), right Inferior Frontal Gyrus (rIFG) and right Superior Frontal Gyrus (rSFG). In contrast, brain regions activated significantly ($p<0.05$, FDR corrected, minimum cluster size set to 20 voxels) more in the unsuccessful group as compared to the successful group during the neurofeedback regulation task are shown in Figure 5.9. It revealed activations in the left Superior Frontal Gyrus (lSFG), Caudate Head (CauH), right Superior Occipital Gyrus (rSOG) and right Superior Parietal Gyrus (rSPG). Table 5.2 provides corresponding details regarding the size of the activation clusters, peak coordinates and peak intensity.

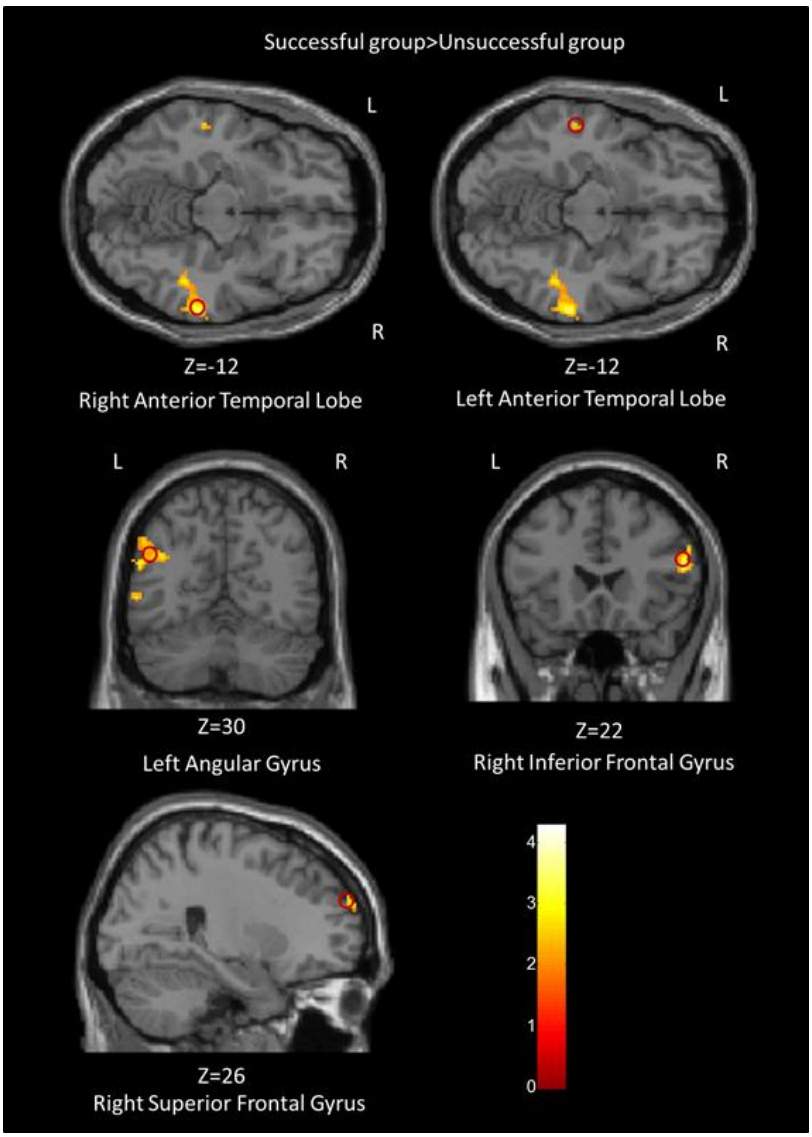

Figure 5.8 *Brain regions activated significantly (p<0.05, FDR corrected, minimum cluster size set to 20 voxels) more in the successful group as compared to the unsuccessful group during the neurofeedback regulation task. The activation maps are overlaid on a representative single-subject T1 template in the MNI space*.

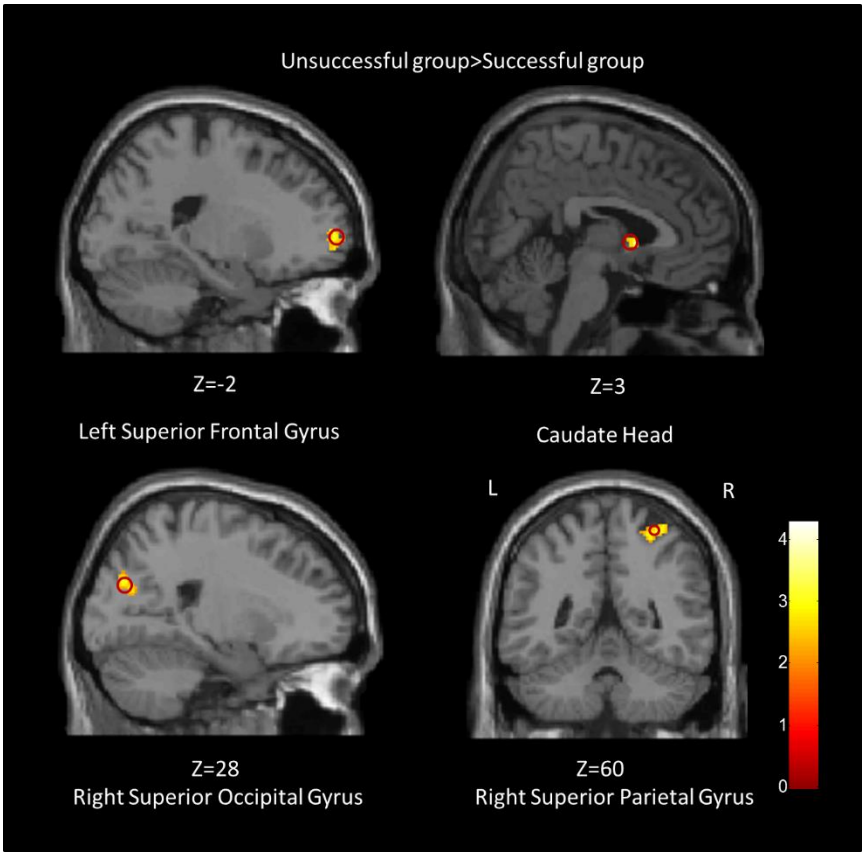

Figure 5.9 *Brain regions activated significantly (p<0.05, FDR corrected, minimum cluster size set to 20 voxels) more in the unsuccessful group as compared to the successful group during the neurofeedback regulation task. The activation maps are overlaid on a representative single-subject T1 template in the MNI space.*

Table 5.2 *Comparison of activations between the successful and unsuccessful groups*

* Coordinates referring to the peak of the cluster in MNI Space.

* Anatomical labels are based on Automated Anatomical Labeling (AAL).

* BA – Brodmann area.

Cluster anatomical location	Abbreviation	Peak coordinates			Cluster size	Peak intensity(t)	BA	Hemisphere
		x	y	z				
Successful > Unsuccessful: p<0.05 (FDR corrected), cluster size, minimum 20 voxels								
Right Anterior Temporal Gyrus	rATL	64	-34	-8	570	4.48	21 20 37	Right
Left Anterior Temporal Gyrus	lATL	-54	-30	-6	235	3.64	21	Left
Left Angular Gyrus	lAG	-54	-60	40	356	3.39	39 40	Left
Right Superior Frontal Gyrus	rSFG	24	60	28	114	3.58	10	Right
Right Inferior Frontal Gyrus	rIFG	54	22	18	137	4.17	45 9	Right
Unsuccessful > Successful: p<0.05 (FDR corrected), cluster size, minimum 20 voxels								
Left Superior Frontal Gyrus	lSFG	-20	60	4	105	3.07	10	Left

Caudate Head	CauH	6	8	2	75	4.22		Bilateral
Right Superior Occipital Gyrus	rSOG	18	-78	30	98	3.60	7	Right
Right Superior Parietal Gyrus	rSPG	36	-52	66	135	3.59	5	Right

5.3.3 Between-group Effectivity Connectivity Differences

The successful group exhibited significantly ($p<0.01$, FDR corrected) stronger connectivity paths originating from the rATL and lAG to CauH, rSPG and rSFG. The lAG also exhibited significantly stronger connectivity in targeting rATL, lSFG, rIFG and lATL. The rSOG did not exhibit higher effective connectivity related to any regions in the successful group (Figure 5.10).

The unsuccessful group exhibited significantly ($p<0.01$, FDR corrected) stronger connectivity in bidirectional paths among CauH, rIFG, and rSFG. The rSFG exhibited higher connectivity in targeting lATL, rATL, rIFG, lSFG, rSPG, and rSOG. The rIFG exhibited higher connectivity in targeting lATL, rATL, lAG, lSFG, rSPG, and rSOG. The CauH exhibited higher connectivity in targeting lATL, lAG, lSFG, and rSOG. The lATL exhibited higher connectivity in targeting lAG, rATL and lAG (Figure 5.11).

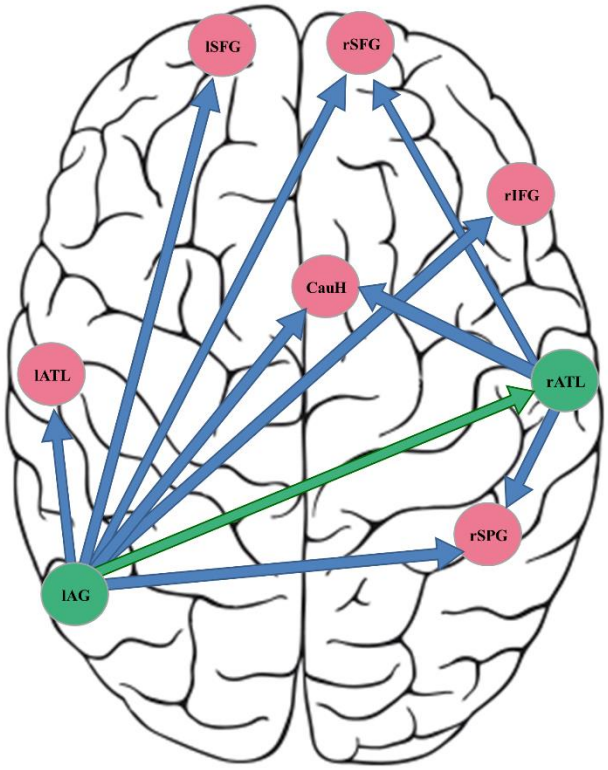

Figure 5.10 *Paths which showed significantly stronger connectivity in the successful group as compared to the unsuccessful group (p<0.01, FDR corrected) during neurofeedback regulation. Predominantly source regions are shown in green while predominantly sink regions are shown in pink. The green line represents the connectivity paths between source regions while blue lines represent connectivity from source to sink/target regions.*

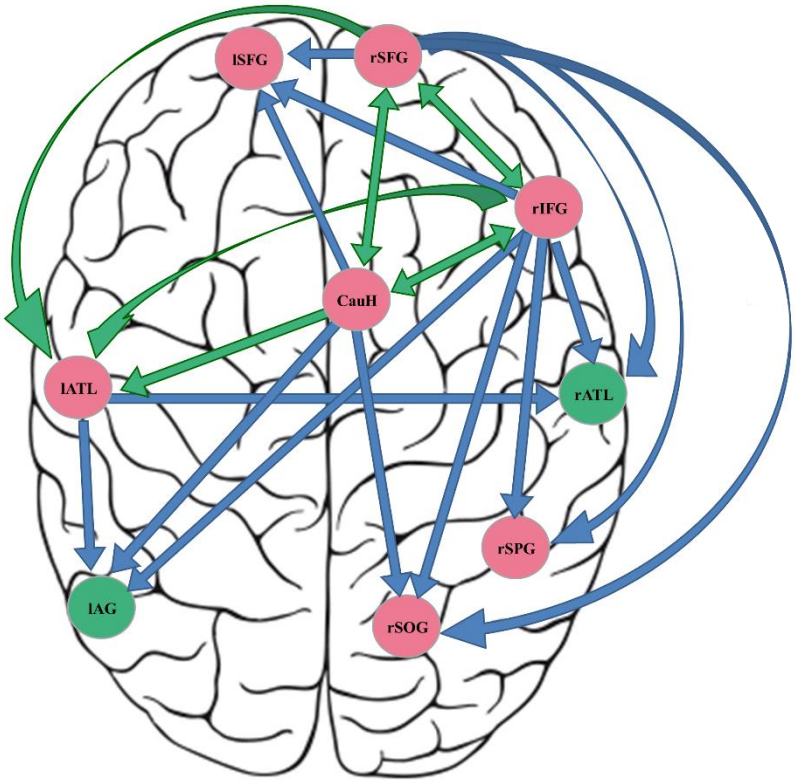

Figure 5.11 *Paths which showed significantly stronger connectivity in the unsuccessful group as compared to the successful group (p<0.01, FDR corrected) during neurofeedback regulation. The predominantly source regions are shown in green while predominantly sink regions are shown in pink. The green line represents the connectivity paths between source regions while blue lines represent connectivity from source to sink/target regions.*

5.3.4 Effectivity Connectivity Differences between Genders in Successful Group

In successful group, female subjects exhibited significantly ($p<0.01$, FDR corrected) stronger connectivity paths originating from the lAG to lATL, rIFG, rSPG than the male subjects (Figure 5.12). While the male subjects exhibited significantly ($p<0.01$, FDR corrected) stronger connectivity paths originating from the rSPG to lAG, lATL, rIFG, rSFG and CauH (Figure 5.13).

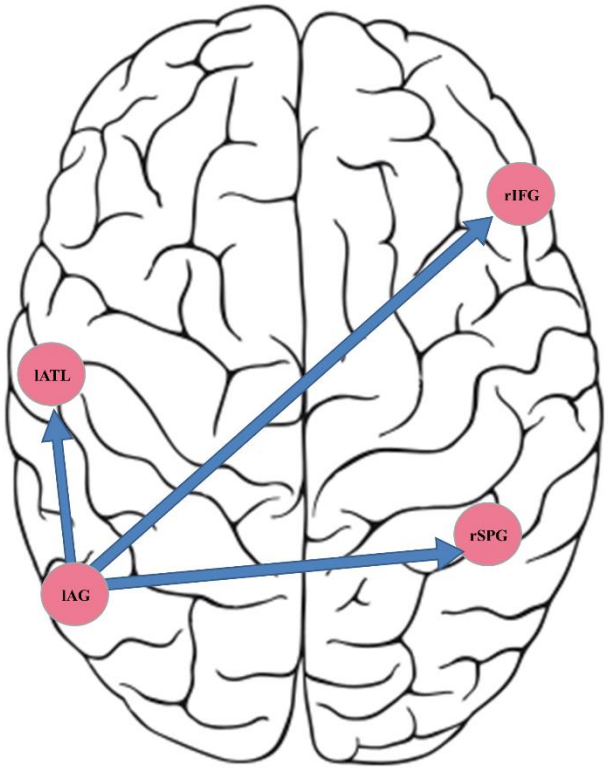

Figure 5.12 *Paths which showed significantly stronger connectivity in female subjects in successful group as compared with male subjects in successful group (p<0.01, FDR corrected) during neurofeedback regulatio.*

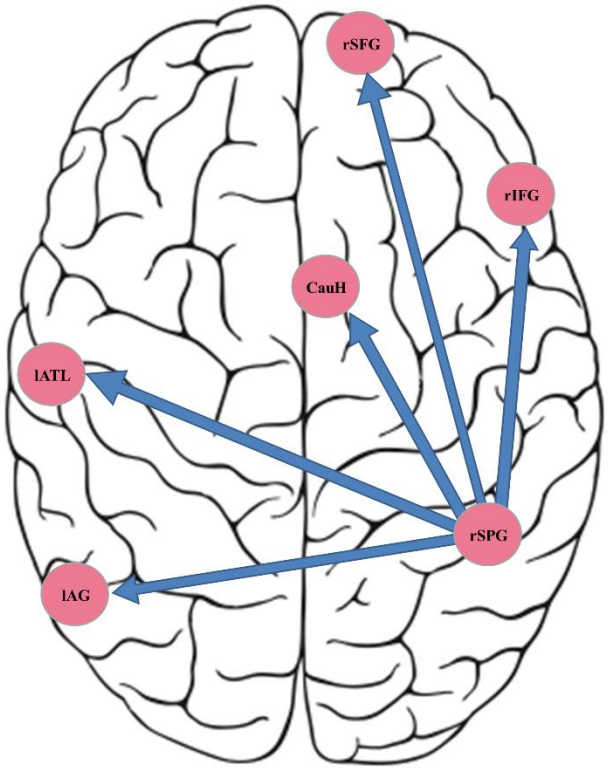

Figure 5.13 *Paths which showed significantly stronger connectivity in male subjects in successful group as compared with female subjects in successful group successful (p<0.01, FDR corrected) during neurofeedback regulation.*

5.3.5 Effectivity Connectivity Differences Before and After Generating the Solution

In successful group, the connectivity of 10 task timepoints before the generation of solution exhibited significantly ($p<0.01$, FDR corrected) stronger connectivity paths originating from the rATL to lATL, lAG, rSFG when compared with the connectivity of 10 task timepoints after the generation of solution (Figure 5.14). No stronger connectivity paths were found in the connectivity of 10 task timepoints after the generation of solution.

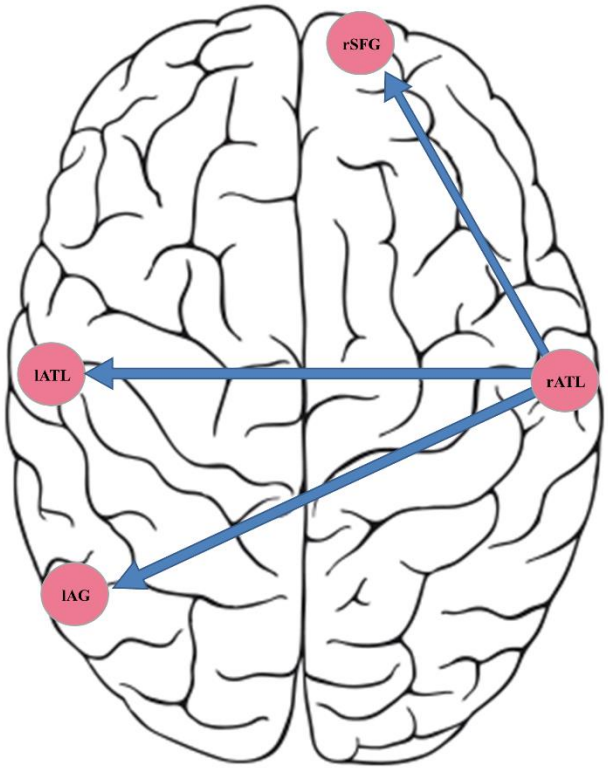

Figure 5.14 *Paths which showed significantly stronger connectivity in the 10 task timepoints before generation of solution as compared with the 10 task timepoints after generation of solution in successful group ($p<0.01$, FDR corrected).*

5.4 Discussion

The primary goal of this study was to demonstrate that rt-fMRI neurofeedback-based self-regulation of brain activity could mimic the effects of tDCS by facilitating a significant number of individuals in solving the nine-dot puzzle [66]. Specifically, we applied rt-fMRI neurofeedback by extracting the signal from rATL. This choice was inspired by previous EEG experiments that demonstrated a sudden burst of high-frequency (gamma-band) neural activity in rATL prior to the emergence of insight solutions [255] and the tDCS study that demonstrated that excitatory

stimulation over rATL could facilitate insight problem-solving [2]. In our work, 10 subjects solved the problem and 13 subjects did not (i.e. approximately 40% were successful). This result is in agreement with Chi's study [2], where 40% individuals solved the problem with the facilitation of tDCS. Thus, we concluded that self-regulation of brain activity via rt-fMRI neurofeedback could mimic the effects of tDCS .

In order to understand the neural mechanisms underlying enhanced insight problem-solving and creativity with rt-fMRI neuroffedback from rATL, we performed post-hoc analysis of the data in both the groups. For the successful group, we selected the data only from individuals who solved the problem. All such subjects did so only in the fourth run. The unsuccessful group consisted of data from subjects that completed 4 runs (to ensure that the individuals undergo rt-fMRI neurofeedback for approximately the same duration), but did not solve the puzzle. The successful group showed progressively enhanced up-regulation of the rATL signal from first to fourth runs while the unsuccessful group did not. Moreover the difference in percent signal change over rATL was significant between the groups in the fourth run when the subjects in the successful group arrived at the solution (Figure 5.7).

Post-hoc activation analysis revealed that the successful group exhibited higher activations in rATL, lATL, lAG, rIFG and rSFG (Figure 5.8). On the other hand, the unsuccessful group exhibited higher activations in lSFG, CauH, rSPG and rSOG (Figure 5.9). Since both groups performed the same task of solving nine-dot problem, these detected regions could be involved in various mental processes underlying creativity and insight problem solving. These detected brain

regions are generally consistent with previous studies. A number of neuroimaging studies have demonstrated the increased activations of the bilateral temporal cortex (rATL [255][262][294] and lATL [295][296]) during insight problem solving. The rATL was shown to be recruited before the moment at which the solution to insight problems arose [255]. The exact role of lATL in creativity and insight problem solving remains to be determined. However, recent findings suggest that lATL could be involved in retrieving and maintaining heuristic information obtained during the learning stage [297], which is necessary for all types of problem solving. The bilateral frontal cortices have also been implicated in insight problem solving [298][261][260][299]. The prefrontal cortex has been shown related to the successful execution of mental processes which are required for creativity and insight problem solving (e.g. suppressing extraneous thoughts, selecting prepotent solution strategies and shifting attention from a non-prepotent strategy) besides others [53][54][300][301][302]. The prefrontal cortex is not thought to be directly involved in generating creativity and insight. Rather, it is considered to contributes to the instigation of the creative thoughts by enabling the recognition of appropriately novel combinations of information [260], thereby aiding the breaking of conceptual constraints. There are appears to be lateral specificity in the frontal cortex. For example, the right hemisphere of the frontal cortex was found to be involved in formulating distant semantic relations [303]. This supports theories that the right hemisphere is involved in the processing of distant associations that may be useful in creative thought and problem solving [253][254][255][256][257]. This is in line with higher activation in rSFG and rIFG in the successful group (Figure 5.8) in our results.

We also detected other active regions in both groups. Higher activation of lAG was found in the successful group (Figure 5.8). The activation of lAG has been shown to be related to problem solving [304][305][306] and mental arithmetic [307]. Dandan et al concluded that the lAG might be involved in forming novel associations between insight problems and related prototypes [308]. On the other hand, higher activation was found in CauH in the unsuccessful group (Figure 5.9). The CauH is a core region of the non-declarative memory system [309][310], and its activation could be related to potential mnemonic strategies that might have been used by unsuccessful participants [311][312]. Higher activation was also found in rSOG in the unsuccessful group (Figure 5.8). rSOG is implicated in visual processing [267]. Given that Salvi et al demonstrated that sudden insight is associated with shutting out of visual inputs [313], it makes sense that we found higher activation of rSOG in the unsuccessful group. Higher activation was also found in rSPG in the unsuccessful group (Figure 5.9). Recently, increasing number of studies have reported the activation of parietal lobe [255][299] could serve broadly in associative processing [314][315], which facilitated creativity thinking. However, a study instructed participants to generate either creative or uncreative stories and found that creative (as compared to uncreative) story generation was associated with lower activity in right parietal lobe [316]. Combined with the lower activation of rSPG detected in the unsuccessful group in our result, we proposed the idea that the rSPG could be recruited in creative task, but less devotion is required in generating the creative solution.

Our results demonstrated that rt-fMRI neurofeedback not only facilitated the subjects to up-regulate the activation of targeted brain region (rATL in our case), but also to alter brain

connectivity associated with the targeted region [34][35]. Enhancement of activity in a single targeted region could propagate to other regions connected to the targeted region, either increasing or decreasing activity in those regions. Therefore, we hypothesized that connectivity associated with rATL would be significantly different between the groups. Specifically, we hypothesized rATL to predominantly receive inputs from other regions in unsuccessful subjects. This is based on previous literature speculating that top-down modulation of temporal regions by frontal regions imposes cognitive biases [317][318][319] which inhibits creativity and insight problem solving. On the other hand, in successful participants, we hypothesized that rATL would predominantly drive other regions and escape the top-down cognitive biases.

Our results indeed support the above hypothesis. We found that rATL and lAG drove rSFG, rSPG and the CanH in the successful group (Figure 5.10) while it was driven by rSFG, rIFG and lATL (Figure 5.11) in the unsuccessful group. We also found that before the generation of the solution, the rATL particularly drives the lATL, lAG, rSFG (Figure 5.14). This result is highly consistent to the EEG data that revealed a sudden burst of high-frequency (gamma-band) neural activity in rATL prior to the emergence of insight solutions [8].

In summary, the frontal regions are likely involved in top-down modulation (which impose cognitive biases while solving problems) of temporal regions, forcing individuals to see a Gestalt, i.e. a square bounding box for the nine dots, which likely prevents them from "thinking out of the box". Therefore, up-regulation of activity in rATL will likely mitigate this bias. Also, the activity in rATL is especially important in generating the solution.

Our result also indicates that the cognitive pattern under problem solving is likely different between genders. In female, the lAG drives other regions (Figure 5.12) while in male, the rSPG drives other regions (Figure 5.13). As mentioned above, lAG has been shown to be related to mental arithmetic [307] and parietal lobe [255][299] could serve broadly in associative processing [314][315]. This result may reflect the cognitive bias between genders.

In conclusion, our study demonstrates that neurofeedback could potentially be used to mimic effects seen in brain stimulation techniques such as tDCS in facilitating insight problem solving and enhancing human creativity. This provides a potential framework for cross-pollination between brain stimulation and neurofeedback paradigms.

Chapter 6

Conclusion and Future Work

6.1 Conclusion

This dissertation aims to propose novel signal processing methods and experimental paradigms with fMRI applications, which devotes to the strategies of decoding brain signals and states.

The conclusions are summarized as follows:

Study 1 and study 2: Most rs-fMRI connectivity analyses were conventionally applied to the raw BOLD signal, which ignored the confounding effect raised from the varied HRF. Previous discussions proposed HRF deconvolution methods to acquire neural-space signal and concluded that it is better to use neural-space signal for inferring causality on hidden neural activity[53][54][55][56]. In the light of these works, we continued the discussion into rs-fMRI connectivity analysis. We hypothesized that the systematic differences in the shape of the HRF could be examined between these pathological populations and healthy controls, and the varied HRF would contribute to the differences in estimating functional connectivity in the BOLD space as compared to the latent neural space. Since the aberrant non-neural factors that would control the HRF shape was well-stablished in ASD [47], SZ [48][49][50][51][52] and BP [53][54][55],

we verified the proposed hypotheses on the three pathological populations. By applying a novel deconvolution method which copes with varied HRF, we acquired the voxel specific HRF and latent neural event in these pathological populations and healthy control group. In study 1, we identified the brain regions which had systematic differences in HRF shape between these ASD and control groups. Specifically, we detected a cluster in precuneus exhibited aberrations in all HRF parameters. Further, we examined and compared the precuneus-seed-based functional connectivity differences between ASD and controls in BOLD space as well as latent neural space and the fMRI data processed without deconvolution failed to detect group differences in connectivity. In study 2, we observed brain regions showed differences in HRF shape between SZ, BP and control subjects, and detected a cluster within the mediodorsal, habenular and central lateral nuclei of the thalamus that exhibited pairwise altered HRF shape between the three populations. We evaluated the thalamic seed-based functional connectivity maps in BOLD space as well as latent neural space. In both studies, our results indicated that the pairwise functional connectivity differences between the groups were inferred significantly different in BOLD space and latent neural space. Moreover, we performed two-way ANOVA analyses in study 1 and 2, and the interaction between group and deconvolution factors was demonstrated in estimated regions. This shows that functional connectivity group differences in these regions would be inferred differently in DC and NDC datasets.

Together, our results demonstrated that the possible confounds introduced by the variable HRF in identified functional networks in pathological populations, especially in the populations

that share overlapped pathology in the neurotransmitters which also control HRF shape. We reported that raw fMRI data might have failed to detect group differences in rs-fMRI connectivity analysis and emphasized the importance of performing HRF deconvolution method in rs-fMRI connectivity analysis. Moreover, our results are relevant for the understanding of hemodynamic and neurochemical aberrations in ASD, SZ, and BP.

Study 3: Present researchers have demonstrated that the activity in right-sided rATL is crucial in generating "Aha!" experience in insight problem solving [255]. However, the elaborated mechanism remains unclear. Our work aimed to find a way to approach insight with novel neuroimaging techniques and experimental paradigms. By introducing rt-fMRI neurofeedback technology, we mimicked the facilitated effect of tDSC [66] on solving nine-dot puzzle. Consequently, the increased number of subjects who solved the problem is in line with the stimulus effect of tDSC. Also, the successful solved group exhibited better capability in self-regulation the brain activity in rATL. Since the enhancement of activity in a single targeted region could mediate its connection with other regions, we further investigated the underlying neuronal connectivity. Our results demonstrated that rt-fMRI neurofeedback not only facilitated the subjects to up-regulate the activation of targeted brain region (rATL in our case), but also to altered brain connectivity associated with the targeted region [34][35]. Our results indicated that the up-regulation of activity in rATL are likely to mitigate the top-down modulation of temporal regions by frontal regions imposing cognitive biases [317][318][319], which inhibits creativity and insight problem solving.

To sum it up, we characterized the underlying directional brain networks in these groups of participants in order to understand the role of top-down inputs into the rATL in enhancing or suppressing creative insight. We have demonstrated that insight solutions are indeed associated with a discrete, distinct pattern of neural activity, supporting unique cognitive processes. Moreover, our study demonstrated that neurofeedback could potentially be used to mimic effects seen in brain stimulation techniques such as tDCS in facilitating insight problem solving and enhancing human creativity. This study provided a potential framework for cross-pollination between brain stimulation and neurofeedback paradigms.

6.2 Limitations and Future work

We here present some limitations of this dissertation and point towards future directions which could address those limitations.

In study 1 and study 2, we only estimated the effect of HRF variability in functional connectivity by using the estimated seeds. However, one could investigate the effect of voxel-wise HRF variability on voxel-wise functional connectivity differences between controls and pathologic populations at the whole brain level. Second, we have discussed various neurochemical alterations in pathologic populations and how they could have influenced the shape of the HRF. These inferences are indirect at best, since we did not directly measure the concentration of those neurochemicals. Such an endeavor, using noninvasive in vivo methods, such as magnetic resonance spectroscopy in humans as well as invasive methods in animal models could provide evidence that is more direct and further validate our observations.

In study 3, we mimicked the facilitated effect of tDSC over rATL on solving nine-dot puzzle [66]. However, in Chi's research [66], they investigated the stimulation targeted on rATL, the inhibition targeted on lATL and the integrated effect of both. The further study should also investigate the self-generated inhibition over lATL and integrated effect based on rt-fMRI technology.

Bibliography

[1] S. Ogawa, T. M. Lee, A. S. Nayak, and P. Glynn, “Oxygenation-sensitive contrast in magnetic resonance image of rodent brain at high magnetic fields,” *Magn. Reson. Med.*, vol. 14, no. 1, pp. 68–78, 1990.

[2] R. B. Buxton, E. C. Wong, and L. R. Frank, “Dynamics of blood flow and oxygenation changes during brain activation: the balloon model.,” *Magn. Reson. Med.*, vol. 39, no. 6, pp. 855–864, 1998.

[3] R. D. Hoge, J. Atkinson, B. Gill, G. R. Crelier, S. Marrett, and G. B. Pike, “Linear coupling between cerebral blood flow and oxygen consumption in activated human cortex.,” *Proc. Natl. Acad. Sci. U. S. A.*, vol. 96, no. 8, pp. 9403–9408, 1999.

[4] D. Attwell and C. Iadecola, “The neural basis of functional brain imaging signals,” *Trends Neurosci.*, vol. 25, no. 12, pp. 621–625, 2002.

[5] N. R. Sibson, A. Dhankhar, G. F. Mason, D. L. Rothman, K. L. Behar, and R. G. Shulman, “Stoichiometric coupling of brain glucose metabolism and glutamatergic neuronal activity,” *Neurobiology*, vol. 95, no. January, pp. 316–321, 1998.

[6] B. A. Macvicar and E. A. Newman, “Astrocyte regulation of blood flow in the brain,” *Cold Spring Harb. Perspect. Biol.*, vol. 7, no. 5, pp. 1–15, 2015.

[7] A. Kocharyan, P. Fernandes, X.-K. Tong, E. Vaucher, and E. Hamel, “Specific subtypes of cortical GABA interneurons contribute to the neurovascular coupling response to basal forebrain stimulation.,” *J. Cereb. Blood Flow Metab.*, vol. 28, pp. 221–231, 2008.

[8] Z. Cohen, G. Bonvento, P. Lacombe, and E. Hamel, “Serotonin in the regulation of brain microcirculation.,” *Prog. Neurobiol.*, vol. 50, no. 4, pp. 335–62, Nov. 1996.

[9] D. Attwell, A. M. Buchan, S. Charpak, M. Lauritzen, B. A. MacVicar, and E. A. Newman, “Glial and neuronal control of brain blood flow,” *Nature*, vol. 468, no. 7321, pp. 232–243, 2010.

[10] E. T. Ahrens, J. Blumenthal, R. E. Jacobs, and J. N. Giedd, *Brain Mapping: The Systems*. 2000.

[11] D. Chien, K. K. Kwong, D. R. Gress, F. S. Buonanno, R. B. Buxton, and B. R. Rosen, “MR diffusion imaging of cerebral infarction in humans.,” *AJNR. Am. J. Neuroradiol.*, vol. 13, no. 4, pp. 1097-102–5, 1992.

[12] S. A. Huettel, A. W. Song, and G. McCarthy, *Functional magnetic resonance imaging*, Sinauer Associates, Sunderland, 2004.

[13] N. K. Logothetis, J. Pauls, M. Augath, T. Trinath, and A. Oeltermann, “Neurophysiological investigation of the basis of the fMRI signal,” *Nature*, vol. 412, no. 6843, pp. 150–157, 2001.

[14] D. D. Langleben and J. C. Moriarty, “Using Brain Imaging for Lie Detection: Where Science, Law and Research Policy Collide,” *Psychol. Public Policy. Law*, vol. 19, no. 2, pp. 222–234, 2013.

[15] M. S. Gazzaniga, R. B. Ivry, and G. R. Mangun, “Cognitive Neuroscience: The Biology of the Mind,” *The Quarterly Review of Biology*, vol. 84, no. 2. pp. 196–197, 2009.

[16] K. Murphy, R. M. Birn, and P. A. Bandettini, “Resting-state fMRI confounds and cleanup,” *Neuroimage*, vol. 80, pp. 349–359, 2013.

[17] M. D. Fox and M. E. Raichle, “Spontaneous fluctuations in brain activity observed with functional magnetic resonance

imaging," *Nat. Rev. Neurosci.*, vol. 8, no. 9, pp. 700–711, 2007.

[18] C. Iadecola, "Intrinsic signals and functional brain mapping: caution, blood vessels at work.," *Cereb. Cortex*, vol. 12, no. 3, pp. 223–4, 2002.

[19] G. S. Berns, A. W. Song, and H. Mao, "Continuous functional magnetic resonance imaging reveals dynamic nonlinearities of 'dose-response' curves for finger opposition," *J. Neurosci.*, vol. 19, no. 14, p. RC17, 1999.

[20] G. H. Glover, "Deconvolution of impulse response in event-related BOLD fMRI.," *Neuroimage*, vol. 9, no. 4, pp. 416–429, 1999.

[21] G. M. Boynton, S. A. Engel, G. H. Glover, and D. J. Heeger, "Linear systems analysis of functional magnetic resonance imaging in human V1.," *J. Neurosci.*, vol. 16, no. 13, pp. 4207–4221, 1996.

[22] D. E. Glaser, K. J. Friston, A. Mechelli, R. Turner, and C. J. Price, Haemodynamic modelling, In R.S.J. Frackowiak, K.J. Friston, C. Frith, R. Dolan, and J.C. Mazziotta, editors, *Human Brain Function*, Elsevier Press, London, 2003.

[23] K. J. Friston, C. D. Frith, R. S. J. Frackowiak, and R. Turner, "Characterizing Dynamic Brain Responses with fMRI: A Multivariate Approach," *Neuroimage*, vol. 2, no. 2, pp. 166–172, 1995.

[24] L. D. Lewis, K. Setsompop, B. R. Rosen, and J. R. Polimeni, "Fast fMRI can detect oscillatory neural activity in humans," *Proc. Natl. Acad. Sci.*, vol. 113, no. 43, pp. E6679–E6685, 2016.

[25] A. M. Dale, "Optimal experimental design for event-related fMRI," *Hum. Brain Mapp.*, 1999, vol. 8, no. 2–3, pp. 109–114.

[26] M. A. Lindquist and T. D. Wager, "Validity and power in hemodynamic response modeling: A comparison study and a new approach," *Hum. Brain Mapp.*, vol. 28, no. 8, pp. 764–784, 2007.

[27] B. B. Biswal, "Resting state fMRI: A personal history," *Neuroimage*, vol. 62, no. 2, pp. 938–944, 2012.

[28] R. L. Buckner, F. M. Krienen, and B. T. Yeo, "Opportunities and limitations of intrinsic functional connectivity MRI," *Nat. Neurosci.*, vol. 16, no. 7, pp. 832–837, 2013.

[29] D. A. Leopold and N. K. Logothetis, "Spatial patterns of spontaneous local field activity in the monkey visual cortex," *Rev Neurosci*, vol. 14, no. 1–2, pp. 195–205, 2003.

[30] B. Biswal, F. Z. Yetkin, V. M. Haughton, and J. S. Hyde, "Functional Connectivity in the Motor Cortex of Resting," *Brain*, vol. 34, pp. 537–541, 1995.

[31] G. L. Gerstein and D. H. Perkel, "Simultaneously Recorded Trains of Action Potentials: Analysis and Functional Interpretation," *Science*, vol. 164, no. 3881, pp. 828–830, 1969.

[32] D. M. Cole, S. M. Smith, and C. F. Beckmann, "Advances and pitfalls in the analysis and interpretation of resting-state FMRI data.," *Front. Syst. Neurosci.*, vol. 4, no. 4, p. 8, 2010.

[33] C. Rosazza and L. Minati, "Resting-state brain networks: Literature review and clinical applications," *Neurol. Sci.*, vol. 32, no. 5, pp. 773–785, 2011.

[34] J. Sulzer, S. Haller, F. Scharnowski, N. Weiskopf, N. Birbaumer, M. L. Blefari, A. B. Bruehl, L. G. Cohen, R. C. deCharms, R. Gassert, R. Goebel, U. Herwig, S. LaConte, D. Linden, A. Luft, E. Seifritz, and R. Sitaram, "Real-time fMRI neurofeedback: Progress and challenges," *Neuroimage*, vol. 76, pp. 386–399, 2013.

[35] J. T. Voyvodic, "Real-time fMRI paradigm control, physiology, and behavior combined with near real-time statistical analysis," *Neuroimage*, vol. 10, no. 2, pp. 91–106, 1999.

[36] R. C. deCharms, F. Maeda, G. H. Glover, D. Ludlow, J. M. Pauly, D. Soneji, J. D. E. Gabrieli, and S. C. Mackey, "Control over brain activation and pain learned by using real-time functional MRI.," *Proc. Natl. Acad. Sci. U. S. A.*, vol. 102, no.

51, pp. 18626–31, Dec. 2005.

[37] S. Posse, D. Fitzgerald, K. Gao, U. Habel, D. Rosenberg, G. J. Moore, and F. Schneider, “Real-time fMRI of temporolimbic regions detects amygdala activation during single-trial self-induced sadness,” *Neuroimage*, vol. 18, no. 3, pp. 760–768, 2003.

[38] J. W. Schooler, S. Ohlsson, and K. Brooks, “Thoughts Beyond Words: When Language Overshadows Insight,” *J. Exp. Psychol. Gen.*, vol. 122, no. 2, pp. 166–183, 1993.

[39] J. Metcalfe, “Premonitions of insight predict impending error.,” *J. Exp. Psychol. Learn. Mem. Cogn.*, vol. 12, no. 4, pp. 623–634, 1986.

[40] J. M. Chein, R. W. Weisberg, N. L. Streeter, and S. Kwok, “Working memory and insight in the nine-dot problem.,” *Mem. Cognit.*, vol. 38, no. 7, pp. 883–892, 2010.

[41] D. D. Cox and R. L. Savoy, “Functional magnetic resonance imaging (fMRI)‘brain reading’: detecting and classifying distributed patterns of fMRI activity in human visual cortex,” *Neuroimage*, vol. 19, no. 2, pp. 261–270, 2003.

[42] K. N. Kay, T. Naselaris, R. J. Prenger, and J. L. Gallant, “Identifying natural images from human brain activity,” *Nature*, vol. 452, no. 7185, pp. 352–355, 2008.

[43] M. Greicius, “Resting-state functional connectivity in neuropsychiatric disorders.,” *Curr. Opin. Neurol.*, vol. 21, no. 4, pp. 424–30, 2008.

[44] X. J. Chai, S. Whitfield-Gabrieli, A. K. Shinn, J. D. E. Gabrieli, A. Nieto Castañón, J. M. McCarthy, B. M. Cohen, and D. Ongür, “Abnormal medial prefrontal cortex resting-state connectivity in bipolar disorder and schizophrenia,” *Neuropsychopharmacol. Off. Publ. Am. Coll. Neuropsychopharmacol.*, vol. 36, no. 2011, pp. 2009–2017, 2011.

[45] V. L. Cherkassky, R. K. Kana, T. A. Keller, and M. A. Just, “Functional connectivity in a baseline resting-state network in autism,” *Neuroreport*, vol. 17, no. 16, pp. 1687–1690, 2006.

[46] S. Ogawa and T. M. Lee, “Magnetic resonance imaging of blood vessels at high fields: in vivo and in vitro measurements and image simulation.,” *Magn. Reson. Med.*, vol. 16, no. 1, pp. 9–18, 1990.

[47] D. A. Handwerker, J. M. Ollinger, and M. D’Esposito, “Variation of BOLD hemodynamic responses across subjects and brain regions and their effects on statistical analyses,” *Neuroimage*, vol. 21, no. 4, pp. 1639–1651, 2004.

[48] D. A. Handwerker, J. Gonzalez-Castillo, M. D’Esposito, and P. A. Bandettini, “The continuing challenge of understanding and modeling hemodynamic variation in fMRI,” *NeuroImage*, vol. 62, no. 2. pp. 1017–1023, 2012.

[49] Z. Y. Shan, A. A. E. Vinkhuyzen, P. M. Thompson, K. L. McMahon, G. A. M. Blokland, G. I. De Zubicaray, V. Calhoun, N. G. Martin, P. M. Visscher, M. J. Wright, and D. C. Reutens, “Genes influence the amplitude and timing of brain hemodynamic responses,” *Neuroimage*, vol. 124, pp. 663–671, 2016.

[50] R. B. Buxton, “Introduction to Functional Magnetic Resonance Imaging: Principles and Techniques,” *Energy*, vol. 24, no. 2, p. xi, 523 , 2002.

[51] J. M. Levin, M. H. Ross, J. H. Mendelson, M. J. Kaufman, N. Lange, L. C. Maas, N. K. Mello, B. M. Cohen, and P. F. Renshaw, “Reduction in BOLD fMRI response to primary visual stimulation following alcohol ingestion.,” *Psychiatry Res.*, vol. 82, no. 3, pp. 135–46, 1998.

[52] M. D. Noseworthy, J. Alfonsi, and S. Bells, “Attenuation of brain BOLD response following lipid ingestion,” *Hum. Brain Mapp.*, vol. 20, no. 2, pp. 116–121, 2003.

[53] O. David, I. Guillemain, S. Saillet, S. Reyt, C. Deransart, C. Segebarth, and A. Depaulis, “Identifying Neural Drivers with Functional MRI: An Electrophysiological Validation,” *PLoS Biol.*, vol. 6, no. 12, p. e315, 2008.

[54] P. A. Valdes-Sosa, A. Roebroeck, J. Daunizeau, and K. Friston, “Effective connectivity: Influence, causality and biophysical modeling,” *NeuroImage*, vol. 58, no. 2. pp. 339–361, 2011.

[55] S. Ryali, K. Supekar, T. Chen, and V. Menon, “Multivariate dynamical systems models for estimating causal interactions in fMRI,” *Neuroimage*, vol. 54, no. 2, pp. 807–823, 2011.

[56] S. Kadkhodaeian Bakhtiari and G. A. Hossein-Zadeh, “Subspace-based Identification Algorithm for characterizing causal networks in resting brain,” *Neuroimage*, vol. 60, no. 2, pp. 1236–1249, 2012.

[57] C. Reynell and J. J. Harris, “The BOLD signal and neurovascular coupling in autism,” *Dev. Cogn. Neurosci.*, vol. 6, pp. 72–79, 2013.

[58] J. M. McNally, R. W. McCarley, and R. E. Brown, “Impaired GABAergic neurotransmission in schizophrenia underlies impairments in cortical gamma band oscillations.,” *Current psychiatry reports*, vol. 15, no. 3. p. 346, 2013.

[59] C. Chiapponi, F. Piras, F. Piras, C. Caltagirone, and G. Spalletta, “GABA system in schizophrenia and mood disorders: A mini review on third-generation imaging studies,” *Frontiers in Psychiatry*, vol. 7, no. APR. 2016.

[60] X. Y. Zhang, D. F. Zhou, Y. C. Shen, P. Y. Zhang, W. F. Zhang, J. Liang, D. C. Chen, M. H. Xiu, T. A. Kosten, and T. R. Kosten, “Effects of risperidone and haloperidol on superoxide dismutase and nitric oxide in schizophrenia,” *Neuropharmacology*, vol. 62, no. 5–6, pp. 1928–1934, 2012.

[61] N. Igbal and H. M. Van Praag, “The role of serotonin in schizophrenia,” *Eur. Neuropsychopharmacol.*, vol. 5, no. SUPPL. 1, pp. 11–23, 1995.

[62] G. Tsai and J. T. Coyle, “Glutamatergic mechanism in schizophrenia,” *Annu. Rev. Pharmacol. Toxicol*, vol. 42, pp. 165–79, 2002.

[63] R. T. De Sousa, M. V Zanetti, G. F. Busatto, M. G. Mouro, C. a Zarate, W. F. Gattaz, E. M. Higa, and R. Machado-Vieira, “Lithium increases nitric oxide levels in subjects with bipolar disorder during depressive episodes.,” *J. Psychiatr. Res.*, vol. 55, pp. 96–100, 2014.

[64] T. Mahmood and T. Silverstone, “Serotonin and bipolar disorder.,” *J. Affect. Disord.*, vol. 66, no. 1, pp. 1–11, 2001.

[65] H. H. Schiffer, “Glutamate receptor genes: susceptibility factors in schizophrenia and depressive disorders?,” *Mol Neurobiol*, vol. 25, no. 2, pp. 191–212, 2002.

[66] R. P. Chi and A. W. Snyder, “Brain stimulation enables the solution of an inherently difficult problem,” *Neurosci. Lett.*, vol. 515, no. 2, pp. 121–124, 2012.

[67] K. J. Friston, A. P. Holmes, K. J. Worsley, J. P. Poline, C. D. Frith, and R. S. J. Frackowia, “Statistical parametric maps in functional imaging: A general linear approach,” *Hum. Brain Mapp.*, vol. 2, no. 4, pp. 189–210, 1994.

[68] Y. Benjamini and Y. Hochberg, “Controlling the false discovery rate: a practical and powerful approach to multiple testing,” *J. R. Stat. Soc. B*, vol. 57, no. 1, pp. 289–300, 1995.

[69] J. P. Shaffer, “Multiple Hypothesis Testing,” *Annu. Rev. Psychol.*, vol. 46, no. 1, pp. 561–584, 1995.

[70] C. R. Genovese, N. A. Lazar, and T. Nichols, “Thresholding of statistical maps in functional neuroimaging using the false discovery rate,” *Neuroimage*, vol. 15, no. 4, pp. 870–878, 2002.

[71] J. T. Webb, M. A. Ferguson, J. A. Nielsen, and J. S. Anderson, “BOLD Granger causality reflects vascular anatomy.,” *PLoS One*, vol. 8, no. 12, p. e84279, 2013.

[72] M. Havlicek, K. J. Friston, J. Jan, M. Brazdil, and V. D. Calhoun, “Dynamic modeling of neuronal responses in fMRI using cubature Kalman filtering,” *Neuroimage*, vol. 56, no. 4, pp. 2109–2128, 2011.

[73] S. Haykin, “Cubature Kalman Filters,” *IEEE Trans. Automat Contr.*, vol. 54, no. 6, pp. 1254-1269, 2009.

[74] J. C. Jimenez, I. Shoji, and T. Ozaki, "Simulation of Stochastic Differential Equations Through the Local Linearization Method . A Comparative Study," *J. Stat. Phys.*, vol. 94, pp. 4–6, 1999.

[75] G. R. Wu, W. Liao, S. Stramaglia, J.-R. J. Ding, H. Chen, and D. Marinazzo, "A blind deconvolution approach to recover effective connectivity brain networks from resting state fMRI data," *Med. Image Anal.*, vol. 17, no. 3, pp. 365–74, 2013

[76] K. Pearson, "Note on Regression and Inheritance in the Case of Two Parents," *Proc. R. Soc. London*, vol. 58, pp. 240–242, 2006.

[77] R. A. Fischer, "On a distribution yielding the error functions of several well known statistics," *Proceedings of the international congress of mathematics*, vol. 2. pp. 493–502, 1924.

[78] C. W. J. Granger, "Investigating Causal Relations by Econometric Models and Cross-spectral Methods," *Econometrica*, vol. 37, no. 3, pp. 424–438, 1969.

[79] C. W. J. Granger, "Testing for causality. A personal viewpoint," *J. Econ. Dyn. Control*, vol. 2, no. C, pp. 329–352, 1980.

[80] M. Eichler, "Causal inference in time series analysis," in C. Berzuini, P. Dawid, L. Bernardinell, editors, *Causality: Statistical Perspectives and Applications*, John Wiley & Sons, New York, 2012.

[81] B. M. Hampstead, M. Khoshnoodi, W. Yan, G. Deshpande, and K. Sathian, "Patterns of effective connectivity during memory encoding and retrieval differ between patients with mild cognitive impairment and healthy older adults," *Neuroimage*, vol. 124, pp. 997–1008, 2016.

[82] C. Büchel and K. J. Friston, "Dynamic changes in effective connectivity characterized by variable parameter regression and Kalman filtering," in *Human Brain Mapping*, 1998, vol. 6, no. 5–6, pp. 403–408.

[83] S. Lacey, R. Stilla, G. Deshpande, S. Zhao, C. Stephens, K. McCormick, D. Kemmerer, and K. Sathian, "Engagement of the left extrastriate body area during body-part metaphor comprehension," *Brain Lang.*, vol. 166, pp. 1–18, 2017.

[84] B. Biswal, F. Z. Yetkin, V. M. Haughton, and J. S. Hyde, "Functional connectivity in the motor cortex of resting human brain using echo-planar MRI.," *Magn. Reson. Med.*, vol. 34, no. 4, pp. 537–541, 1995.

[85] D. Cordes, V. M. Haughton, K. Arfanakis, J. D. Carew, P. A. Turski, C. H. Moritz, M. A. Quigley, and M. E. Meyerand, "Frequencies contributing to functional connectivity in the cerebral cortex in 'resting-state' data," *Am. J. Neuroradiol.*, vol. 22, no. 7, pp. 1326–1333, 2001.

[86] J. A. Nielsen, B. A. Zielinski, P. Fletcher, A. L. Alexander, N. Lange, E. D. Bigler, J. E. Lainhart, and J. S. Anderson, "Abnormal lateralization of functional connectivity between language and default mode regions in autism," *Mol. Autism*, vol. 5, no. 1, p. 8, 2014.

[87] W. Cheng, E. T. Rolls, H. Gu, J. Zhang, and J. Feng, "Autism: reduced connectivity between cortical areas involved in face expression, theory of mind, and the sense of self," *Brain*, vol. 138, no. 5, pp.1382-1393, 2015.

[88] J. A Nielsen, B. A Zielinski, P. Fletcher, A. L. Alexander, N. Lange, E. D. Bigler, J. E. Lainhart, and J. S. Anderson, "Deriving reproducible biomarkers from multi-site resting-state data: An Autism-based example," Neuroimage, vol. 147, pp. 736–745, 2016

[89] K. Alaerts, D. G. Woolley, J. Steyaert, A. Di Martino, S. P. Swinnen, and N. Wenderoth, "Underconnectivity of the superior temporal sulcus predicts emotion recognition deficits in autism," *Soc. Cogn. Affect. Neurosci.*, vol. 9, no. 10, pp. 1589–1600, 2013.

[90] C. P. Chen, C. L. Keown, A. Jahedi, A. Nair, M. E. Pflieger, B. A. Bailey, and R. A. Müller, "Diagnostic classification of intrinsic functional connectivity highlights somatosensory, default mode, and visual regions in autism.," *NeuroImage. Clin.*, vol. 8, pp. 238–45, 2015.

[91] G. K. Aguirre, E. Zarahn, and M. D'esposito, "The variability of human, BOLD hemodynamic responses.," *Neuroimage*, vol. 8, no. 4, pp. 360–9, 1998.

[92] J. V Duarte, J. M. Pereira, B. Quendera, M. Raimundo, C. Moreno, L. Gomes, F. Carrilho, and M. Castelo-Branco, "Early disrupted neurovascular coupling and changed event level hemodynamic response function in type 2 diabetes: an fMRI study," *J. Cereb. Blood Flow Metab.*, vol. 35, no. 10, pp. 1671–80, 2015.

[93] D. Rangaprakash, G. Deshpande, T. A. Daniel, A. M. Goodman, J. L. Robinson, N. Salibi, J. S. Katz, T. S. Denney, M. N. Dretsch, "Compromised hippocampus-striatum pathway as a potential imaging biomarker of mild traumatic brain injury and post-traumatic stress disorder," Human Brain Mapping, 2017 (in press).

[94] D. R. Gitelman, W. D. Penny, J. Ashburner, and K. J. Friston, "Modeling regional and psychophysiologic interactions in fMRI: the importance of hemodynamic deconvolution.," *Neuroimage*, vol. 19, no. 1, pp. 200–207, 2003.

[95] K. M. Aquino, P. A. Robinson, M. M. Schira, and M. Breakspear, "Deconvolution of neural dynamics from fMRI data using a spatiotemporal hemodynamic response function," *Neuroimage*, vol. 94, pp. 203–215, 2014.

[96] G. R. Wu and D. Marinazzo, "Point-Process Deconvolution of fMRI BOLD Signal Reveals Effective Connectivity Alterations in Chronic Pain Patients," *Brain Topogr.*, vol. 28, no. 4, pp. 541–547, 2014.

[97] S. H. Fatemi, T. J. Reutiman, T. D. Folsom, and P. D. Thuras, "GABAA receptor downregulation in brains of subjects with autism," *J. Autism Dev. Disord.*, vol. 39, no. 2, pp. 223–230, 2009.

[98] A. Di Martino, C. G. Yan, Q. Li, E. Denio, F. X. Castellanos, K. Alaerts, J. S. Anderson, M. Assaf, S. Y. Bookheimer, M. Dapretto, B. Deen, S. Delmonte, I. Dinstein, B. Ertl-Wagner, D. a Fair, L. Gallagher, D. P. Kennedy, C. L. Keown, C. Keysers, J. E. Lainhart, C. Lord, B. Luna, V. Menon, N. J. Minshew, C. S. Monk, S. Mueller, R. Müller, M. B. Nebel, J. T. Nigg, K. O'Hearn, K. A. Pelphrey, S. J. Peltier, J. D. Rudie, S. Sunaert, M. Thioux, J. M. Tyszka, L. Q. Uddin, J. S. Verhoeven, N. Wenderoth, J. L. Wiggins, S. H. Mostofsky, and M. P. Milham, "The autism brain imaging data exchange: towards a large-scale evaluation of the intrinsic brain architecture in autism.," *Mol. Psychiatry*, vol. 19, no. 6, pp. 659–67, 2014.

[99] Y. Chao-Gan and Z. Yu-Feng, "DPARSF: A MATLAB Toolbox for 'Pipeline' Data Analysis of Resting-State fMRI.," *Front. Syst. Neurosci.*, vol. 4, no. 5, p. 13, 2010.

[100] W. Penny and L. Harrison. Multivariate autoregressive models. In K. Friston, J. Ashburner, S. Kiebel, T. Nichols, and W. Penny, editors, *Statistical Parametric Mapping: The analysis of functional brain images*. Elsevier, London, 2006.

[101] X. W. Song, Z. Y. Dong, X. Y. Long, S. F. Li, X. N. Zuo, C. Z. Zhu, Y. He, C. G. Yan, and Y. F. Zang, "REST: A Toolkit for Resting-State Functional Magnetic Resonance Imaging Data Processing," *PLoS ONE*, vol. 6, no. 9. p. e25031, 2011.

[102] K. J. Friston, S. Williams, R. Howard, R. S. Frackowiak, and R. Turner, "Movement-related effects in fMRI time-series.," *Magn. Reson. Med.*, vol. 35, no. 3, pp. 346–355, 1996.

[103] E. Tagliazucchi, P. Balenzuela, D. Fraiman, and D. R. Chialvo, "Criticality in large-scale brain fmri dynamics unveiled by a novel point process analysis," *Front. Physiol.*, vol. 3, 2012.

[104] W. H. Press, S. A. Teukolsky, W. T. Vetterling, and B. P. Flannery, *Numerical recipes in C (2nd ed.): the art of scientific computing*, vol. 29, no. 4. 1992.

[105] M. J. Lowe, B. J. Mock, and J. A. Sorenson, "Functional Connectivity in Single and Multislice Echoplanar Imaging Using Resting-State Fluctuations," *Neuroimage*, vol. 7, no. 2, pp. 119–132, 1998.

[106] A. P. Holmes and K. J. Friston, "Generalisability, random effects and population inference," *Neuroimage*, vol. 7, p. S754, 1998.

[107] G. G. Brown, L. T. Eyler Zorrilla, B. Georgy, S. S. Kindermann, E. C. Wong, and R. B. Buxton, "BOLD and perfusion response to finger-thumb apposition after acetazolamide administration: differential relationship to global perfusion.," *J. Cereb. Blood Flow Metab.*, vol. 23, no. 7, pp. 829–37, 2003.

[108] G. Buzsáki, K. Kaila, and M. Raichle, "Inhibition and Brain Work," *Neuron*, vol. 56, no. 5. pp. 771–783, 2007.

[109] D. Lozano-Soldevilla, N. Ter Huurne, R. Cools, and O. Jensen, "GABAergic modulation of visual gamma and alpha oscillations and its consequences for working memory performance," *Curr. Biol.*, vol. 24, no. 24, pp. 2878–2887, 2014.

[110] S. D. Muthukumaraswamy, C. J. Evans, R. A. E. Edden, R. G. Wise, and K. D. Singh, "Individual variability in the shape and amplitude of the BOLD-HRF correlates with endogenous GABAergic inhibition.," *Hum. Brain Mapp.*, vol. 33, no. 2, pp. 455–65, Feb. 2012.

[111] D. W. Busija, F. Bari, F. Domoki, and T. Louis, "Mechanisms involved in the cerebrovascular dilator effects of N-methyl-d-aspartate in cerebral cortex.," *Brain Res. Rev.*, vol. 56, no. 1, pp. 89–100, 2007.

[112] G. Northoff, M. Walter, R. F. Schulte, J. Beck, U. Dydak, A. Henning, H. Boeker, S. Grimm, and P. Boesiger, "GABA concentrations in the human anterior cingulate cortex predict negative BOLD responses in fMRI," *Nat. Neurosci.*, vol. 10, no. 12, pp. 1515–1517, 2007.

[113] S. D. Muthukumaraswamy, R. A. E. Edden, D. K. Jones, J. B. Swettenham, and K. D. Singh, "Resting GABA concentration predicts peak gamma frequency and fMRI amplitude in response to visual stimulation in humans.," *Proc. Natl. Acad. Sci. U. S. A.*, vol. 106, no. 20, pp. 8356–8361, 2009.

[114] M. Harada, M. M. Taki, A. Nose, H. Kubo, K. Mori, H. Nishitani, and T. Matsuda, "Non-invasive evaluation of the GABAergic/glutamatergic system in autistic patients observed by MEGA-editing proton MR spectroscopy using a clinical 3 tesla instrument.," *J. Autism Dev. Disord.*, vol. 41, no. 4, pp. 447–54, 2011.

[115] S. H. Fatemi, T. J. Reutiman, T. D. Folsom, O. G. Rustan, R. J. Rooney, and P. D. Thuras, "Downregulation of GABA receptor protein subunits α6, β2, δ, ε, γ2, θ, and ρ2 in superior frontal cortex of subjects with autism," J. Autism Dev. Disord., vol. 44, no. 8, pp. 1833–1845, 2014.

[116] N. Hadjikhani, N. R. Zürcher, O. Rogier, T. Ruest, L. Hippolyte, Y. Ben-Ari, and E. Lemonnier, "Improving emotional face perception in autism with diuretic bumetanide: A proof-of-concept behavioral and functional brain imaging pilot study," *Autism*, vol. 19, no. 2, p. 1362361313514141, 2013.

[117] S. D. Muthukumaraswamy, C. J. Evans, R. A. E. Edden, R. G. Wise, and K. D. Singh, "Individual variability in the shape and amplitude of the BOLD-HRF correlates with endogenous GABAergic inhibition.," *Hum. Brain Mapp.*, vol. 33, no. 2, pp. 455–65, 2012.

[118] G. Cellot and E. Cherubini, "GABAergic signaling as therapeutic target for autism spectrum disorders.," *Front. Pediatr.*, vol. 2, p. 70, 2014.

[119] V. S. Fénelon and A. E. Herbison, "In vivo regulation of specific GABAa receptor subunit messenger RNAs by increased GABA concentrations in rat brain," *Neuroscience*, vol. 71, no. 3, pp. 661–670, 1996.

[120] S. Ferré and F. Artigas, "Dopamine D2 Receptor-Mediated Regulation of Serotonin Extracellular Concentration in the Dorsal Raphe Nucleus of Freely Moving Rats.," J. Neurochem., vol. 61, no. 2, pp. 772–775, 1993.

[121] R. W. Fuller, "Uptake inhibitors increase extracellular serotonin concentration measured by brain microdialysis," *Life Sciences*, vol. 55, no. 3. pp. 163–167, 1994.

[122] C. E. Beyer and T. I. F. H. Cremers, "Do selective serotonin reuptake inhibitors acutely increase frontal cortex levels of serotonin?," *Eur. J. Pharmacol.*, vol. 580, no. 3, pp. 350–354, 2008.

[123] E. R. Ritvo, A. Yuwiler, E. Geller, E. M. Ornitz, K. Saeger, and S. Plotkin, "Increased Blood Serotonin and Platelets in Early Infantile Autism," *Arch. Gen. Psychiat.*, vol. 23, pp. 566–572, 1970.

[124] C. Pagan, R. Delorme, J. Callebert, H. Goubran-Botros, F. Amsellem, X. Drouot, C. Boudebesse, K. Le Dudal, N. Ngo-Nguyen, H. Laouamri, C. Gillberg, M. Leboyer, T. Bourgeron, and J.-M. Launay, "The serotonin-N-acetylserotonin-melatonin pathway as a biomarker for autism spectrum disorders.," *Transl. Psychiatry*, vol. 4, no. 11, p. e479, 2014.

[125] C. H. Huang and S. L. Santangelo, "Autism and serotonin transporter gene polymorphisms: a systematic review and meta-analysis," *Am J Med Genet B Neuropsychiatr Genet*, vol. 147B, no. 6, pp. 903–913, 2008.

[126] J. S. Sutcliffe, R. J. Delahanty, H. C. Prasad, J. L. McCauley, Q. Han, L. Jiang, C. Li, S. E. Folstein, and R. D. Blakely, "Allelic heterogeneity at the serotonin transporter locus (SLC6A4) confers susceptibility to autism and rigid-compulsive behaviors," *Am J Hum Genet*, vol. 77, no. 2, pp. 265–279, 2005.

[127] S. R. Chandana, M. E. Behen, C. Juhász, O. Muzik, R. D. Rothermel, T. J. Mangner, P. K. Chakraborty, H. T. Chugani, and D. C. Chugani, "Significance of abnormalities in developmental trajectory and asymmetry of cortical serotonin synthesis in autism," *Int. J. Dev. Neurosci.*, vol. 23, no. 2–3 SPEC. ISS., pp. 171–182, 2005.

[128] J. Veenstra-VanderWeele, C. L. Muller, H. Iwamoto, J. E. Sauer, W. A. Owens, C. R. Shah, J. Cohen, P. Mannangatti, T. Jessen, B. J. Thompson, R. Ye, T. M. Kerr, A. M. Carneiro, J. N. Crawley, E. Sanders-Bush, D. G. McMahon, S. Ramamoorthy, L. C. Daws, J. S. Sutcliffe, and R. D. Blakely, "Autism gene variant causes hyperserotonemia, serotonin receptor hypersensitivity, social impairment and repetitive behavior.," *Proc. Natl. Acad. Sci. U. S. A.*, vol. 109, no. 14, pp. 5469–74, 2012.

[129] E. M. Daly, Q. Deeley, C. Ecker, M. Craig, B. Hallahan, C. Murphy, P. Johnston, D. Spain, N. Gillan, M. Brammer, V. Giampietro, M. Lamar, L. Page, F. Toal, A. Cleare, S. Surguladze, and D. G. M. Murphy, "Serotonin and the neural processing of facial emotions in adults with autism: an fMRI study using acute tryptophan depletion.," *Arch. Gen. Psychiatry*, vol. 69, no. 10, pp. 1003–13, 2012.

[130] N. Tsujino, Y. Nakatani, Y. Seki, A. Nakasato, M. Nakamura, M. Sugawara, and H. Arita, "Abnormality of circadian rhythm accompanied by an increase in frontal cortex serotonin in animal model of autism," *Neurosci. Res.*, vol. 57, no. 2, pp. 289–295, 2007.

[131] I. Makkonen, R. Riikonen, H. Kokki, M. M. Airaksinen, and J. T. Kuikka, "Serotonin and dopamine transporter binding in children with autism determined by SPECT," *Dev. Med. Child Neurol.*, vol. 50, no. 8, pp. 593–597, 2008.

[132] P. Shih, B. Keehn, J. K. Oram, K. M. Leyden, C. L. Keown, and R. A. Müller, "Functional differentiation of posterior superior temporal sulcus in autism: A functional connectivity magnetic resonance imaging study," *Biol. Psychiatry*, vol. 70, no. 3, pp. 270–277, 2011.

[133] J. Shang, Y. Fu, Z. Ren, T. Zhang, M. Du, Q. Gong, S. Lui, and W. Zhang, "The common traits of the ACC and PFC in anxiety disorders in the DSM-5: Meta-analysis of voxel-based morphometry studies," *PLoS One*, vol. 9, no. 3, 2014.

[134] N. M. Kleinhans, T. Richards, K. Weaver, L. C. Johnson, J. Greenson, G. Dawson, and E. Aylward, "Association between amygdala response to emotional faces and social anxiety in autism spectrum disorders," *Neuropsychologia*, vol. 48, no. 12, pp. 3665–3670, 2010.

[135] S. W. White, D. Oswald, T. Ollendick, and L. Scahill, "Anxiety in children and adolescents with autism spectrum disorders," *Clinical Psychology Review*, vol. 29, no. 3. pp. 216–229, 2009.

[136] A. F. Jorm, M. Prior, A. Sanson, D. Smart, Y. Zhang, and S. Easteal, "Association of a functional polymorphism of the serotonin transporter gene with anxiety-related temperament and behavior problems in children: a longitudinal study from

infancy to the mid-teens.," *Mol. Psychiatry*, vol. 5, no. 5, pp. 542–7, 2000.

[137] S. Katsuragi, H. Kunugi, A. Sano, T. Tsutsumi, K. Isogawa, S. Nanko, and J. Akiyoshi, "Association between serotonin transporter gene polymorphism and anxiety-related traits.," *Biol. Psychiatry*, vol. 45, no. 3, pp. 368–70, 1999.

[138] R. G. King, N. M. Gude, J. L. Di Iulio, and S. P. Brennecke, "Regulation of human placental fetal vessel tone: Role of nitric oxide," *Reprod. Fertil. Dev.*, vol. 7, no. 6, pp. 1407–1411, 1995.

[139] B. Stefanovic, W. Schwindt, M. Hoehn, and A. C. Silva, "Functional uncoupling of hemodynamic from neuronal response by inhibition of neuronal nitric oxide synthase," *J.Cereb.Blood Flow Metab*, vol. 27, no. 0271–678X (Print), pp. 741–754, 2007.

[140] R. Aamand, T. Dalsgaard, Y. C. L. Ho, A. Møller, A. Roepstorff, and T. E. Lund, "A NO way to BOLD?: Dietary nitrate alters the hemodynamic response to visual stimulation," *Neuroimage*, vol. 83, pp. 397–407, 2013.

[141] T. L. Sweeten, D. J. Posey, S. Shankar, and C. J. McDougle, "High nitric oxide production in autistic disorder: a possible role for interferon-gamma.," *Biol. Psychiatry*, vol. 55, no. 4, pp. 434–7, 2004.

[142] M. H. F. S. Tostes, H. C. Teixeira, W. F. Gattaz, M. A. F. Brandão, and N. R. B. Raposo, "Altered neurotrophin, neuropeptide, cytokines and nitric oxide levels in autism," *Pharmacopsychiatry*, vol. 45, no. 6, pp. 241–243, 2012.

[143] S. S. Zoroğlu, M. Yürekli, I. Meram, S. Söğüt, H. Tutkun, O. Yetkin, E. Sivasli, H. A. Savaş, M. Yanik, H. Herken, and O. Akyol, "Pathophysiological role of nitric oxide and adrenomedullin in autism.," *Cell Biochem. Funct.*, vol. 21, no. 1, pp. 55–60, 2003.

[144] B. Wenzel, M. Kunst, C. Günther, G. K. Ganter, R. Lakes-Harlan, N. Elsner, and R. Heinrich, "Nitric oxide/cyclic guanosine monophosphate signaling in the central complex of the grasshopper brain inhibits singing behavior," *J. Comp. Neurol.*, vol. 488, no. 2, pp. 129–139, 2005.

[145] D. Yanagihara and I. Kondo, "Nitric oxide plays a key role in adaptive control of locomotion in cat.," *Proc. Natl. Acad. Sci. U. S. A.*, vol. 93, no. 23, pp. 13292–7, 1996.

[146] E. A. Del Bel, F. S. Guimarães, M. Bermũdez-Echeverry, M. Z. Gomes, A. Schiaveto-De-Souza, F. E. Padovan-Neto, V. Tumas, A. P. Barion-Cavalcanti, M. Lazzarini, L. P. Nucci-Da-Silva, and D. De Paula-Souza, "Role of nitric oxide on motor behavior," *Cellular and Molecular Neurobiology*, vol. 25, no. 2. pp. 371–392, 2005.

[147] H. S. Sharma, L. Wiklund, R. D. Badgaiyan, S. Mohanty, and P. Alm, "Intracerebral administration of neuronal nitric oxide synthase antiserum attenuates traumatic brain injury-induced blood-brain barrier permeability, brain edema formation, and sensory motor disturbances in the rat," *Acta Neurochir. Suppl.*, no. 96, pp. 288–294, 2006.

[148] S. R. Leekam, C. Nieto, S. J. Libby, L. Wing, and J. Gould, "Describing the sensory abnormalities of children and adults with autism," *J. Autism Dev. Disord.*, vol. 37, no. 5, pp. 894–910, 2007.

[149] C. Whyatt and C. Craig, "Sensory-motor problems in Autism," *Front. Integr. Neurosci.*, vol. 7, no. 7, p. 51, 2013.

[150] C. A. Buneo and R. A. Andersen, "Sensorimotor integration in posterior parietal cortex," *Neuropsychologia*, vol. 44, no. 13, pp. 2594–606, 2006.

[151] B. Cerf-Ducastel, P. F. Van De Moortele, P. MacLeod, D. Le Bihan, and A. Faurion, "Interaction of gustatory and lingual somatosensory perceptions at the cortical level in the human: a functional magnetic resonance imaging study.," *Chem. Senses*, vol. 26, pp. 371–383, 2001.

[152] E. Naito, S. Kinomura, S. Geyer, R. Kawashima, P. E. Roland, and K. Zilles, "Fast reaction to different sensory modalities activates common fields in the motor areas, but the anterior cingulate cortex is involved in the speed of reaction.," *J. Neurophysiol.*, vol. 83, no. 3, pp. 1701–1709, 2000.

[153] J. Downar, A. P. Crawley, D. J. Mikulis, and K. D. Davis, “A cortical network sensitive to stimulus salience in a neutral behavioral context across multiple sensory modalities.,” *J. Neurophysiol.*, vol. 87, no. 1, pp. 615–620, 2002.

[154] S. H. Fatemi and T. D. Folsom, “Dysregulation of fragile × mental retardation protein and metabotropic glutamate receptor 5 in superior frontal cortex of individuals with autism: a postmortem brain study.,” *Mol. Autism*, vol. 2, p. 6, 2011.

[155] A. Sheikh, G. Wen, F. Cao, A. Yin, M. Malik, Z. Tauqeer, A. Nagori, M. Schirripa, F. Schirripa, G. Merz, T. Brown, and X. Li, “Alteration of astrocytes and Wnt/beta-catenin signaling in the frontal cortex of autistic subjects,” *J. Neuroinflammation*, vol. 9, no. 1, p. 223, 2012.

[156] D. R. Corfield, K. Murphy, O. Josephs, L. Adams, and R. Turner, “Does hypercapnia-induced cerebral vasodilation modulate the hemodynamic response to neural activation?,” *Neuroimage*, vol. 13, no. 6, pp. 1207–1211, 2001.

[157] D. S. Margulies, J. L. Vincent, C. Kelly, G. Lohmann, L. Q. Uddin, B. B. Biswal, A. Villringer, F. X. Castellanos, M. P. Milham, and M. Petrides, “Precuneus shares intrinsic functional architecture in humans and monkeys.,” *Proc. Natl. Acad. Sci. U. S. A.*, vol. 106, no. 47, pp. 20069–20074, 2009.

[158] S. Zhang and C. shan R. Li, “Functional connectivity mapping of the human precuneus by resting state fMRI,” *Neuroimage*, vol. 59, no. 4, pp. 3548–3562, 2012.

[159] J. R. Andrews-Hanna, J. Smallwood, and R. N. Spreng, “The default network and self-generated thought: Component processes, dynamic control, and clinical relevance,” *Ann. N. Y. Acad. Sci.*, vol. 1316, no. 1, pp. 29–52, 2014.

[160] C. J. Lynch, L. Q. Uddin, K. Supekar, A. Khouzam, J. Phillips, and V. Menon, “Default mode network in childhood autism: Posteromedial cortex heterogeneity and relationship with social deficits,” *Biol. Psychiatry*, vol. 74, no. 3, pp. 212–219, 2013.

[161] S. D. Washington, E. M. Gordon, J. Brar, S. Warburton, A. T. Sawyer, A. Wolfe, E. R. Mease-Ference, L. Girton, A. Hailu, J. Mbwana, W. D. Gaillard, M. L. Kalbfleisch, and J. W. Vanmeter, “Dysmaturation of the default mode network in autism,” *Hum. Brain Mapp.*, vol. 35, no. 4, pp. 1284–1296, 2014.

[162] J. O. Maximo, E. J. Cadena, and R. K. Kana, “The implications of brain connectivity in the neuropsychology of autism,” *Neuropsychology Review*, vol. 24, no. 1. pp. 16–31, 2014.

[163] L. Q. Uddin and V. Menon, “The anterior insula in autism: Under-connected and under-examined,” *Neuroscience and Biobehavioral Reviews*, vol. 33, no. 8. pp. 1198–1203, 2009.

[164] I. M. Eigsti, M. C. Stevens, R. T. Schultz, M. Barton, E. Kelley, L. Naigles, A. Orinstein, E. Troyb, and D. A. Fein, “Language comprehension and brain function in individuals with an optimal outcome from autism,” *NeuroImage Clin.*, vol. 10, pp. 182–191, 2016.

[165] D. L. Williams and N. J. Minshew, “Understanding Autism and Related Disorders: What has Imaging Taught Us?,” *Neuroimaging Clinics of North America*, vol. 17, no. 4. pp. 495–509, 2007.

[166] C. Lamm, J. Decety, and T. Singer, “Meta-analytic evidence for common and distinct neural networks associated with directly experienced pain and empathy for pain,” *Neuroimage*, vol. 54, no. 3, pp. 2492–2502, 2011.

[167] D. P. Kennedy and E. Courchesne, “The intrinsic functional organization of the brain is altered in autism,” *Neuroimage*, vol. 39, no. 4, pp. 1877–1885, 2008.

[168] E. A. H. Von Dem Hagen, R. S. Stoyanova, S. Baron-Cohen, and A. J. Calder, “Reduced functional connectivity within and between ‘social’ resting state networks in autism spectrum conditions,” *Soc. Cogn. Affect. Neurosci.*, vol. 8, no. 6, pp. 694–701, 2013.

[169] P. B. Fitzgerald, A. R. Laird, J. Maller, and Z. J. Daskalakis, “A meta-analytic study of changes in brain activation in

depression," *Hum. Brain Mapp.*, vol. 29, no. 6, pp. 683–695, 2008.

[170] M. Cabanis, M. Pyka, S. Mehl, B. W. Müller, S. Loos-Jankowiak, G. Winterer, W. Wölwer, F. Musso, S. Klingberg, A. M. Rapp, K. Langohr, G. Wiedemann, J. Herrlich, H. Walter, M. Wagner, K. Schnell, K. Vogeley, H. Kockler, N. J. Shah, T. Stöcker, R. Thienel, K. Pauly, A. Krug, and T. Kircher, "The precuneus and the insula in self-attributional processes," *Cogn. Affect. Behav. Neurosci.*, vol. 13, no. 2, pp. 330–345, 2013.

[171] A. Shmuel, M. Augath, A. Oeltermann, and N. K. Logothetis, "Negative functional MRI response correlates with decreases in neuronal activity in monkey visual area V1," *Nat. Neurosci.*, vol. 9, no. 4, pp. 569–577, 2006.

[172] A. Devor, P. Tian, N. Nishimura, I. C. Teng, E. M. C. Hillman, S. N. Narayanan, I. Ulbert, D. A. Boas, D. Kleinfeld, and A. M. Dale, "Suppressed Neuronal Activity and Concurrent Arteriolar Vasoconstriction May Explain Negative Blood Oxygenation Level-Dependent Signal," *J. Neurosci.*, vol. 27, no. 16, pp. 4452–4459, 2007.

[173] W. Maier, A. Zobel, and M. Wagner, "Schizophrenia and bipolar disorder: differences and overlaps.," *Curr. Opin. Psychiatry*, vol. 19, no. 2, pp. 165–170, 2006.

[174] F. Karege, A. Méary, N. Perroud, S. Jamain, M. Leboyer, E. Ballmann, R. Fernandez, A. Malafosse, and F. Schürhoff "Genetic overlap between schizophrenia and bipolar disorder: A study with AKT1 gene variants and clinical phenotypes," *Schizophr. Res.*, vol. 135, no. 1–3, pp. 8–14, 2012.

[175] T. M. Laursen, E. Agerbo, and C. B. Pedersen, "Bipolar disorder, schizoaffective disorder, and schizophrenia overlap: A new comorbidity index," *J. Clin. Psychiatry*, vol. 70, no. 10, pp. 1432–1438, 2009.

[176] P. F. Buckley, B. J. Miller, D. S. Lehrer, and D. J. Castle, "Psychiatric comorbidities and schizophrenia," *Schizophr. Bull.*, vol. 35, no. 2, pp. 383–402, 2009.

[177] G. Salvadore, J. A. Quiroz, R. Machado-Vieira, I. D. Henter, H. K. Manji, and C. A. Zarate, "The neurobiology of the switch process in bipolar disorder: A review," *Journal of Clinical Psychiatry*, vol. 71, no. 11. pp. 1488–1501, 2010.

[178] M. P. Van Den Heuvel and H. E. Hulshoff Pol, "Exploring the brain network: A review on resting-state fMRI functional connectivity," *Eur. Neuropsychopharmacol.*, vol. 20, no. 8, pp. 519–534, 2010.

[179] A. Anticevic, A. Savic, G. Repovs, G. Yang, D. R. McKay, E. Sprooten, E. E. Knowles, J. H. Krystal, G. D. Pearlson, and D. C. Glahn, "Ventral anterior cingulate connectivity distinguished nonpsychotic bipolar illness from psychotic bipolar disorder and schizophrenia," *Schizophr. Bull.*, vol. 41, no. 1, pp. 133–143, 2015.

[180] S. A. Meda, A. Gill, M. C. Stevens, R. P. Lorenzoni, D. C. Glahn, V. D. Calhoun, J. A. Sweeney, C. A. Tamminga, M. S. Keshavan, G. Thaker, and G. D. Pearlson, "Differences in resting-state functional magnetic resonance imaging functional network connectivity between schizophrenia and psychotic bipolar probands and their unaffected first-degree relatives," *Biol. Psychiatry*, vol. 71, no. 10, pp. 881–889, 2012.

[181] S. Selek, H. A. Savas, H. S. Gergerlioglu, F. Bulbul, E. Uz, and M. Yumru, "The course of nitric oxide and superoxide dismutase during treatment of bipolar depressive episode," *J. Affect. Disord.*, vol. 107, no. 1–3, pp. 89–94, 2008.

[182] A. C. Andreazza, M. Kauer-Sant'Anna, B. N. Frey, D. J. Bond, F. Kapczinski, L. T. Young, and L. N. Yatham, "Oxidative stress markers in bipolar disorder: A meta-analysis," *J. Affect. Disord.*, vol. 111, no. 2–3. pp. 135–144, 2008.

[183] B. B. Quednow, M. A. Geyer, and A. L. Halberstadt, Serotonin and Schizophrenia. in Muller CP, Jacobs B, editors, *Handbook of the Behavioral Neurobiology of Serotonin,* Academic, London, 2010.

[184] G. M. Wilson, S. Flibotte, V. Chopra, B. L. Melnyk, W. G. Honer, and R. A. Holt, "DNA copy-number analysis in bipolar disorder and schizophrenia reveals aberrations in genes involved in glutamate signaling," *Hum. Mol. Genet.*, vol. 15, no. 5, pp. 743–749, 2006.

[185] S. Y. T. Cherlyn, P. S. Woon, J. J. Liu, W. Y. Ong, G. C. Tsai, and K. Sim, "Genetic association studies of glutamate, GABA and related genes in schizophrenia and bipolar disorder: A decade of advance," *Neuroscience and Biobehavioral Reviews*, vol. 34, no. 6. pp. 958–977, 2010.

[186] K. R. Sreenivasan, M. Havlicek, and G. Deshpande, "Non-Parametric Hemodynamic Deconvolution of fMRI using Homomorphic Filtering," *IEEE Trans. Med. Imaging*, vol. 62, no. c, pp. 1–1, 2014.

[187] J. F. Leckman, D. Sholomskas, W. D. Thompson, A. Belanger, and M. M. Weissman, "Best estimate of lifetime psychiatric diagnosis: a methodological study.," *Arch. Gen. Psychiatry*, vol. 39, no. 8, pp. 879–83, 1982.

[188] P. A. Gowland and R. Bowtell, "Theoretical optimization of multi-echo fMRI data acquisition.," *Phys. Med. Biol.*, vol. 52, no. 7, pp. 1801–13, 2007.

[189] Mazaika, Hoeft, Glovera, P. K. Mazaika, F. Hoeft, G. H. Glover, and A. L. Reiss, "Methods and Software for fMRI Analysis for Clinical Subjects," *Hum. Brain Mapp.*, p. 77309, 2009.

[190] S. Posse, S. Wiese, D. Gembris, K. Mathiak, C. Kessler, M. L. Grosse-Ruyken, B. Elghahwagi, T. Richards, S. R. Dager, and V. G. Kiselev, "Enhancement of BOLD-contrast sensitivity by single-shot multi-echo functional MR imaging," *Magn. Reson. Med.*, vol. 42, no. 1, pp. 87–97, 1999..

[191] G. H. Glover, T. Q. Li, and D. Ress, "Image-based method for retrospective correction of physiological motion effects in fMRI: RETROICOR," *Magn. Reson. Med.*, vol. 44, no. 1, pp. 162–167, 2000.

[192] N. Petridou, C. C. Gaudes, I. L. Dryden, S. T. Francis, and P. A. Gowland, "Periods of rest in fMRI contain individual spontaneous events which are related to slowly fluctuating spontaneous activity," *Hum. Brain Mapp.*, vol. 34, no. 6, pp. 1319–1329, 2013.

[193] T. E. J. Behrens, H. Johansen-Berg, M. W. Woolrich, S. M. Smith, C. A. M. Wheeler-Kingshott, P. A. Boulby, G. J. Barker, E. L. Sillery, K. Sheehan, O. Ciccarelli, A. J. Thompson, J. M. Brady, and P. M. Matthews, "Non-invasive mapping of connections between human thalamus and cortex using diffusion imaging.," *Nat. Neurosci.*, vol. 6, no. 7, pp. 750–7, 2003.

[194] A. Morel, *Stereotactic Atlas of the Human Thalamus and Basal Ganglia*. CRC Press, London, 2007.

[195] A. Krauth, R. Blanc, A. Poveda, D. Jeanmonod, A. Morel, and G. Székely, "A mean three-dimensional atlas of the human thalamus: Generation from multiple histological data," *Neuroimage*, vol. 49, no. 3, pp. 2053–2062, 2010.

[196] T. E. J. Behrens, H. Johansen-Berg, M. W. Woolrich, S. M. Smith, C. A. M. Wheeler-Kingshott, P. A. Boulby, G. J. Barker, E. L. Sillery, K. Sheehan, O. Ciccarelli, A. J. Thompson, J. M. Brady, and P. M. Matthews, "Non-invasive mapping of connections between human thalamus and cortex using diffusion imaging.," *Nat. Neurosci.*, vol. 6, no. 7, pp. 750–7, 2003.

[197] A. Krauth, R. Blanc, A. Poveda, D. Jeanmonod, A. Morel, and G. Székely, "A mean three-dimensional atlas of the human thalamus: Generation from multiple histological data," *Neuroimage*, vol. 49, no. 3, pp. 2053–2062, 2010.

[198] C. Chang, M. E. Thomason, and G. H. Glover, "Mapping and correction of vascular hemodynamic latency in the BOLD signal," *Neuroimage*, vol. 43, no. 1, pp. 90–102, 2008.

[199] L. J. Kemna and S. Posse, "Effect of respiratory CO(2) changes on the temporal dynamics of the hemodynamic response in functional MR imaging.," *Neuroimage*, vol. 14, no. 3, pp. 642–649, 2001.

[200] G. Buzsáki, K. Kaila, and M. Raichle, "Inhibition and Brain Work," *Neuron*, vol. 56, no. 5. pp. 771–783, 2007.

[201] G. G. Brown, L. T. Eyler Zorrilla, B. Georgy, S. S. Kindermann, E. C. Wong, and R. B. Buxton, "BOLD and perfusion response to finger-thumb apposition after acetazolamide administration: differential relationship to global perfusion.," *J.*

Cereb. Blood Flow Metab., vol. 23, no. 7, pp. 829–37, 2003.

[202] L. M. Rowland, K. Kontson, J. West, R. A. Edden, H. Zhu, S. A. Wijtenburg, H. H. Holcomb, and P. B. Barker, "In vivo measurements of glutamate, GABA, and NAAG in schizophrenia," *Schizophr. Bull.*, vol. 39, no. 5, pp. 1096–1104, 2013.

[203] L. Rowland, B. Krause, S. Wijtenburg, R. Mcmahon, J. Chiappelli, K. Nugent, S. Nisonger, S. Korenic, P. Kochunov, and L. Hong, "Medial frontal GABA is lower in older schizophrenia: a MEGA-PRESS with macromolecule suppression study," *Mol. Psychiatry*, vol. 21, pp. 198–204, 2015.

[204] S. F. Taylor and I. F. Tso, "GABA abnormalities in schizophrenia: A methodological review of in vivo studies," *Schizophrenia Research*, vol. 167, no. 1–3. pp. 84–90, 2015.

[205] S. Akbarian, J. J. Kim, S. G. Potkin, J. O. Hagman, A. Tafazzoli, W. E. Bunney Jr., and E. G. Jones, "Gene expression for glutamic acid decarboxylase is reduced without loss of neurons in prefrontal cortex of schizophrenics," *Arch Gen Psychiatry*, vol. 52, no. 4, pp. 258–266, 1995.

[206] T. Hashimoto, H. H. Bazmi, K. Mirnics, Q. Wu, A. R. Sampson, and D. A. Lewis, "Conserved regional patterns of GABA-related transcript expression in the neocortex of subjects with schizophrenia," *Am. J. Psychiatry*, vol. 165, no. 4, pp. 479–489, 2008.

[207] F. M. Benes, B. Lim, D. Matzilevich, J. P. Walsh, S. Subburaju, and M. Minns, "Regulation of the GABA cell phenotype in hippocampus of schizophrenics and bipolars.," *Proc. Natl. Acad. Sci. U. S. A.*, vol. 104, pp. 10164–10169, 2007.

[208] R. O. Brady, J. M. Mccarthy, A. P. Prescot, J. E. Jensen, A. J. Cooper, B. M. Cohen, P. F. Renshaw, and D. Öngür, "Brain gamma-aminobutyric acid (GABA) abnormalities in bipolar disorder," *Bipolar Disord.*, vol. 15, no. 4, pp. 434–439, 2013.

[209] S. H. Fatemi and T. D. Folsom, "GABA receptor subunit distribution and FMRP–mGluR5 signaling abnormalities in the cerebellum of subjects with schizophrenia, mood disorders, and autism," *Schizophr. Res.*, vol. 167, no. 1, pp. 42–56, 2015.

[210] A. Abi-Dargham, M. Laruelle, G. K. Aghajanian, D. Charney, and J. Krystal, "The role of serotonin in the pathophysiology and treatment of schizophrenia.," *J. Neuropsychiatry Clin. Neurosci.*, vol. 9, pp. 1–17, 1997.

[211] A. Carrard, A. Salzmann, A. Malafosse, and F. Karege, "Increased DNA methylation status of the serotonin receptor 5HTR1A gene promoter in schizophrenia and bipolar disorder," *J. Affect. Disord.*, vol. 132, no. 3, pp. 450–453, 2011.

[212] G. M. Sullivan, R. T. Ogden, M. A. Oquendo, J. S. D. Kumar, N. Simpson, Y. Huang, J. J. Mann, and R. V. Parsey, "Positron Emission Tomography Quantification of Serotonin-1A Receptor Binding in Medication-Free Bipolar Depression," *Biol. Psychiatry*, vol. 66, no. 3, pp. 223–230, 2009.

[213] M. Rees, N. Norton, I. Jones, F. McCandless, J. Scourfield, P. Holmans, S. Moorhead, E. Feldman, S. Sadler, T. Cole, K. Redman, A. Farmer, P. McGuffin, M. J. Owen, and N. Craddock, "Association studies of bipolar disorder at the human serotonin transporter gene (hSERT; 5HTT).," *Mol. Psychiatry*, vol. 2, no. 5, pp. 398–402, 1997.

[214] A. N. M. Schoffelmeer, G. Wardeh, and L. J. M. J. Vanderschuren, "Expression of serotonin 5-HT2A receptors in the human cerebellum and alterations in schizophrenia," *Synapse*, vol. 42, no. 2, pp. 104–114, 2001.

[215] P. W. J. Burnet, S. L. Eastwood, and P. J. Harrison, "5-HT(1A) 5-HT(2A) receptor mRNAs and binding site densities are differentially altered in schizophrenia," *Neuropsychopharmacology*, vol. 15, no. 5, pp. 442–455, 1996.

[216] D. M. Cannon, M. Ichise, S. J. Fromm, A. C. Nugent, D. Rollis, S. K. Gandhi, J. M. Klaver, D. S. Charney, H. K. Manji, and W. C. Drevets, "Serotonin Transporter Binding in Bipolar Disorder Assessed using [11C]DASB and Positron Emission Tomography," *Biol. Psychiatry*, vol. 60, no. 3, pp. 207–217, 2006.

[217] M. A. Oquendo, R. S. Hastings, Y. Y. Huang, N. Simpson, R. T. Ogden, X.-Z. Hu, D. Goldman, V. Arango, R. L. Van Heertum, J. J. Mann, and R. V Parsey, "Brain serotonin transporter binding in depressed patients with bipolar disorder

using positron emission tomography.," *Arch. Gen. Psychiatry*, vol. 64, no. 2, pp. 201–8, 2007.

[218] R. E. Smith, V. Haroutunian, K. L. Davis, and J. H. Meador-Woodruff, "Expression of excitatory amino acid transporter transcripts in the thalamus of subjects with schizophrenia," *Am. J. Psychiatry*, vol. 158, no. 9, pp. 1393–1399, 2001.

[219] H. M. Ibrahim, A. J. Hogg, D. J. Healy, V. Haroutunian, K. L. Davis, and J. H. Meador-Woodruff, "Ionotropic glutamate receptor binding and subunit mRNA expression in thalamic nuclei in schizophrenia.," *Am. J. Psychiatry*, vol. 157, no. 11, pp. 1811–1823, 2000.

[220] S. Akbarian, N. J. Sucher, D. Bradley, A. Tafazzoli, D. Trinh, W. P. Hetrick, S. G. Potkin, C. A. Sandman, W. E. Bunney, and E. G. Jones, "Selective alterations in gene expression for NMDA receptor subunits in prefrontal cortex of schizophrenics.," *J. Neurosci.*, vol. 16, no. 1, pp. 19–30, 1996.

[221] D. Bauer, D. Gupta, V. Harotunian, J. H. Meador-Woodruff, and R. E. McCullumsmith, "Abnormal expression of glutamate transporter and transporter interacting molecules in prefrontal cortex in elderly patients with schizophrenia," *Schizophr. Res.*, vol. 104, no. 1–3, pp. 108–120, 2008.

[222] S. M. O'Donovan, K. Hasselfeld, D. Bauer, M. Simmons, P. Roussos, V. Haroutunian, J. H. Meador-Woodruff, and R. E. McCullumsmith, "Glutamate transporter splice variant expression in an enriched pyramidal cell population in schizophrenia.," *Transl. Psychiatry*, vol. 5, no. 2, p. e579, 2015.

[223] M. A. Frye, J. Watzl, S. Banakar, J. O'Neill, J. Mintz, P. Davanzo, J. Fischer, J. W. Chirichigno, J. Ventura, S. Elman, J. Tsuang, I. Walot, and M. A. Thomas, "Increased anterior cingulate/medial prefrontal cortical glutamate and creatine in bipolar depression.," *Neuropsychopharmacology*, vol. 32, no. 12, pp. 2490–9, 2007.

[224] R. F. Deicken, Y. Eliaz, R. Feiwell, and N. Schuff, "Increased thalamic N-acetylaspartate in male patients with familial bipolar I disorder.," *Psychiatry Res.*, vol. 106, no. 1, pp. 35–45, 2001.

[225] A. Uezato, J. H. Meador-Woodruff, and R. E. McCullumsmith, "Vesicular glutamate transporter mRNA expression in the medial temporal lobe in major depressive disorder, bipolar disorder, and schizophrenia," *Bipolar Disord.*, vol. 11, no. 7, pp. 711–725, 2009.

[226] C. N. Karson, W. S. T. Griffin, R. E. Mrak, M. Husain, T. M. Dawson, S. H. Snyder, N. C. Moore, and W. Q. Sturner, "Nitric oxide synthase (NOS) in schizophrenia - Increases in cerebellar vermis," *Mol. Chem. Neuropathol.*, vol. 27, no. 3, pp. 275–284, 1996.

[227] H. A. Savaş, H. Herken, M. Yürekli, E. Uz, H. Tutkun, S. S. Zoroğlu, M. E. Özen, B. Cengiz, and Ö. Akyol, "Possible role of nitric oxide and adrenomedullin in bipolar affective disorder," *Neuropsychobiology*, vol. 45, no. 2, pp. 57–61, 2002.

[228] J. C. Klein, M. F. S. Rushworth, T. E. J. Behrens, C. E. Mackay, A. J. de Crespigny, H. D'Arceuil, and H. Johansen-Berg, "Topography of connections between human prefrontal cortex and mediodorsal thalamus studied with diffusion tractography," *Neuroimage*, vol. 51, no. 2, pp. 555–564, 2010.

[229] E. F. S. Kaufman and A. C. Rosenquist, "Efferent projections of the thalamic intralaminar nuclei in the cat," *Brain Res.*, vol. 335, no. 2, pp. 257–279, 1985.

[230] S. T. Sakai, "Corticonigral projections from area 6 in the raccoon," *Exp. Brain Res.*, vol. 73, no. 3, pp. 498–504, 1988.

[231] E. F. Kaufman and A. C. Rosenquist, "Afferent connections of the thalamic intralaminar nuclei in the cat.," *Brain Res.*, vol. 335, no. 2, pp. 281–96, Jun. 1985.

[232] S. H. Jang, H. W. Lim, and S. S. Yeo, "The neural connectivity of the intralaminar thalamic nuclei in the human brain: A diffusion tensor tractography study.," *Neurosci. Lett.*, 2014.

[233] V. J. Kumar, E. Van Oort, K. Scheffler, C. F. Beckmann, and W. Grodd, "Functional anatomy of the human thalamus at

rest," *Neuroimage*, vol. 147, pp. 678–691, Feb. 2017.

[234] R. J. Sutherland, "The dorsal diencephalic conduction system: A review of the anatomy and functions of the habenular complex," *Neurosci. Biobehav. Rev.*, vol. 6, no. 1, pp. 1–13, 1982.

[235] W. R. Klemm, "Habenular and interpeduncularis nuclei: shared components in multiple-function networks.," *Med. Sci. Monit.*, vol. 10, no. 11, p. RA261-A273, 2004.

[236] V. A. Magnotta, M. L. Adix, A. Caprahan, K. Lim, R. Gollub, and N. C. Andreasen, "Investigating connectivity between the cerebellum and thalamus in schizophrenia using diffusion tensor tractography: A pilot study," *Psychiatry Res. - Neuroimaging*, vol. 163, no. 3, pp. 193–200, 2008.

[237] M. Argyelan, M. Carbon, M. Niethammer, A. M. Ulug, H. U. Voss, S. B. Bressman, V. Dhawan, and D. Eidelberg, "Cerebellothalamocortical connectivity regulates penetrance in dystonia.," *J. Neurosci.*, vol. 29, no. 31, pp. 9740–9747, 2009.

[238] D. Ristanović, N. T. Milošević, B. D. Stefanović, D. L. Marić, and K. Rajković, "Morphology and classification of large neurons in the adult human dentate nucleus: A qualitative and quantitative analysis of 2D images," *Neurosci. Res.*, vol. 67, no. 1, pp. 1–7, 2010.

[239] R. W. Guillery and S. M. Sherman, "Thalamic relay functions and their role in corticocortical communication: Generalizations from the visual system," *Neuron*, vol. 33, no. 2. pp. 163–175, 2002.

[240] E. A. Pelzer, A. Hintzen, M. Goldau, D. Y. Von Cramon, L. Timmermann, and M. Tittgemeyer, "Cerebellar networks with basal ganglia: Feasibility for tracking cerebello-pallidal and subthalamo-cerebellar projections in the human brain," *European Journal of Neuroscience*, vol. 38, no. 8. pp. 3106–3114, 2013.

[241] R. P. Dum and P. L. Strick, "An Unfolded Map of the Cerebellar Dentate Nucleus and its Projections to the Cerebral Cortex," *J. Neurophysiol.*, vol. 89, no. 1, pp. 634–639, 2002.

[242] A. Mason, I. A. Ilinsky, S. Maldonado, and K. Kultas-Ilinsky, "Thalamic terminal fields of individual axons from the ventral part of the dentate nucleus of the cerebellum in Macaca mulatta.," *J. Comp. Neurol.*, vol. 421, no. 3, pp. 412–28, Jun. 2000.

[243] N. C. Andreasen, D. S. O'Leary, T. Cizadlo, S. Arndt, K. Rezai, L. L. Ponto, G. L. Watkins, and R. D. Hichwa, "Schizophrenia and cognitive dysmetria: a positron-emission tomography study of dysfunctional prefrontal-thalamic-cerebellar circuitry.," *Proc. Natl. Acad. Sci. U. S. A.*, vol. 93, no. 18, pp. 9985–90, 1996.

[244] R. C. Welsh, A. C. Chen, and S. F. Taylor, "Low-frequency BOLD fluctuations demonstrate altered thalamocortical connectivity in schizophrenia," *Schizophr. Bull.*, vol. 36, no. 4, pp. 713–722, 2010.

[245] N. D. Woodward, H. Karbasforoushan, and S. Heckers, "Thalamocortical dysconnectivity in schizophrenia," *Am. J. Psychiatry*, vol. 169, no. 10, pp. 1092–1099, 2012.

[246] S. Marenco, J. L. Stein, A. A. Savostyanova, F. Sambataro, H. Y. Tan, A. L. Goldman, B. A. Verchinski, A. S. Barnett, D. Dickinson, J. a Apud, J. H. Callicott, A. Meyer-Lindenberg, and D. R. Weinberger, "Investigation of Anatomical Thalamo-Cortical Connectivity and fMRI Activation in Schizophrenia," *Neuropsychopharmacology*, vol. 37, no. 2, pp. 499–507, 2012.

[247] M. Argyelan, T. Ikuta, P. Derosse, R. J. Braga, K. E. Burdick, M. John, P. B. Kingsley, A. K. Malhotra, and P. R. Szeszko, "Resting-state fMRI connectivity impairment in schizophrenia and bipolar disorder," *Schizophr. Bull.*, vol. 40, no. 1, pp. 100–110, 2014.

[248] A. Anand, Y. Li, Y. Wang, M. J. Lowe, and M. Dzemidzic, "Resting state corticolimbic connectivity abnormalities in

unmedicated bipolar disorder and unipolar depression," *Psychiatry Res. Neuroimaging*, vol. 171, no. 3, pp. 189–198, 2009.

[249] M. Deschˆnes, J. Bourassa, and A. Parent, "Two different types of thalamic fibers innervate the rat striatum," *Brain Res.*, vol. 701, no. 1–2, pp. 288–292, 1995.

[250] M. E. Erro, J. L. Lanciego, and J. M. Giménez-Amaya, "A re-examination of the striatal input from the mediodorsal thalamic nucleus in the rat," *European Journal of Anatomy*, vol. 4, no. 2. pp. 95–101, 2000.

[251] N. Axten, A. Newell, and H. A. Simon, "Human Problem Solving.," *Contemp. Sociol.*, vol. 2, no. 2, p. 169, 1973.

[252] S. Ohlsson, Information-processing explanations of insight and related phenomena. In M. T. Keane and K. J. Gilhooly, editors, *Advances in the psychology of thinking*, Harvester Wheatsheaf, London, 1992.

[253] M. Jung-Beeman and E. M. Bowden, "The right hemisphere maintains solution-related activation for yet-to-be-solved problems," *Mem. Cognit.*, vol. 28, no. 7, pp. 1231–1241, 2000.

[254] E. M. Bowden and M. Jung-Beeman, "Aha! Insight experience correlates with solution activation in the right hemisphere," *Psychon. Bull. Rev.*, vol. 10, no. 3, pp. 730–737, 2003.

[255] M. Jung-Beeman, E. M. Bowden, J. Haberman, J. L. Frymiare, S. Arambel-Liu, R. Greenblatt, P. J. Reber, and J. Kounios, "Neural activity when people solve verbal problems with insight," *PLoS Biol.*, vol. 2, no. 4, 2004.

[256] M. Beeman, Coarse semantic coding and discourse comprehension. In M. Beeman, and C. Chiarello, editors, *Right hemisphere language comprehension: Perspectives from cognitive neuroscience*, Erlbaum, New Jersey, 1998.

[257] D. A. Treffert, "The savant syndrome: an extraordinary condition. A synopsis: past, present, future," *Philos. Trans. R. Soc. B Biol. Sci.*, vol. 364, no. 1522, pp. 1351–1357, 2009.

[258] C. A. Kaplan and H. A. Simon, "In search of insight," *Cogn. Psychol.*, vol. 22, no. 3, pp. 374–419, 1990.

[259] J. N. MacGregor, T. C. Ormerod, and E. P. Chronicle, "Information Processing and Insight: A Process Model of Performance on the Nine-Dot and Related Problems," *J. Exp. Psychol. Learn. Mem. Cogn.*, vol. 27, no. 1, pp. 176–201, 2001.

[260] J. Kounios and M. Beeman, "The cognitive neuroscience of insight.," *Annu. Rev. Psychol.*, vol. 65, pp. 71–93, 2014.

[261] J. Luo and G. Knoblich, "Studying insight problem solving with neuroscientific methods," *Methods*, vol. 42, no. 1, pp. 77–86, 2007.

[262] E. M. Bowden, M. Jung-Beeman, J. Fleck, and J. Kounios, "New approaches to demystifying insight," *Trends in Cognitive Sciences*, vol. 9, no. 7. pp. 322–328, 2005.

[263] E. P. Chronicle, T. C. Ormerod, and J. N. Macgregor, "When insight just won't come: The failure of visual cues in the nine-dot problem," *Q. J. Exp. Psychol.*, vol. 54, no. 3, pp. 903–919, 2001.

[264] M. Öllinger, G. Jones, and G. Knoblich, "Investigating the effect of mental set on insight problem solving," *Exp. Psychol.*, vol. 55, no. 4, pp. 269–282, 2008.

[265] J. Luo and K. Niki, "Function of hippocampus in 'insight' of problem solving," *Hippocampus*, vol. 13, no. 3. pp. 316–323, 2003.

[266] X. Ding, Y. Y. Tang, C. Cao, Y. Deng, Y. Wang, X. Xin, and M. I. Posner, "Short-term meditation modulates brain activity of insight evoked with solution cue," *Soc. Cogn. Affect. Neurosci.*, vol. 10, no. 1, pp. 43–49, 2015.

[267] J. Qiu, H. Li, J. Jou, J. Liu, Y. Luo, T. Feng, Z. Wu, and Q. Zhang, "Neural correlates of the 'Aha' experiences: Evidence from an fMRI study of insight problem solving," *Cortex*, vol. 46, no. 3, pp. 397–403, 2010.

[268] C.-T. Lung and R. L. Dominowski, "Effects of Strategy Instructions and Practice on Nine-Dot Problem Solving," *J. Exp. Psychol. Learn. Mem. Cogn.*, vol. 11, no. 4, pp. 804–811, 1985.

[269] D. Scheinost, M. Hampson, M. Qiu, J. Bhawnani, R. T. Constable, and X. Papademetris, “A graphics processing unit accelerated motion correction algorithm and modular system for real-time fMRI,” *Neuroinformatics*, vol. 11, no. 3, pp. 291–300, 2013.

[270] X. Papademetris, M. P. Jackowski, N. Rajeevan, M. Distasio, H. Okuda, R. T. Constable, and L. H. Staib, “BioImage Suite : An integrated medical image analysis suite : An update,” *Insight J.*, pp. 1–6, 2006.

[271] M. Hampson, D. Scheinost, M. Qiu, J. Bhawnani, C. M. Lacadie, J. F. Leckman, R. T. Constable, and X. Papademetris, “Biofeedback of real-time functional magnetic resonance imaging data from the supplementary motor area reduces functional connectivity to subcortical regions.,” *Brain Connect.*, vol. 1, no. 1, pp. 91–8, 2011.

[272] E. K. Molloy, M. E. Meyerand, and R. M. Birn, “The influence of spatial resolution and smoothing on the detectability of resting-state and task fMRI,” *Neuroimage*, vol. 86, pp. 221–230, 2014.

[273] S. Lacey, R. Stilla, K. Sreenivasan, G. Deshpande, and K. Sathian, “Spatial imagery in haptic shape perception,” *Neuropsychologia*, vol. 60, no. 1, pp. 144–158, 2014.

[274] P. Liang, Z. Li, G. Deshpande, Z. Wang, X. Hu, and K. Li, “Altered causal connectivity of resting state brain networks in amnesic MCI,” *PLoS One*, vol. 9, no. 3, 2014.

[275] G. Deshpande and X. Hu, “Investigating effective brain connectivity from fMRI data: past findings and current issues with reference to Granger causality analysis,” *Brain Connect.*, vol. 2, no. 5 PG-235-245, pp. 235–245, 2012.

[276] G. Deshpande, S. LaConte, G. A. James, S. Peltier, and X. Hu, “Multivariate granger causality analysis of fMRI data,” *Hum. Brain Mapp.*, vol. 30, no. 4, pp. 1361–1373, 2009.

[277] B. Biller and B. L. Nelson, “Modeling and generating multivariate time-series input processes using a vector autoregressive technique,” *ACM Trans. Model. Comput. Simul.*, vol. 13, no. 3, pp. 211–237, 2003.

[278] Y. Wang, S. Katwal, B. Rogers, J. Gore, and G. Deshpande, “Experimental Validation of Dynamic Granger Causality for Inferring Stimulus-evoked Sub-100ms Timing Differences from fMRI.,” *IEEE Trans. Neural Syst. Rehabil. Eng.*, vol. 4320, no. c, 2016.

[279] G. Bellucci, S. Chernyak, M. Hoffman, G. Deshpande, O. Dal Monte, K. M. Knutson, J. Grafman, and F. Krueger, “Effective connectivity of brain regions underlying third-party punishment: Functional MRI and Granger causality evidence,” *Soc. Neurosci.*, vol. 12, no. 2, pp. 124–134, 2017.

[280] C. Feng, G. Deshpande, C. Liu, R. Gu, Y. J. Luo, and F. Krueger, “Diffusion of responsibility attenuates altruistic punishment: A functional magnetic resonance imaging effective connectivity study,” *Hum. Brain Mapp.*, vol. 37, no. 2, pp. 663–677, 2016.

[281] K. Goodyear, R. Parasuraman, S. Chernyak, E. De Visser, P. Madhavan, G. Deshpande, and F. Krueger, “An fMRI and effective connectivity study investigating miss errors during advice utilization from human and machine agents,” *Soc. Neurosci.*, pp. 1–12, 2016.

[282] G. Deshpande, K. Sathian, and X. Hu, “Assessing and compensating for zero-lag correlation effects in time-lagged granger causality analysis of fMRI,” *IEEE Trans. Biomed. Eng.*, vol. 57, no. 6, pp. 1446–1456, 2010.

[283] K. Goodyear, R. Parasuraman, S. Chernyak, P. Madhavan, G. Deshpande, and F. Krueger, “Advice Taking from Humans and Machines: An fMRI and Effective Connectivity Study,” *Front. Hum. Neurosci.*, vol. 10, 2016.

[284] K. R. Sreenivasan, X. Zhuang, S. Banks, V. Mishra, Z. Yang, G. Deshpande, and D. Cordes, “Olfactory Network differences in Master Sommeliers: Connectivity Analysis Using Granger Causality and Graph-theoretical Approach.,” Brain Connect., vol. 1, no. 2, pp. 123-136, 2017.

[285] G. Deshpande, L. E. Libero, K. R. Sreenivasan, H. D. Deshpande, and R. K. Kana, “Identification of neural connectivity signatures of autism using machine learning.,” *Front Hum Neurosci*, vol. 7, no. 10, p. 670, 2013.

[286] C. Jin, H. Jia, P. Lanka, D. Rangaprakash, L. Li, T. Liu, X. Hu, G. Deshpande, "Dynamic brain connectivity is a better predictor of PTSD than static connectivity", Human Brain Mapping, 2017 (in press).

[287] S. Ryali, T. Chen, K. Supekar, and V. Menon, “Estimation of functional connectivity in fMRI data using stability selection-based sparse partial correlation with elastic net penalty,” *Neuroimage*, vol. 59, no. 4, pp. 3852–3861, 2012.

[288] M. M. Grant, D. White, J. Hadley, N. Hutcheson, R. Shelton, K. Sreenivasan, and G. Deshpande, “Early life trauma and directional brain connectivity within major depression,” *Hum. Brain Mapp.*, vol. 35, no. 9, pp. 4815–4826, 2014.

[289] L. E. Libero, T. P. DeRamus, A. C. Lahti, G. Deshpande, and R. K. Kana, “Multimodal neuroimaging based classification of autism spectrum disorder using anatomical, neurochemical, and white matter correlates,” *Cortex*, vol. 66, pp. 46–59, 2015.

[290] M. M. Grant, K. Wood, K. Sreenivasan, M. Wheelock, D. White, J. Thomas, D. C. Knight, and G. Deshpande, “Influence of Early Life Stress on Intra- and Extra-Amygdaloid Causal Connectivity.,” *Neuropsychopharmacology*, vol. 40, no. 7, pp. 1–12, 2015.

[291] N. L. Hutcheson, K. R. Sreenivasan, G. Deshpande, M. A. Reid, J. Hadley, D. M. White, L. Ver Hoef, and A. C. Lahti, “Effective connectivity during episodic memory retrieval in schizophrenia participants before and after antipsychotic medication,” *Hum. Brain Mapp.*, vol. 36, no. 4, pp. 1442–1457, 2015.

[292] M. D. Wheelock, K. R. Sreenivasan, K. H. Wood, L. W. Ver Hoef, G. Deshpande, and D. C. Knight, “Threat-related learning relies on distinct dorsal prefrontal cortex network connectivity,” *Neuroimage*, vol. 102, no. P2, pp. 904–912, 2014.

[293] K. Sathian, G. Deshpande, and R. Stilla, “Neural Changes with Tactile Learning Reflect Decision-Level Reweighting of Perceptual Readout,” *J. Neurosci.*, vol. 33, no. 12, pp. 5387–5398, 2013.

[294] S. Sandkühler and J. Bhattacharya, “Deconstructing insight: EEG correlates of insightful problem solving,” *PLoS One*, vol. 3, no. 1, 2008.

[295] F. Tian, S. Tu, J. Qiu, J. Y. Lv, D. T. Wei, Y. H. Su, and Q. L. Zhang, “Neural correlates of mental preparation for successful insight problem solving,” *Behav. Brain Res.*, vol. 216, no. 2, pp. 626–630, 2011.

[296] M. Ellamil, C. Dobson, M. Beeman, and K. Christoff, “Evaluative and generative modes of thought during the creative process,” *Neuroimage*, vol. 59, no. 2, pp. 1783–1794, 2012.

[297] X. Hao, S. Cui, W. Li, W. Yang, J. Qiu, and Q. Zhang, “Enhancing insight in scientific problem solving by highlighting the functional features of prototypes: An fMRI study,” *Brain Res.*, vol. 1534, pp. 46–54, 2013.

[298] J. Qiu, H. Li, D. Yang, Y. Luo, Y. Li, Z. Wu, and Q. Zhang, “The neural basis of insight problem solving: An event-related potential study,” *Brain Cogn.*, vol. 68, no. 1, pp. 100–106, 2008.

[299] A. Fink, R. H. Grabner, M. Benedek, G. Reishofer, V. Hauswirth, M. Fally, C. Neuper, F. Ebner, and A. C. Neubauer, “The creative brain: Investigation of brain activity during creative problem solving by means of EEG and fMRI,” *Hum. Brain Mapp.*, vol. 30, no. 3, pp. 734–748, 2009.

[300] C. Reverberi, A. Lavaroni, G. L. Gigli, M. Skrap, and T. Shallice, “Specific impairments of rule induction in different frontal lobe subgroups,” *Neuropsychologia*, vol. 43, no. 3, pp. 460–472, 2005.

[301] J. Duncan, “An adaptive coding model of neural function in prefrontal cortex,” *Nat Rev Neurosci*, vol. 2, no. 11, pp. 820–829, 2001.

[302] C. D. Frith, The role of dorsolateral prefrontal cortex in the selection of action as revealed by functional imaging, In S. Monsell and J. Driver, editors, *Control of Cogitive Process*, MIT press, Cambrige, 2000.

[303] C. A. Seger, J. E. Desmond, G. H. Glover, and J. D. Gabrieli, "Functional magnetic resonance imaging evidence for right-hemisphere involvement in processing unusual semantic relationships.," *Neuropsychology*, vol. 14, no. 3, pp. 361–9, 2000.

[304] R. Stanescu-Cosson, P. Pinel, P. F. van De Moortele, D. Le Bihan, L. Cohen, and S. Dehaene, "Understanding dissociations in dyscalculia: a brain imaging study of the impact of number size on the cerebral networks for exact and approximate calculation.," *Brain*, vol. 123, no. 11, pp. 2240–2255, 2000.

[305] R. H. Grabner, D. Ansari, G. Reishofer, E. Stern, F. Ebner, and C. Neuper, "Individual differences in mathematical competence predict parietal brain activation during mental calculation," *Neuroimage*, vol. 38, no. 2, pp. 346–356, 2007.

[306] R. H. Grabner, D. Ansari, K. Koschutnig, G. Reishofer, F. Ebner, and C. Neuper, "To retrieve or to calculate? Left angular gyrus mediates the retrieval of arithmetic facts during problem solving," *Neuropsychologia*, vol. 47, no. 2, pp. 604–608, 2009.

[307] R. H. Grabner, D. Ansari, K. Koschutnig, G. Reishofer, and F. Ebner, "The function of the left angular gyrus in mental arithmetic: Evidence from the associative confusion effect," *Hum. Brain Mapp.*, vol. 34, no. 5, pp. 1013–1024, 2013.

[308] T. Dandan, Z. Haixue, L. Wenfu, Y. Wenjing, Q. Jiang, and Z. Qinglin, "Brain activity in using heuristic prototype to solve insightful problems," *Behav. Brain Res.*, vol. 253, pp. 139–144, 2013.

[309] C. A. Seger, "The basal ganglia in human learning.," *Neuroscientist*, vol. 12, no. 4, pp. 285–290, 2006.

[310] T. D. Barnes, Y. Kubota, D. Hu, D. Z. Jin, and A. M. Graybiel, "Activity of striatal neurons reflects dynamic encoding and recoding of procedural memories.," *Nature*, vol. 437, no. 7062, pp. 1158–1161, 2005.

[311] O. Monchi, M. Petrides, A. P. Strafella, K. J. Worsley, and J. Doyon, "Functional role of the basal ganglia in the planning and execution of actions," *Ann. Neurol.*, vol. 59, no. 2, pp. 257–264, 2006.

[312] F. Huang, J. Fan, and J. Luo, "The neural basis of novelty and appropriateness in processing of creative chunk decomposition," *Neuroimage*, vol. 113, pp. 122–132, 2015.

[313] C. Salvi, E. Bricolo, S. L. Franconeri, J. Kounios, and M. Beeman, "Sudden insight is associated with shutting out visual inputs," *Psychon. Bull. Rev.*, vol. 22, no. 6, pp. 1814–1819, 2015.

[314] K. C. Aberg, K. C. Doell, and S. Schwartz, "The 'creative right brain' revisited: Individual creativity and associative priming in the right hemisphere relate to hemispheric asymmetries in reward brain function.," *Cereb. Cortex*, vol. 9, pp. 1–14, 2016.

[315] A. Fink, B. Weber, K. Koschutnig, Mathias Benedek, G. Reishofer, F. Ebner, I. Papousek, and E. M. Weiss, "Creativity and schizotypy from the neuroscience perspective.," *Cogn. Affect. Behav. Neurosci.*, vol. 14, no. 2011, pp. 378–87, 2014.

[316] P. A. Howard-Jones, S. J. Blakemore, E. A. Samuel, I. R. Summers, and G. Claxton, "Semantic divergence and creative story generation: An fMRI investigation," *Cogn. Brain Res.*, vol. 25, no. 1, pp. 240–250, 2005.

[317] A. Gazzaley and M. D'Esposito, Unifying prefrontal cortex function: Executive control, neural networks, and top-down modulation. In B. Miller, B and J. Cummings, editors, *The Human Fontal Lobes*. Guildford Publications, New York, 2007.

[318] Y. Miyashita, "Cognitive Memory: Cellular and Network Machineries and Their Top-Down Control," *Science*, vol. 306, no. 5695, pp. 435–440, 2004.

[319] A. Gazzaley and A. C. Nobre, "Top-down modulation: bridging selective attention and working memory," *Trends Cogn. Sci.*, vol. 16, no. 2, pp. 129–135, 2012.